



Swansea University
Prifysgol Abertawe



Swansea University E-Theses

Nano-second laser sources for use in analytical spectroscopy.

Alshahrie, Ahmed Salem Ahmed

How to cite:

Alshahrie, Ahmed Salem Ahmed (2006) *Nano-second laser sources for use in analytical spectroscopy..* thesis, Swansea University.

<http://cronfa.swan.ac.uk/Record/cronfa42409>

Use policy:

This item is brought to you by Swansea University. Any person downloading material is agreeing to abide by the terms of the repository licence: copies of full text items may be used or reproduced in any format or medium, without prior permission for personal research or study, educational or non-commercial purposes only. The copyright for any work remains with the original author unless otherwise specified. The full-text must not be sold in any format or medium without the formal permission of the copyright holder. Permission for multiple reproductions should be obtained from the original author.

Authors are personally responsible for adhering to copyright and publisher restrictions when uploading content to the repository.

Please link to the metadata record in the Swansea University repository, Cronfa (link given in the citation reference above.)

<http://www.swansea.ac.uk/library/researchsupport/ris-support/>

Nano-Second Laser Sources for Use in Analytical Spectroscopy

By

AHMED SALEM ALSHAHRIE

B.Sc., (KING ABDUL AZIZ UNIVERSITY- SAUDI ARABIA)



Department of Physics

Swansea University

This thesis is submitted to Swansea University in candidature for the

Degree of Master of Philosophy

October 2006



ProQuest Number: 10798117

All rights reserved

INFORMATION TO ALL USERS

The quality of this reproduction is dependent upon the quality of the copy submitted.

In the unlikely event that the author did not send a complete manuscript and there are missing pages, these will be noted. Also, if material had to be removed, a note will indicate the deletion.



ProQuest 10798117

Published by ProQuest LLC (2018). Copyright of the Dissertation is held by the Author.

All rights reserved.

This work is protected against unauthorized copying under Title 17, United States Code
Microform Edition © ProQuest LLC.

ProQuest LLC.
789 East Eisenhower Parkway
P.O. Box 1346
Ann Arbor, MI 48106 – 1346

DECLARATION

This work has not previously been accepted in substance for any degree and is not being concurrently submitted in candidature for any degree.

Signed _____ (candidate)

Date 19.01.07

STATEMENT 1

This thesis is the result of my own investigations, except where otherwise stated. Where correction services have been used, the extent and nature of the correction is clearly marked in a footnote(s).

Other sources are acknowledged by footnotes giving explicit references. A bibliography is appended.

Signed _____ (candidate)

Date 19.01.07

STATEMENT 2

I hereby give consent for my thesis, if accepted, to be available for photocopying and for inter-library loan, and for the title and summary to be made available to outside organisations.

Signed _____ (candidate)

Date 19.01.07

NB: *Candidates on whose behalf a bar on access has been approved by the University (see Note 9), should use the following version of Statement 2:*

I hereby give consent for my thesis, if accepted, to be available for photocopying and for inter-library loans **after expiry of a bar on access approved by the University of Wales Swansea.**

Signed _____ (candidate)

Date 19.01.07

This thesis is dedicated to my country, my parents, my wife, my sister, and my kids (my daughter Reem, and my sons Muath and Salem)

Acknowledgment

I would like to express my sincere gratitude to my supervisor Professor Helmut H. Telle for his advice, guidance, encouragement, invaluable supervision, and help throughout this study. I would also like to thank Dr- Dave C. Beddows for his advice and help.

My thanks also go to my country " SAUDI ARABIA" for the award of the postgraduate scholarship that enabled me to achieve this work.

Similarly thanks and appreciation to the technical and support staff Julian Kivell, Dave Payne, Hugh Thomas, Mike Rogers, Ray Squire, and Linda Andrews.

I would also like to thank my colleagues for their help and advice: Mark Holton, Mohammad Abu Zeyad, Andrew Mogford, Richard Lewis, and Chris Baker.

Summary

The remit for the work described in this study was to characterize an aging Nd:YAG laser to explore what could be done to (i) extend its useful life of operation and (ii) to enhance its capabilities for spectroscopic applications.

In the first instance, the operating parameters of the Nd:YAG laser for its fundamental output at 1064nm were measured, including pulse energy (as a function of the Q-switch delay time which influences the pulse energy), pulse width and transverse intensity beam profiles (using burn paper to evaluate the uniformity). It was found that the laser still operated well, although its maximum pulse energy was down on the specifications of the laser when it was new.

In the second phase, 2nd and 3rd harmonic generation at 532nm and 355nm were implemented, using salvaged units from another laser system (non-linear crystal and harmonic separator units). Once again, the 2nd / 3rd harmonic output from the laser system was investigated. It was found that overall the laser operated to expectations, but that the beam quality for the harmonics was not very good (most likely due to surface damage of the non-linear doubling crystal).

In the third phase, the 2nd harmonic output was prepared for pumping a tuneable dye laser. For this, a telescopic beam expansion unit was built. The dye laser could be operated successfully, and as for the Nd:YAG laser itself, its output parameters were recorded, including pulse energy, pulse width and spectral tuning range.

In a final step, the Nd:YAG laser and the dye laser were successfully tested in spectroscopic applications, namely laser-induced breakdown spectroscopy (LIBS) and opto-galvanic spectroscopy (OGS).

CONTENTS

Title.

Dedication.

Acknowledgements.

Summary.

Contents.

1. Introduction	1
2. General remarks on lasers and specifics of the systems used in this study	4
2.1 Absorption, stimulated and spontaneous emission	4
2.2 Rate equations	5
2.3 Population inversion	7
2.4 Four-level laser system	8
2.5 Cavity configuration	9
2.6 Q-switching	10
2.7 Nd: YAG lasers and their characteristics	12
2.7.1 Nd: YAG crystals	12
2.7.2: Nd: YAG laser pumping	13
2.7.3 Excitation mechanisms	15
2.8 Dye lasers and their characteristics	16
2.8.1 Dye laser pumping	16
2.8.2 Excitation mechanism	17

2.8.3 Laser dyes	19
2.9 Typical applications	22
2.9.1 Nd: YAG laser applications	22
2.9.2 Dye laser applications	22
3. Laser systems used in this study	23
3.1 The Nd: YAG laser system	23
3.1.1 Optical layout	23
3.1.2 System components	24
3.2 Non-linear optics	31
3.2.1 Non-linear effects on the polarisability	31
3.2.2 Phase matching	33
3.2.3 Second harmonic generation	36
3.3 The dye laser system	36
3.3.1 Layout of the dye laser system	36
3.3.2 Dye laser components	38
4. Characterization of the Nd: YAG laser system	41
4.1 General remarks	41
4.2 Set up for the Nd: YAG laser	41
4.2.1 Adjustment of the optical axis	41
4.2.2 Adjustment of the laser beam	43
4.2.3 Optimisation of the 2 nd ad 3 rd harmonic pulse energy	43

4.2.4 Time delay between flashlamp and Q- switch operation	44
4.3 Pulse energy measurement	46
4.3.1 Pulse energy of the fundamental beam at 1064nm	47
4.3.2 Pulse energy of the 2 nd harmonic beam at 532nm	49
4.3.3 Pulse energy of the 3 rd harmonic beam at 355nm	52
4.3.4 Summary of pulse energy output data	53
4.4 Determination of beam profiles by burn patterns	55
4.5 Gaussian beam propagation	61
4.6 Pulse width	63
4.7 Fluence of the laser beam and power density	65
5. Characterisation of the dye laser system	67
5.1 Alignment of the dye laser system	67
5.2 Cleaning the dye selector and leak testing	68
5.3 Preparation of the dye solution	69
5.4 Rh B dye laser wavelengths	70
5.5 Pulse energy of the dye laser	71
6. Spectroscopic applications of the ND: YAG and the dye lasers	74
6.1 Laser-induced breakdown spectroscopy (LIBS)	74
6.1.1 Principles and theory	74
6.1.2 Apparatus for LIBS	77
6.2 Experimental results	78

6.2.1 LIBS spectra of aluminum samples	77
6.2.2 LIBS spectra of copper samples	83
6.2.3 LIBS experiment using 532nm radiation	87
6.3 Opto-galvanic spectroscopy (OGS)	89
6.3.1 Principles of opto-galvanic spectroscopy	89
6.3.2 Apparatus for opto-galvanic spectroscopy (OGS)	94
6.3.3 OGS measurements using the LP 3002 dye laser	98
6.4 Laser-induced fluorescence spectroscopy (LIFS)	103
6.4.1 Principles of laser-induced fluorescence spectroscopy	103
6.4.2 Probing the OG plasma by utilizing laser-induced fluorescence	105
7. Conclusion	107
7.1 Summary of results	107
7.2 Future work	109
REFERENCES	111

Chapter 1: Introduction

This study was carried out to set up, and understand, a laser system comprising (1) a Nd:YAG laser, (2) harmonic generation (namely 2nd and 3rd harmonic), and (3) a dye laser. All operating parameters for the Nd:YAG laser and dye laser were to be measured, and both Nd:YAG and dye lasers were to be used in selected spectroscopic applications.

This work has been divided into three parts according to the set up of the experiments and the laser used.

Part one: generation of pulses at the fundamental wavelength of the Nd:YAG laser in the infrared at 1064nm and by using KD*P crystals, generation of visible light at 532nm "green" laser pulses and UV light at 355nm. Using a harmonic separator, the three wavelengths were separated from each other. The individual components (Quantel Brilliant a Nd:YAG laser, Harmonic Generator, and Harmonic Separator) were set up to provide a uniform beam height of 75mm. In addition, an enclosure was built for the system according to the regulations of laser safety. The pulse energy of the fundamental beam at 1064 nm, 2nd harmonic wave at 532nm, and 3rd harmonic wave at 355nm were measured using an energy meter; we found as highest energies 102 mJ, 63 mJ, and 26 mJ, respectively. The pulse widths were measured for these three wavelengths by using a fast photo diode, in conjunction with an oscilloscope.

Part two: alignment of dye laser FL 3000 by using of HeNe laser, and preparing the solution that was used as active medium of the dye laser. In our study Rhodamine B (in Methanol) was used as the medium; the dye laser was pumped using the 2nd harmonic radiation of the Nd:YAG laser at 532nm. When the dye laser was pumped by pulses at 532nm, it could be tuned in the range 588-603nm.

Set ups, for spectroscopic applications was the third part of study, where the equipment for this part consisted of the appropriate laser source [The Nd:YAG laser in the study of Laser-induced Breakdown spectroscopy (LIBS), and dye laser in the study of opto-galvanic spectroscopy (OGS)], spectrometer, delay generator, detector controller, and a PC. Optical collection, focusing lens and samples (aluminium and copper) were adjusted as appropriate for the studies of LIBS or OGS. A focussed beam, either at 1064 nm or at 532nm was used for ablation, and the LIBS plasma spectra for aluminium and copper samples were investigated, for changes in resolution delay, and laser pulse energy.

In Chapter 2 a general overview for the laser systems relevant to this study is given. This includes the observation of population inversion, Q-switching, and four-level systems; a brief outline for Nd: YAG crystal, pumping of Nd:YAG lasers and excitation mechanisms is provided. This is followed by a description of the dye laser, and types of laser dyes.

The layout of the Nd: YAG and dye lasers, and ancillary components, is described in Chapter 3.

Chapter 4 includes a brief description of the adjustment and optimisation for the laser beams at 532nm and 355nm. The proportional relation between the flashlamp and Q-switch was measured (see section 4.2.4). The operating parameters (pulse energy, power and pulse width) were measured, and the beam profiles determined by using burn patterns.

The dye laser results are summarised in Chapter 5.

The results for the study of the spectroscopic applications of the Nd: YAG and dye lasers, are given in Chapter 6, including laser-induced breakdown spectroscopy (LIBS), laser-induced fluorescence spectroscopy (LIFS), and opto-galvanic spectroscopy (OGS).

Chapter 2: General remarks on lasers and specifics of the systems used in this study

In this chapter a brief summary of general laser theory is provided, including absorption, stimulated, and spontaneous emission, population inversion, four-level system, short pulse generation (Q-switching), and cavity configuration. Thereafter a brief description of Nd:YAG lasers is given, including the level structure, laser wavelength, pumping, and excitation mechanism. Finally, the applications of Nd:YAG lasers to the pumping of dye lasers conclude this chapter, addressing excitation mechanism, and laser dyes.

2.1 Absorption, stimulated and spontaneous emission

When an atom/molecule absorbs a photon of energy $h\nu = E_2 - E_1$, the process is known as (stimulated) absorption (see Figure 2.1). The transition probability per second can be written as

$$\frac{d}{dt}P_{12} = B_{12}\rho(\nu),$$

Where B_{12} is the Einstein coefficient of absorption, and $\rho_\nu(\nu)$ is the energy density (in units of J/m^3) of the incoming radiation field.

Stimulated emission occurs as the transition from an excited state E_2 to a lower state E_1 , which is added to the radiation field. The probability of stimulated emission per second is given by

$$\frac{d}{dt}P_{21} = B_{21}\rho(\nu),$$

Where B_{21} is named the Einstein coefficient for stimulated emission. If the excited state with energy E_2 is left alone, it will decay spontaneously, where A_{21} is the Einstein coefficient for spontaneous emission.

$$\frac{d}{dt}P_{21}^{spont} = A_{21}$$

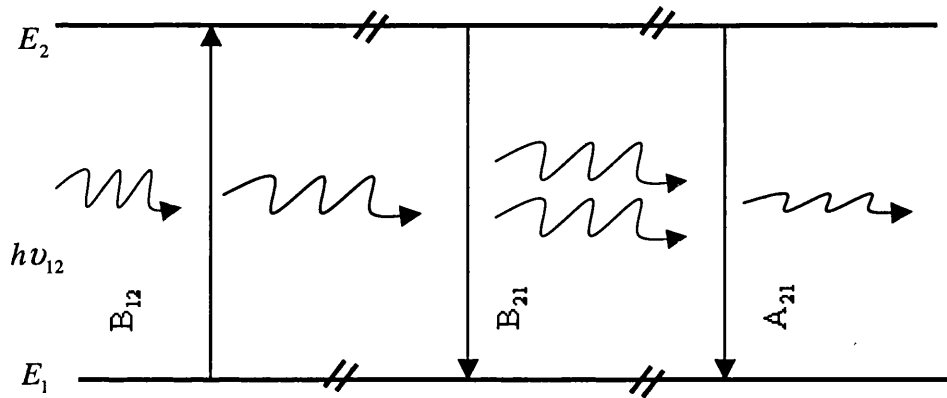


Figure 2.1: Diagram of stimulated, spontaneous absorption and emission for two levels. (Adopted from Demtröder, 2003).

In thermal equilibrium of a system with $N_0 = N_1 + N_2$ (N_1, N_2 are the population densities of the levels 1 and 2 respectively) particles, the total absorption rate $B_{12}\rho(\nu)N_1$ must be equal the total emission rate $[B_{21}\rho(\nu)N_2 + A_{21}N_2]$, i.e.

$$[B_{21}\rho(\nu) + A_{21}]N_2 = B_{12}\rho(\nu)N_1$$

2.2 Rate Equations

The rate equations including absorption, stimulated, and spontaneous emission in the four level system of a laser scheme (see Figure 2.2) are given by:

$$\frac{dN_1}{dt} = (N_2 - N_1)B_{21}nh\nu + N_2A_{21} - N_1R_1$$

$$\frac{dN_2}{dt} = P - (N_2 - N_1)B_{21}nh\nu - N_2A_{21} - N_2R_2$$

$$\frac{dn}{dt} = -\beta n + (N_2 - N_1)B_{21}nh\nu$$

N_1R_1 : Relaxation rate in the lower laser level.

N_2R_2 : Non-radiative Relaxation rate in the upper laser level.

P : Pump rate.

β : The loss coefficient, which determines the loss rate of the photon that is stored.

n : Photon density of the laser output.

This coupled differential equation system needs to be solved to determine the level populations at all times.

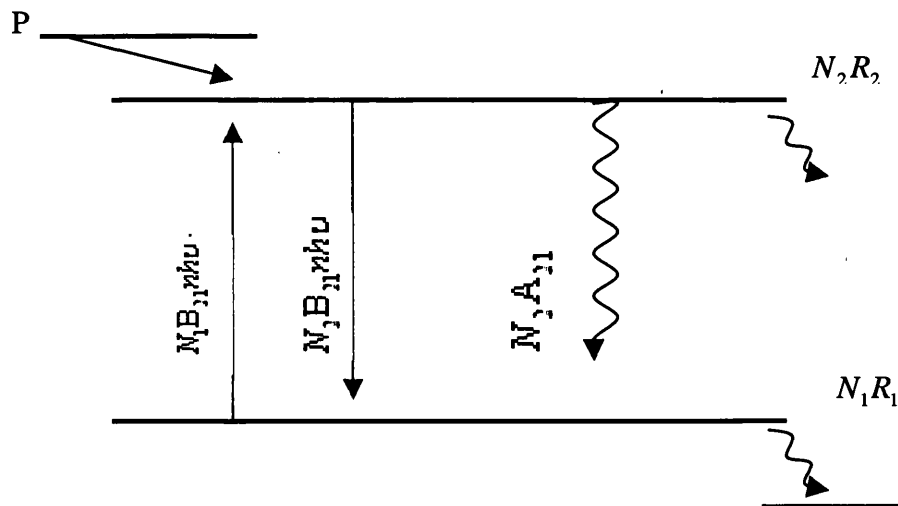


Figure 2.2: Diagram of pumping level, relaxation rate, stimulated, and spontaneous emission in a four-level system (Adopted from Demtröder, 2003).

2.3: Population inversion

Amplified radiation can only be produced when population inversion is present in the optical medium and the cavity configuration generates intensity gain. The intensity of the emerging radiation can be written as

$$I = I_0 \exp \left[\sigma_{ul} \left(N_u - \frac{g_l}{g_u} N_l \right) z \right]$$

I is the intensity of the output beam.

I_0 is the intensity of the beam that enters the medium.

σ_{ul} is the absorption cross section.

Thus, amplification only occurs, when the value of $N_u - \frac{g_l}{g_u} N_l$ is positive, otherwise,

the radiation is reduced due to absorption.

2.4 Four-level laser system

The pumping and transfer processes of the four-level system of the energy from the excited level (q) to the upper laser level (u) can be divided into three types: transfer from below as shown in Figure 2.4 (a), transfer across, Figure 2.4 (b), and transfer from above, Figure 2.4 (c).

The flux transfer rate from the excited state (q) to the upper laser level (u) is expressed as

$$F = N_u \nu \sigma_{qu} N_q$$

Where ν is represented to the average velocity between the colliding particles (atoms/molecules).

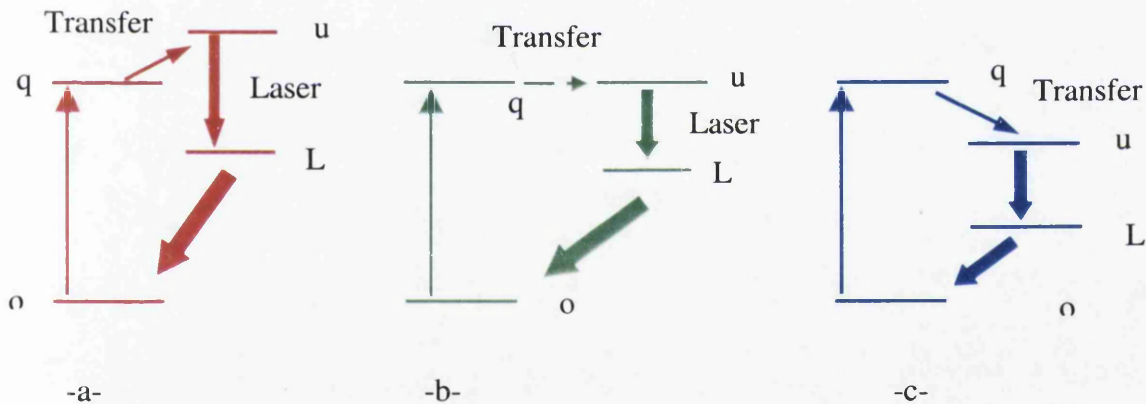


Figure 2.4: Four-level system (adopted from Silfvast, 2004).

The argon ion laser is an example of the transfer from below; transfer across occurs in the helium-neon and CO_2 lasers; and transfer from above is encountered i.e. in Nd: YAG and dye lasers [see Silfvast et al., (2004)].

A four-level system consists of ground state level (o), excited state level (q), upper laser level (u), and lower laser level (l). Level (q) receives the pumping flux, from where subsequently level (u) is populated. Level (q) is normally much close to level (u) than to level (o).

2.5: Cavity configuration

The optical cavity (resonator) of the Nd:YAG laser normally consists of two mirrors, which are placed near the end of the laser rod. There are several cavity configurations that can be used. In our Nd:YAG laser is set up with concave mirrors, within the stability regime (g_1, g_2 curvature of the mirror) $0 < g_1 g_2 < 1$ (i.e. a general spherical resonator).

The output coupling mirror has a coating, which varies over its diameter, to mimic a Gaussian beam profile in the laser output. The laser rod and the flashlamp are placed within an ellipsoid reflector to maximize optical pumping.

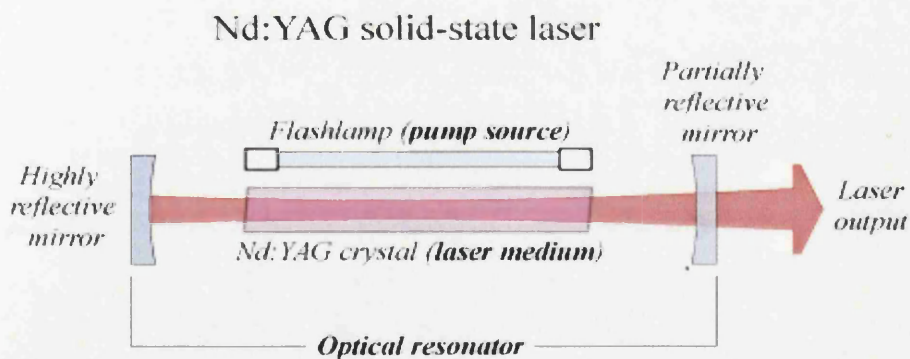


Figure 2.5: Cavity configuration of Nd: YAG laser (adopted from <http://upload.wikimedia.org/wikipedia/en/e/e8/Lasercons.png>).

2.6: Q-switching

Q-switching is a technique for producing short pulses; it depends on the timing of losses in the cavity. The population inversion can build up to a large value without laser action occurring when high losses (transmission) happen in the cavity, these losses prevent laser action. Once the population inversion is maximised, the cavity loss is suddenly reduced and laser output energy is produced, emitted in the form of a short pulse.

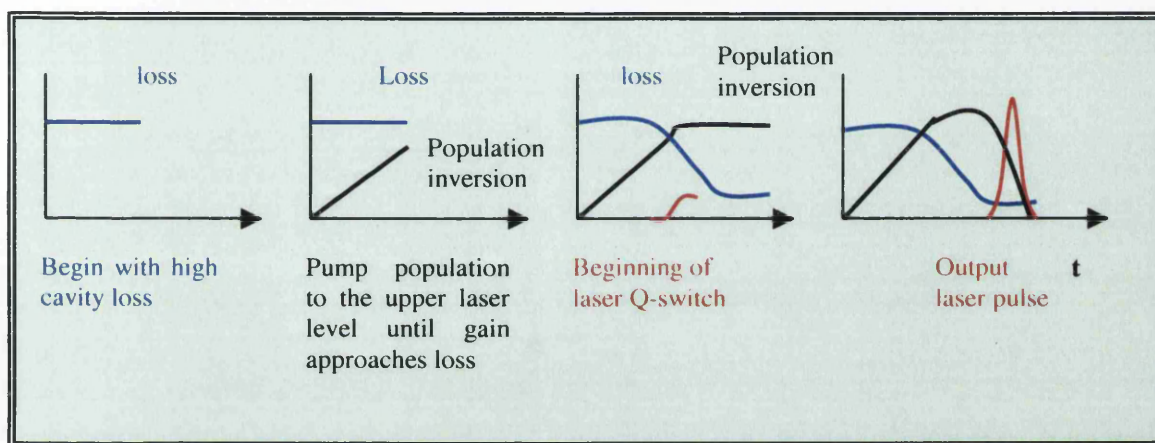


Figure 2.6: Development of Q-switched pulse. (Adopted from Silfvast, 2004).

The most common methods of Q-switching are, the rotating mirror method; electro-optic Q-switching (Pockels cell or Kerr cell), and acousto-optic Q-switching. Electro-optic Q-switching, based on a Pockels cell, is used in the Nd: YAG laser in our experiment.

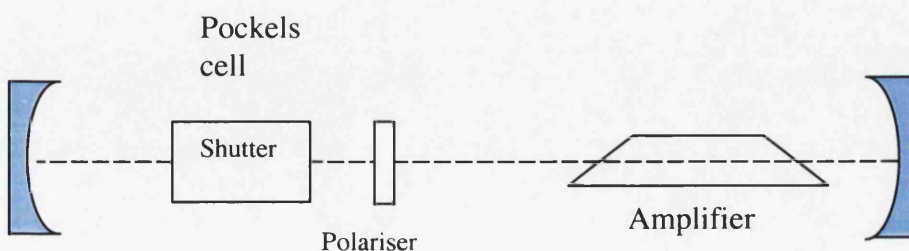


Figure 2.7: Method of Electro-optic Q-switching (Adopted from Silfvast, 2004).

Q-switching works in this type by rotating the polarisation of the beam. The electric field is applied on the crystal, which is inside of the Pockels cell; this rotates the plane of the polarisation, the angle of this rotation (θ) being proportional to the electric field (E) ($\theta \propto E$). In conjunction with a linear polariser the transmission is altered from full blocking to full transmission. The transmittance of the Q-switch is $T = T_0(1 - \cos^2 \theta)$. If $t < t_0$, the voltage (U) which is applied to the Pockels cell is zero, $U=0$, and the transmittance $T=0$ with $\theta = 0$. If at $t = t_0$, a high voltage is applied to the Pockels cell, the angle will change to $\theta = 90^\circ$, and therefore the transmittance reaches its maximum value $T = T_0$ and the beam can pass through the switch.

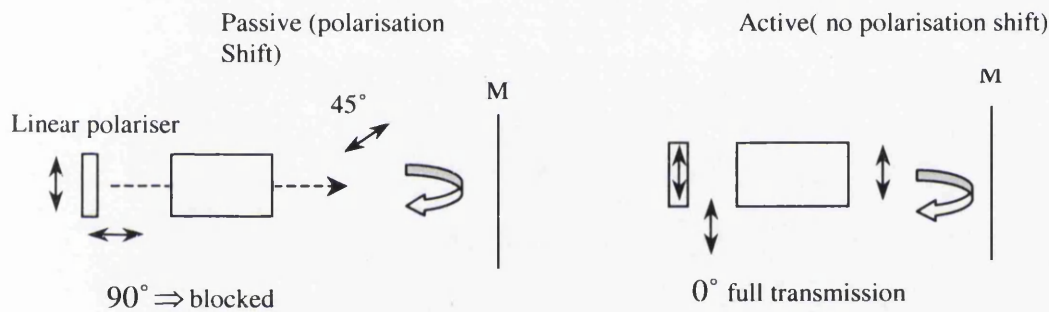


Figure 2.8: Experimental arrangement for electro-optic (EO) Q-switching.

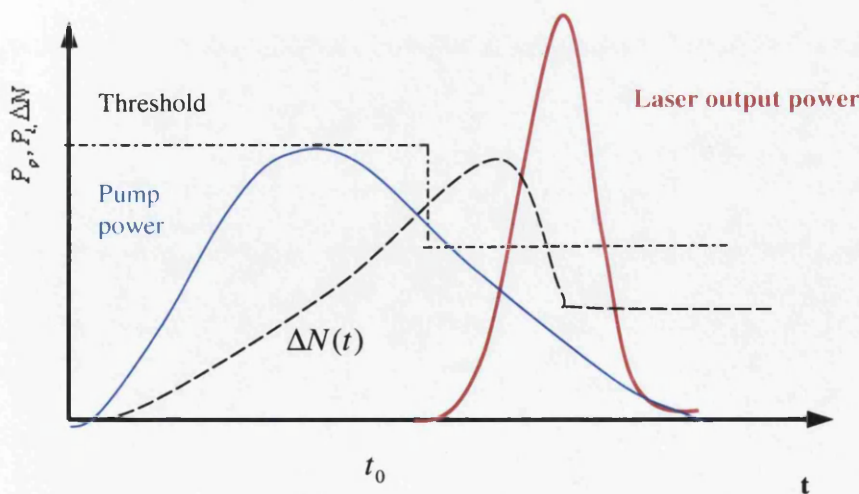


Figure 2.9: Pump power P_p , Inversion density $\Delta N(t)$, and laser output power P_l of Q-Switch. (Demtröder, 2003).

2.7: Nd:YAG lasers and their characteristics

2.7.1: Nd:YAG crystals

Yttrium Aluminum Garnet (YAG), of chemical formula ($\text{Y}_3\text{Al}_5\text{O}_{12}$), is a crystalline material, which can be manufactured with high optical quality. When the crystal is doped with 1% Nd^{3+} ions, the crystal's colour turns slightly red. The red colour occurs because the main absorption of Nd^{3+} occurs for 430nm to 590nm (see Figure 2.10). Further absorption bands are observed between 700 and 900. The typical size of laser crystals is approximately 1-160mm in length with diameters of 3-14mm, the damage threshold of the material is $>15 \text{ J/cm}^2$.

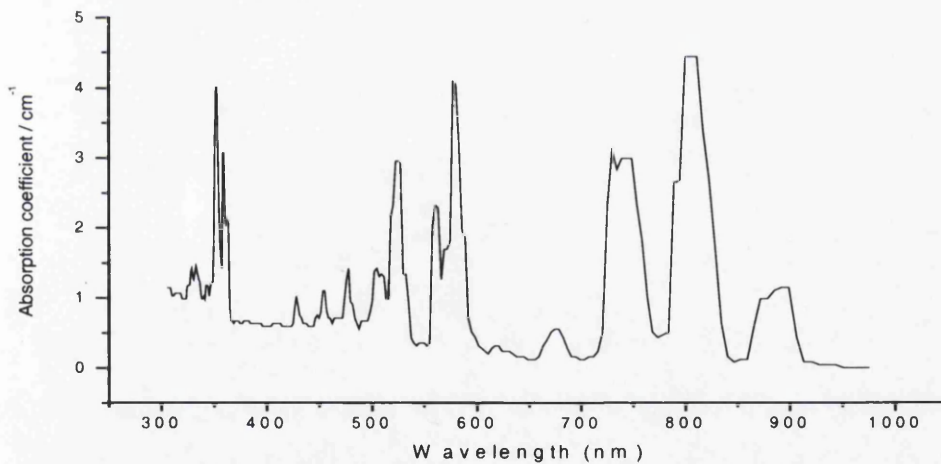


Figure (2.10): Optical absorption of Nd: YAG crystal (adopted from Goodwin,1970).

2.7.2: Nd:YAG laser pumping

1. Flashlamp-pumped Nd:YAG lasers

Mostly, krypton and xenon lamps are used for broadband pumping of Nd:YAG. Either type of lamp has strong emission lines in the infra red part of the spectrum. For pulsed lasers mostly xenon lamps are used. The emission spectrum of such a flashlamp is shown in Figure 2.11. It is notable that its highest energy output is in the IR, matching the 700-900nm absorption band of Nd: YAG (see Figure 2.10).

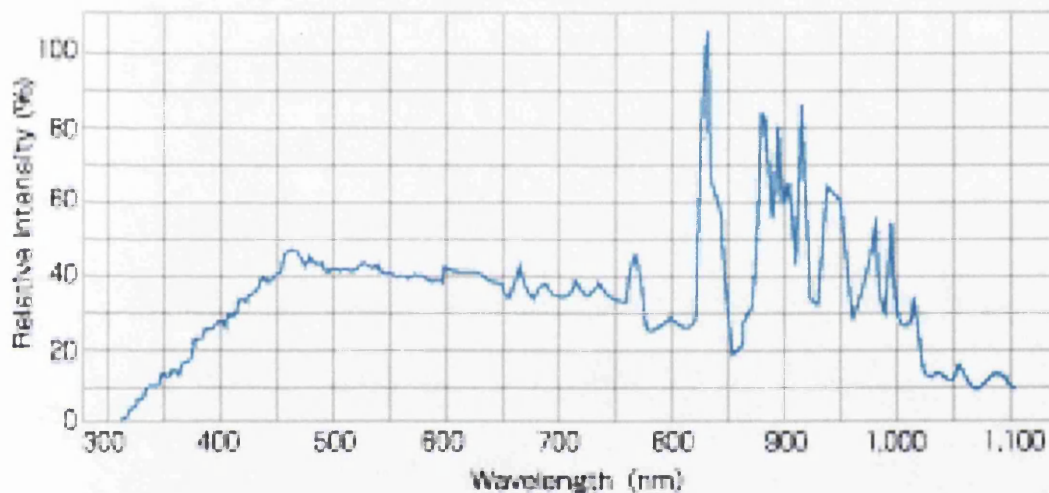


Figure: 2.11: Spectrum of Xenon flashlamp. (Adopted from http://www.ushio.co.jp/products/catalog/imp_e/image/166.gif).

2. Diode laser pumped Nd: YAG lasers:

Instead of flashlamps, diode lasers can be used to pump Nd:YAG lasers. The efficiency of the Nd:YAG lasers can be raised to 20-30 % if diode lasers are used for pumping. This

is because the emission of the diode laser can be matched exactly to the Nd:YAG absorption bands, and hence no pump light is lost, as is the case for Xe-flashlamps.

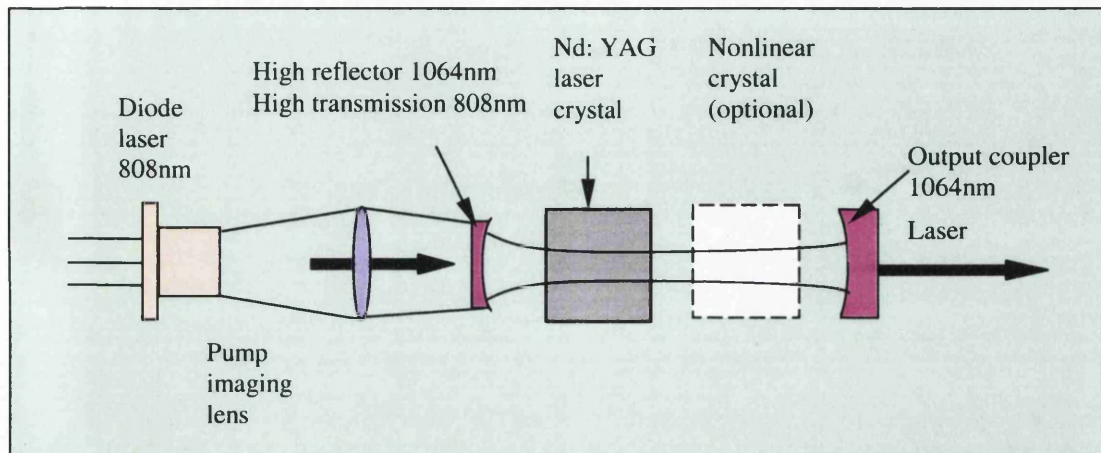


Figure 2.12: Standard diode laser pumping of Nd: YAG laser (Adopted from Silfvast, 2004)

GaAs diode lasers are the most effective way to pump a Nd:YAG laser; the best absorption in Nd:YAG is for diode lasers operating at 808nm.

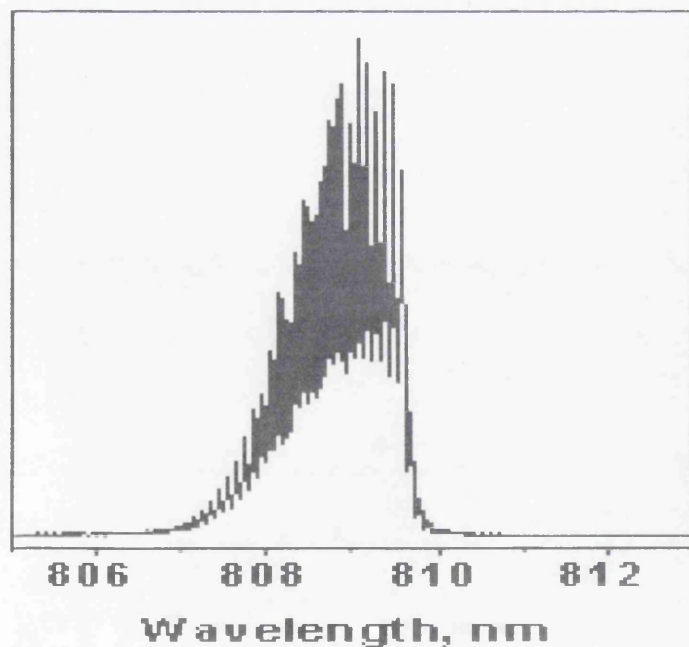


Figure 2.13: Laser diode emission with wavelength 808nm (adopted from <http://www.atcsd.ru/grapfic/LDspectr.gif>).

2.7.3: Excitation mechanism

Nd:YAG lasers constitute four-level systems. Flashlamps are used with light in the range 720-900nm to pump the population from the ground state E_1 to the upper states E_4 or at 808nm with diode laser to population individual sublevel in E_4 . Rapid decay occurs from upper energy levels to the lower laser level. Lasing is created predominantly at 1064nm, on the transition from the ${}^4F_{3/2}$ to the ${}^4I_{11/2}$ energy levels.

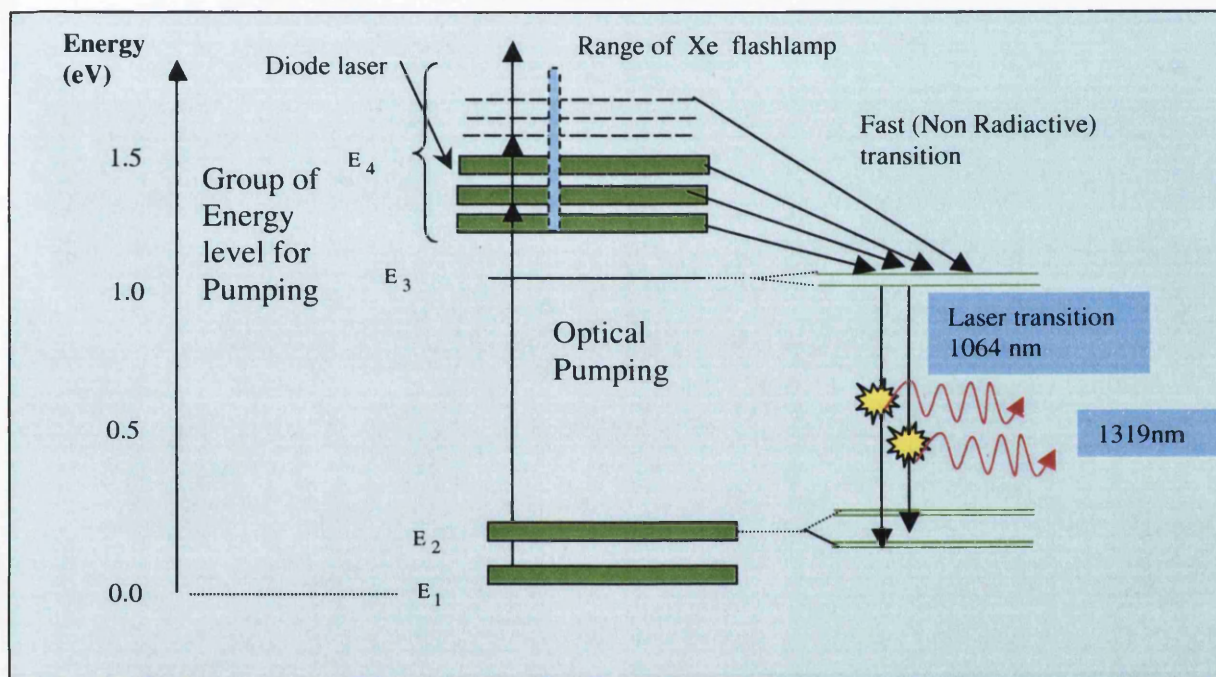


Figure214: Excitation of Nd: YAG lasers (adopted from www.lasalle.edu/academ/chem/laser_web/ndyag_laser.html).

2.8: Dye lasers and their characteristics

The dye laser is a tunable light source for e.g. high-resolution spectroscopic detection of atoms and molecules in several applications. P. Sorokin and F. P. Schafer invented the dye laser in 1966. Dye laser radiation is created in a liquid medium, which contains organic dyes. Dye lasers are divided into three main types: pulsed, CW (continuous wave), and mode-locked dye lasers.

2.8.1: Dye laser pumping

Optical pumping is normally used for dye lasers; specifically pumping by a Nd: YAG laser at 532nm (2nd harmonic) or 355nm (3rd harmonic) is rather popular for pulsed dye lasers. In general, the pump beam at 532nm, 355nm (or excimer laser) is separated into several beams; one of them is used to pump the oscillator, which contains a beam expander, a grating, and a wavelength selective elements. The remaining pump power is used to excite dye amplifiers.

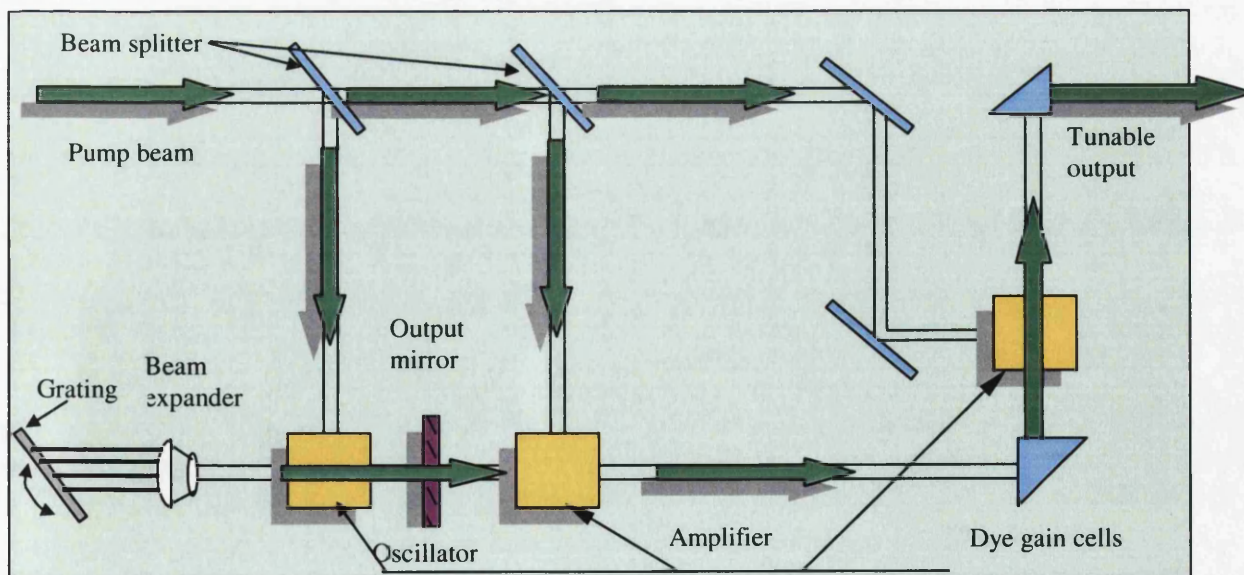


Figure 2.15: Laser -pumped tunable dye laser (Silfvast, 2004).

2.8.2: Excitation mechanism

When dye molecules are diluted in a liquid solvent, the discrete ro-vibrational energy levels merge into broadened bands. Notably, S_0 and S_1 indicate singlet states and T_1 and T_2 refer to triplet states (see Figure 2.16). Since S_1 is a broad energy state, an absorption wavelength that pumps the population can also be broad into S_1 (excited singlet state). Within S_1 the population decays quickly in times of $\sim 10^{-12}$ sec, from higher sublevels to the lowest level of this state, called (u) (see Figure 2.17). The time of decay between upper level (u) and level (l) is of the order of ns, substantially slower than the relaxation time within S_1 . Thus, the population accumulates at level u and an inversion provides between (u) and (l) allows laser action. From (l) the population relaxes quickly back to the lowest energy state (o). Overall, the dye laser constitutes a four-level laser scheme.

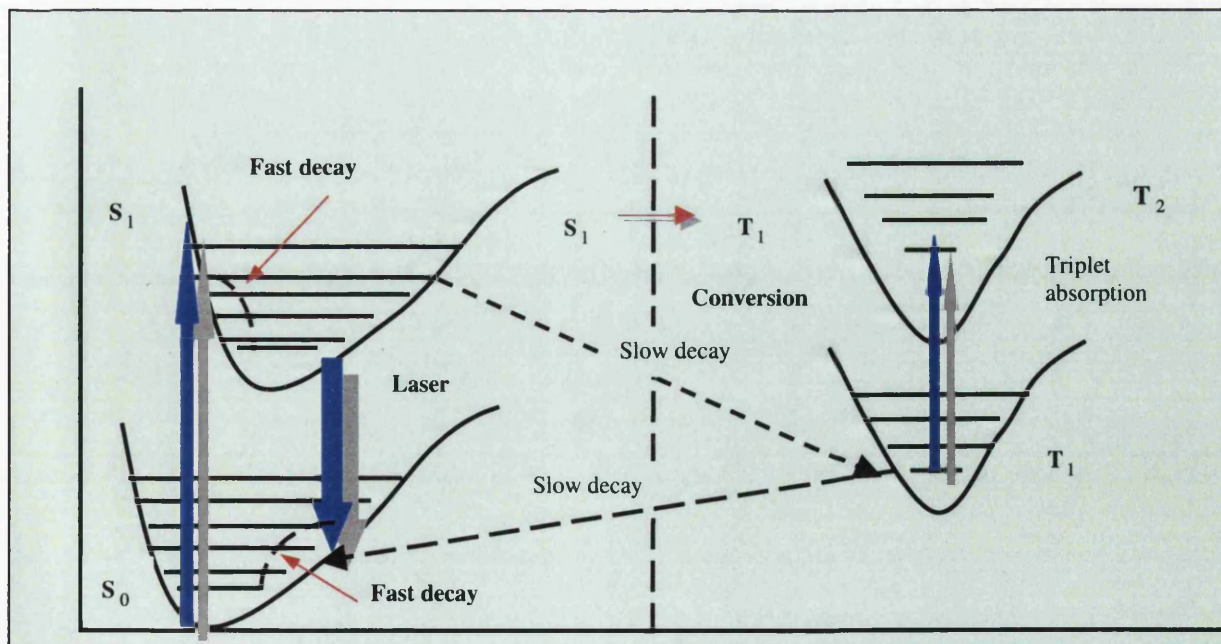


Figure 2.16: Scheme of energy level of the dye laser (Joseph T. Verdeyen, 1995).

A small portion of the population in S_1 transfers to the triplet T_1 state; this is known as intersystem crossing (see Figure 2.16 above). $T \leftrightarrow S$ are spin-forbidden transitions, which cause two problems. The first of them, the absorption from T_1 to T_2 , leads to loss in the laser gain because often its absorption wavelengths coincide with the laser wavelength. The second reason is that the molecules in triplet states tend to react and change to other molecules. This causes severe degradation of the dye solution.

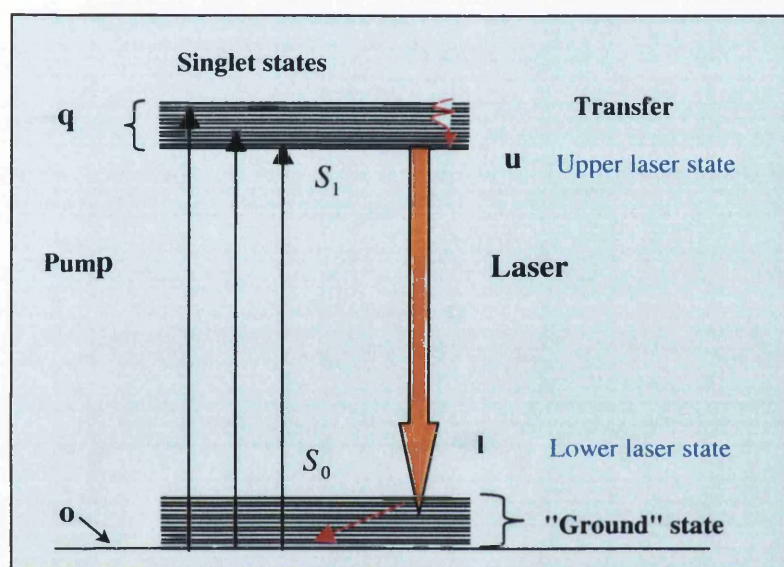
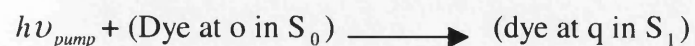


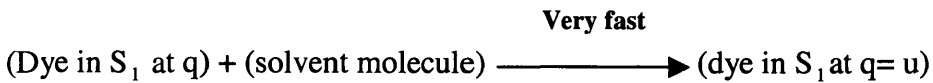
Figure 2.17: Schematic energy level scheme and pumping cycle in dye molecules (Demtröder, 2003).

The excitation -emission cycle can be summarized as following:

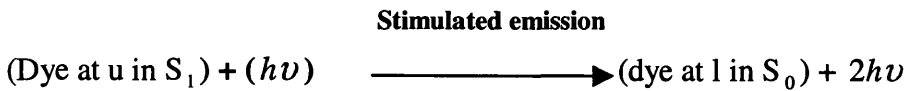
(1) Absorption of a photon from the pump source:



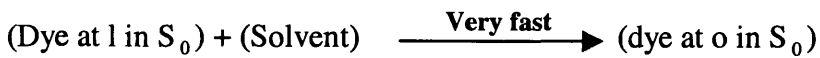
(2) The relaxation in the upper S_1 band



(3) Spontaneous or stimulated emission back to S_0 band



(4) Relaxation in the lower S_0 band

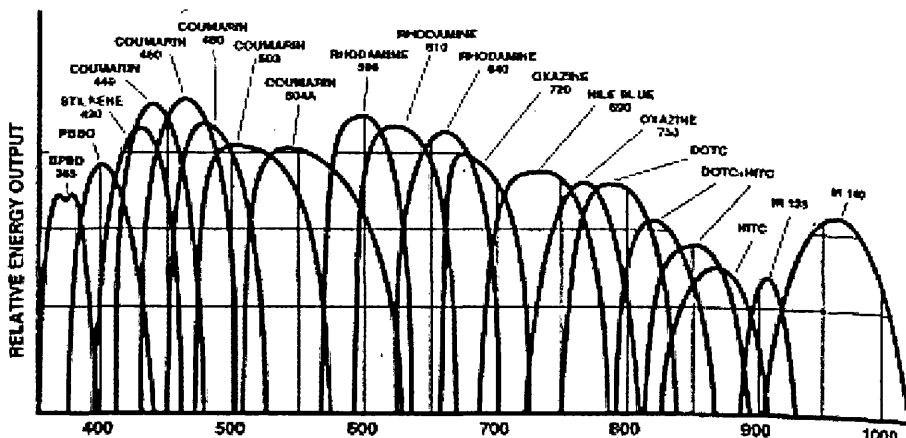


(see Verdeyen, 1995).

2.8.3: Laser dyes

1. Type of laser dyes

A large number of laser dyes exist, which can be pumped by visible (green) or UV radiation originating from a Nd: YAG laser, as recorded in Table 2.1. Their laser output spectra are shown in Figure 2.18. In our study the dye Rhodamine B (LC 6100) was used.



2.18: Spectral profiles of different laser dyes (see Demetröder, 2003).

Table 2.1: Selected dyes for Nd: YAG laser-pumped dye lasers. (Adopted from Lambda Physik).

Laser dye	Peak(nm)	Tuning range (nm)	Pumped λ (nm)	Solvent
LC 3990 Furan 2	402	392-422	355	Methanol
LC 4260 Furan 1	421	410-435	355	Methanol
LC 4200 Stelbene 3	428	415-439	355	Methanol
LC 4400 Coumarin 120	440	420-470	355	Methanol
LC 4700 Coumarin 47	460	444-476	355	Methanol
LC 4800 Coumarin 102	480	462-497	355	Methanol
LC 5000 Coumarin 307	508	485-546	355	Methanol
LC 5100 Coumarin 500	518	498-546	355	Methanol
LC 5400 Coumarin 153	540	516-575	355	Methanol
LC 5530 Fluorescein 27	550	540-575	532	Methanol
LC 5750 Rhodamine 19	567	556-586	532	Methanol
LC 5900 Rhodamine 6G	566	555-585	532	Methanol
* LC 6100 Rhodamine B	594	584-619	532	Methanol
LC 6200 Sulforhodamine B	588	579-600	532	Methanol
LC 6400 Rhodamine 101	621	611-662	532	Methanol
LC 6600 Sulforhodamine 101	628	619-673	532	PC**
LC 6500 DCM	639	615-666	532	PC**

* This is the one used in our experiments.

** PC = Propylene carbonate

2. Rhodamine B (Lambda Physik catalogue number LC 6100)

Rhodamine B is the laser dye, which is used in our experiment. The chemical structure of Rhodamine B is displayed in Figure 2.19. It can be dissolved in methanol and ethanol.

The nominal emission range of RhB is between 580-620nm (see Figure 2.20).

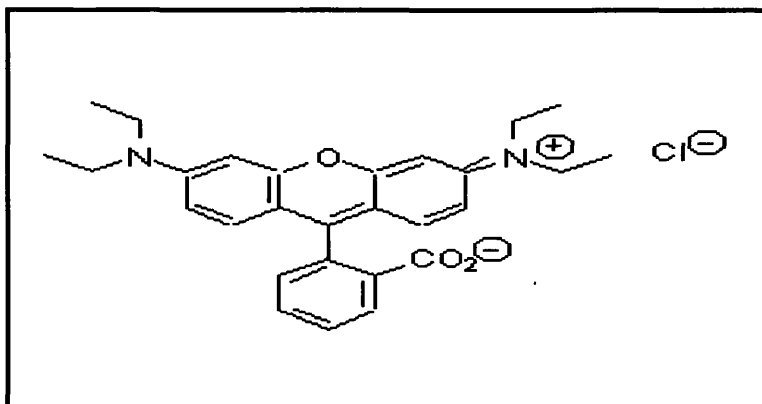


Figure: 219: Chemical structure of Rhodamine B. ([http://omlc.ogi.edu/spectra/PhotochemCAD/html/rhodamine B.html](http://omlc.ogi.edu/spectra/PhotochemCAD/html/rhodamine%20B.html)).

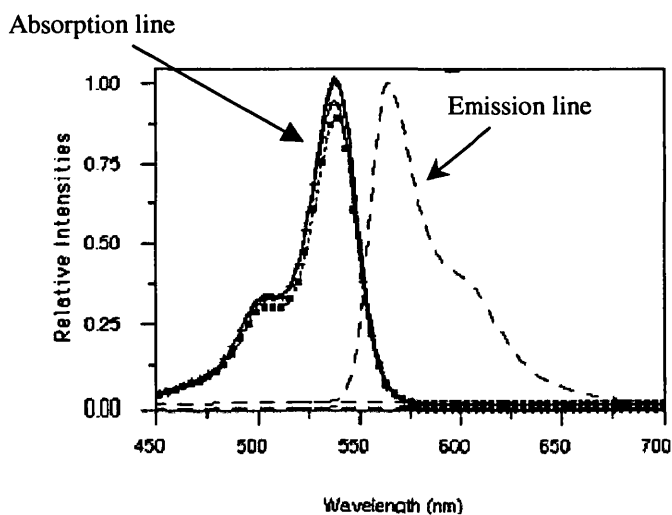


Figure 2.20: Absorption and emission spectrum of RhB. (<http://www.tufts.edu/CMPWebsite2/Public/Bibliography/PaperImages/Image44.gif>).

2.9: Typical applications

2.9.1 Nd:YAG laser applications

Nd:YAG lasers are used in several industrial applications, such as drilling, spot welling, or marking. Nd:YAG lasers can also be used to pump tunable (dye) lasers, which are used in research applications such as Raman spectroscopy, or remote sensing. Finally, they may be used in military applications, such as range finders and target designators.

2.9.2: Dye laser applications

Dye lasers are used in several applications, e.g. in medical applications to remove birthmarks and to shatter kidney stones by directing the beam through optical fibers to the kidney. Also, dye lasers are important in laboratory research, such as analytical spectroscopy where it is used e.g. in the laser-induced fluorescence spectroscopy (LIFS) and opto-galvanic spectroscopy (OGS).

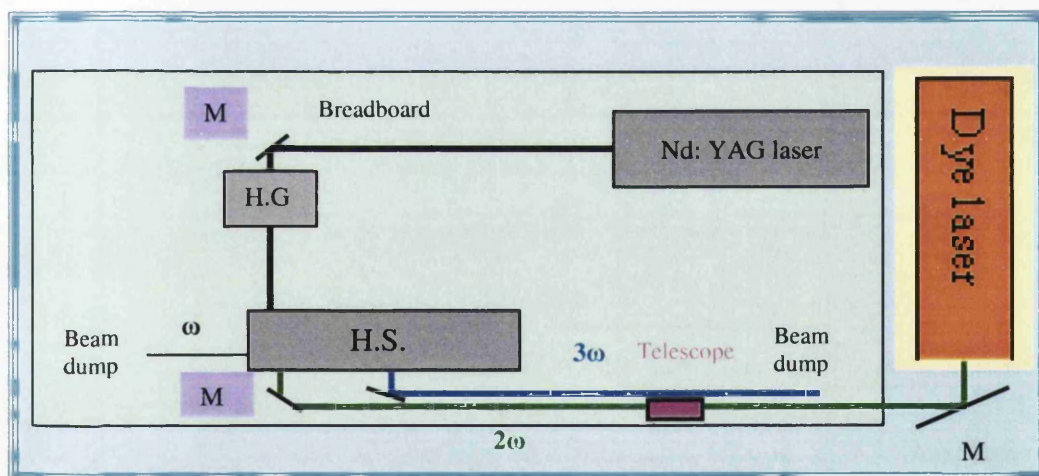
Chapter 3: Laser systems used in this study

In this chapter the Nd:YAG laser system, which was used in this work, and its components are described, together with non-linear harmonic generation. Finally, the dye laser system with its components is discussed.

3.1: The Nd:YAG laser system

3.1.1: Optical layout

The overall layout (all components mounted on a breadboard) is shown schematically in Figure 3.1. The individual components are described in the following section.






	355nm (3ω)	H.G. Harmonic Generator
	532nm (2ω)	H.S. Harmonic Separator
	1064nm (1ω)	M Steering Mirrors

Figure 3-1: Optical layout of the Nd: YAG and dye laser systems.

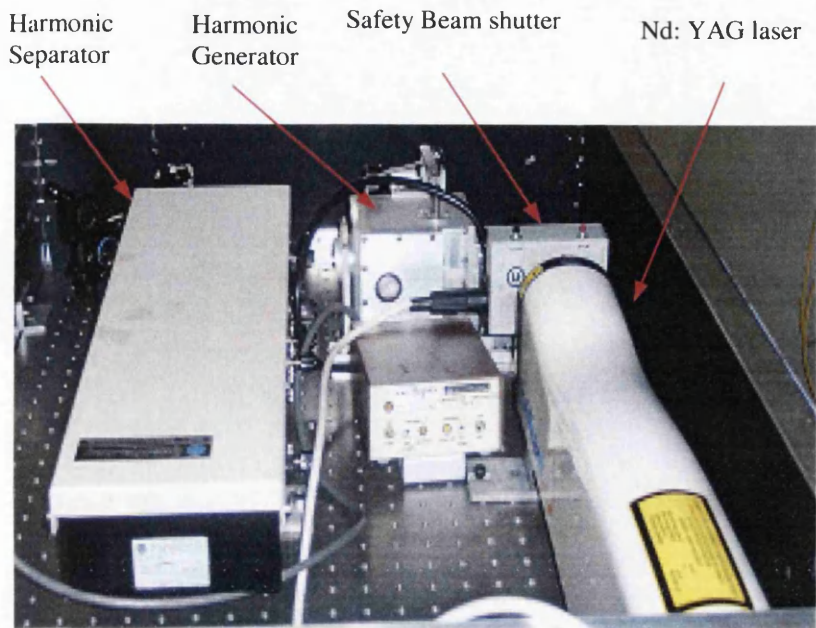


Figure3.2: The Nd: YAG laser system.

3.1.2: System components

The system comprises the following building blocks: Quantel "Brilliant" Nd: YAG laser, Harmonic Generator, Harmonic Separator, beam steering mirrors, pulse energy probe including divergent lens to lower the pulse energy density, and the dye laser (Lambda Physik FL3002). A telescope is also used in the experiment (to adapt the beam shape to the dye laser). Ancillary components are an IR visualiser, a PIN diode, an oscilloscope and an alignment HeNe laser.

1. **Quantel "Brilliant" Q-switched Nd: YAG laser.** This laser consists of two parts: the first is the optical head that includes the flashlamp, Q-switch and Nd: YAG laser rod Figure 3.3. The second part is the power supply unit (PSU) shown in Figure 3.4, which contains the power supply and the cooling group cabinet. An

umbilical connects the optical laser head and the power supply unit; it is 3.3m long and 45mm in diameter.



Figure3.3: Quantel Brilliant (Q-Switch Nd: YAG laser).



Figure3.4: Power supply unit

2. **Harmonic Generator (Quanta Ray).** This unit is used to generate the 2nd harmonic radiation at 532nm and the 3rd harmonic radiation at 355nm. It has two KD*P (Potassium Dideuterium Phosphate) crystals, one of them generates the 2nd harmonic wave (2ω) at 532nm and the other generates the 3rd harmonic output (3ω) at 355nm (by mixing 2ω and ω), as shown below in Figure 3.7.

The harmonic generator is connected to a temperature controller, which stabilizes the temperature of the crystals.

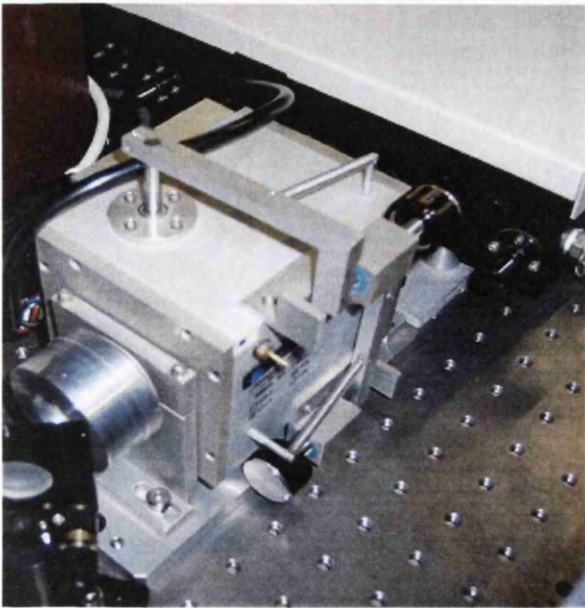


Figure 3.5: Harmonic generator

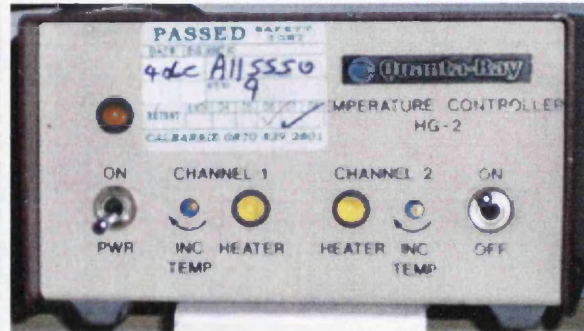
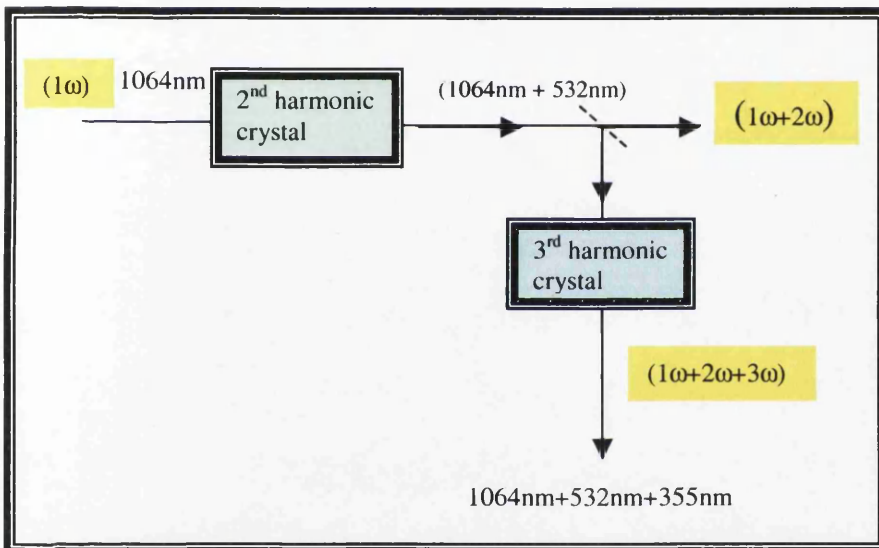
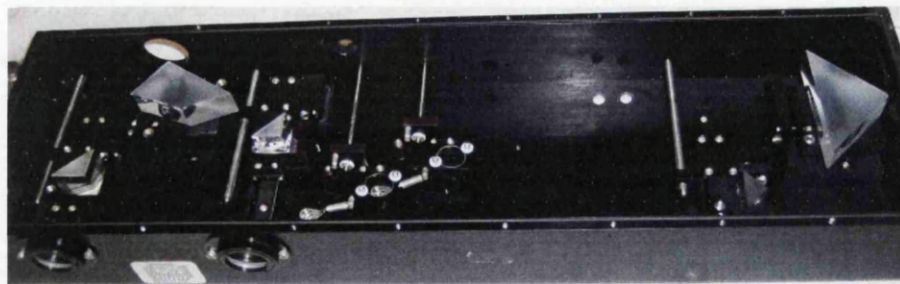


Figure 3.6: Temperature controller HG.

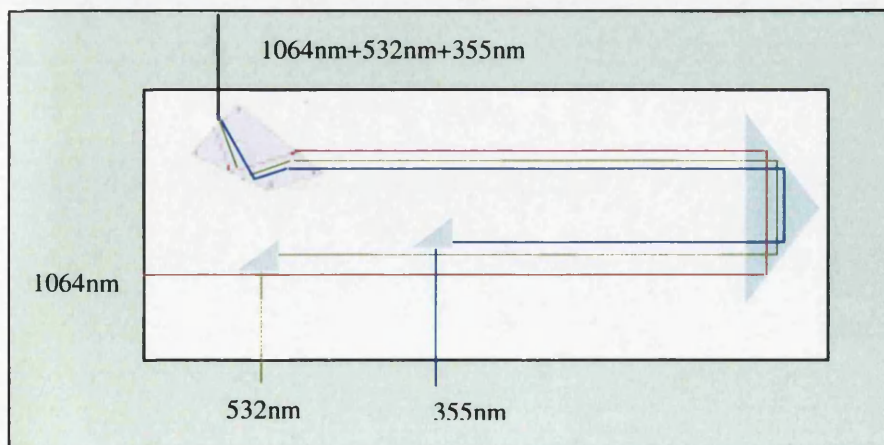
Figure 3.7: 2nd and 3rd harmonic generation layout

KDP / KD*P crystals, [KH_2PO_4 / KD_2PO_4] are transparent from 210nm to 1400nm for the non-deuterated, and 210nm to 1700nm for the deuterated material. The damage threshold of these crystals is over $3\text{GW}/\text{cm}^2$. For further details see e.g. Harper and Wherrett (1977).

3. **Mirrors for the fundamental beam (NB1-J14).** These are BK7 mirrors with a dielectric coating. They exhibit very low losses of only 0.3%, i.e. they have reflectivities of 99.7%, and have a damage threshold of $5\text{J}/\text{cm}^2$ for 10ns pulses, incident at an angle of 45° . Their diameter is 25.4mm.
4. **Mirrors for the 2nd harmonic beam at 532nm (NB1-J12).** These are BK7 mirrors with a dielectric coating. They exhibit very low losses of only 0.3%, i.e. they have reflectivities of 99.7%, and have a damage threshold of $5\text{J}/\text{cm}^2$ for 10ns pulses, incident at an angle of 45° . Their diameter is 25.4mm.
5. **Mirror for the 3rd harmonic beam at 355nm (NB1-J08).** These are BK7 mirrors with a dielectric coating. They exhibit very low losses of only 0.5%, i.e. they have reflectivity of 99.5%, and have a damage threshold of $5\text{J}/\text{cm}^2$ for 10ns pulses, incident at an angle of 45° . Their diameter is 25.4mm.
6. **Harmonic separator** It is used to separate the various harmonics emerging from the harmonic generator.



a



b

Figure 3.8: (a)- Inside view of the harmonic separator. (b)- Schematic layout of the beams in the harmonic separator

It consists of a Pellin-Broca prism, right angle prisms with 90° and 180° deflection, and windows, as shown in Figure 3.8. The Pellin-Broca prism is placed in the harmonic separator to separate the three wavelengths. The Pellin-Broca prism is named after its inventors Ph. Pellin, a French instrument maker, and Andre Broca, a Professor of Physiological Optics.

In Figure 3.9 a Pellin-Broca prism is shown schematically. The light enters from side AB; all refractions and dispersions occur inside the prism, and the wavelengths exit from the face AD as separated beams.

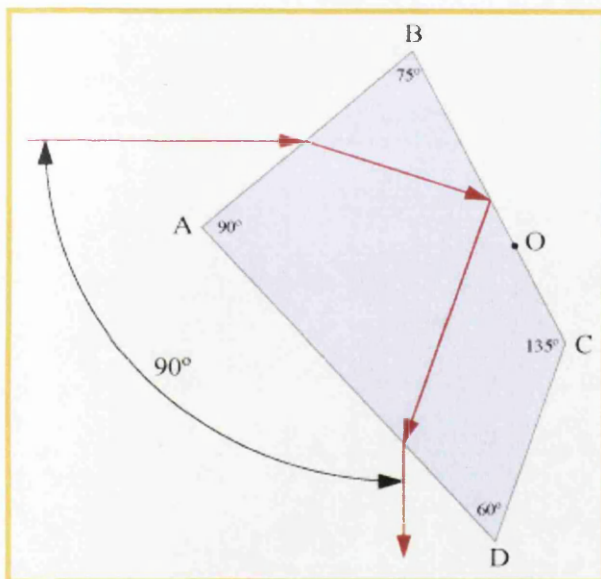


Figure3.9: Pellin –Broca prism (adopted from www.en.wikipedia.org/wiki/Pellin-Broca_prism).

For a Pellin-Broca prism the output beam angle is always at 90° to the input beam path. It can be made of many different materials, but is the mainly manufactured from fused silica (FS) or BK7. Our harmonic separator consists of a fused -silica Pellin-Broca prism, because it has high transmittance in the wavelengths at range of UV to IR, see Figure

3.10 (a and b), and low thermal expansion coefficient. The damage threshold of the (FS)

Pellin-Broca prism is $15\text{J}/\text{cm}^2$ for 20ns, 20Hz at Nd: YAG laser at 1064nm.

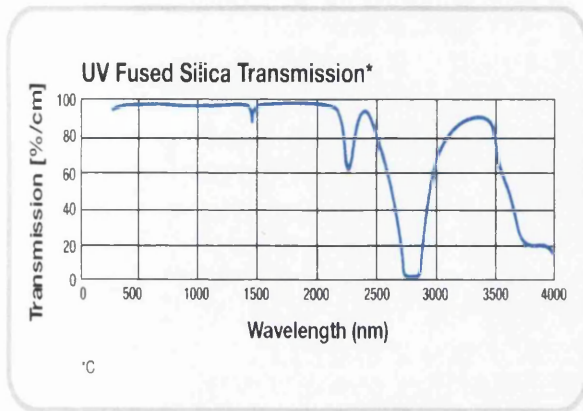


Figure 3.10 a: UV Fused Silica transmission (adopted from Thorlabs catalogue).

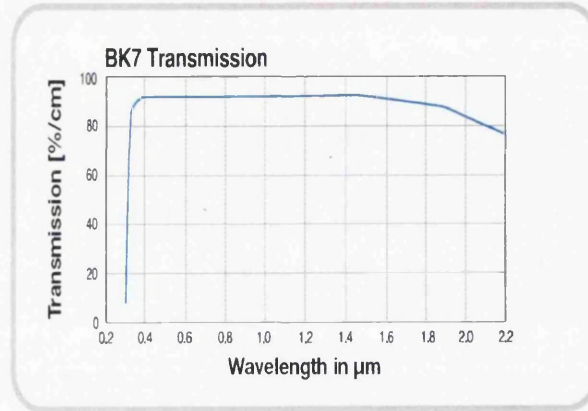


Figure 3.10 b: BK7 transmission (adopted from Thorlabs catalogue).

A right angle prism (in 180° deflection configuration) is used to reflect the three wavelengths back into the separator box, as shown in Figure 3.8 b. It is made of fused silica, without coating. This is done to reduce the size of the box, by folding the beam path. Right angle prisms (in 90° deflection configuration) are used to reflect the wavelengths 532nm and 355nm out of the harmonic separator.

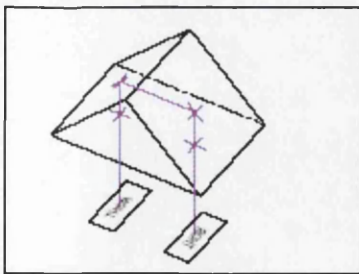


Figure 3.11 a: Right angle prism, 180° deflection (adopted from Thorlabs catalogue).

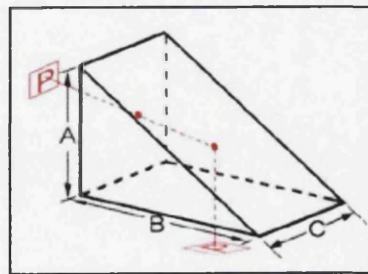


Figure 3.11 b Right angle prism, 90° deflection (adopted from www.sp3plus.co.uk/optics/right-angle-prisms.htm).

The prism, which reflects the 532nm radiation, is made of BK7 glass; the one that reflects the 355nm radiation is made from fused silica. This is because the transmission of fused silica is better than BK7, particularly at 355nm (3ω), as shown in Figure 3.10 (a and b) above.

Finally, the harmonic separator contains two anti-reflection coated windows that permit the wavelengths to exit from the sealed unit. Again, the window that is used for the 3rd harmonic wave at 355nm is made from fused silica, while the window, which is used for the 2nd harmonic wave is made from BK7.

7. **Lens** (divergent lens). This is used to expand the beam to avoid damage to the energy probe. This divergent lens has AR coating for the fundamental at 1064nm and 2nd harmonic at 532nm exhibiting reflective losses of $R= 0.25\%$. The AR coating of the lens for the 3rd harmonic at 355nm has losses of $R= 0.5\%$.
8. **Energy probe**. This joule meter is used to measure the pulse energy; it has a minimum sensitive of $\sim 4\text{mJ}$.
9. **Infrared visualiser**. This is used to show the IR laser beam (for its shape see Figure 3.12).



Figure 3.12: Infra red visualiser

10. **PIN diode and oscilloscope.** These are used to measure the length of the pulses at the fundamental 1064nm (1ω), 2nd harmonic 532nm (2ω) and 3rd harmonic 355nm (3ω) wavelengths. Measurement data are reported in Chapter 4.

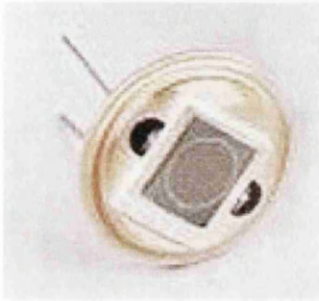


Figure 3.13 a: PIN diode.



Figure 3.13 b: The oscilloscope (Texstar DCS 2150).

11. **HeNe laser.** It is used to align the beam paths in the system.

3.2. Non-linear Optics

In this section, a brief summary of the basic concepts for harmonic generation and phase matching is given.

3.2.1 Non-linear effects on the polarisability

The polarization, \mathbf{P} , of a medium with non-linear susceptibility, χ , dependent to an electric field, \mathbf{E} , can be expressed as

$$\mathbf{P} = \epsilon_0 (\chi^1 \mathbf{E} + \chi^2 \mathbf{E}^2 + \chi^3 \mathbf{E}^3 + \dots) \quad (3.1)$$

Where $\chi^{(k)}$ is the kth-order susceptibility tensor of rank k+1. For the second term (which is associated with frequency doubling and sum-frequency generation, for us 2ω and $3\omega = 2\omega + \omega$, respectively), the susceptibility χ^2 tensor is of rank 3, with components

χ_{ijk} ,

$$P_i^{(2)} = \epsilon_0 \sum_{j,k=1}^3 \chi_{ijk}^{(2)} E_j E_k \quad (3.2)$$

Assume that the total electromagnetic wave, for two incident waves is

$$E = E_1 \cos(\omega_1 t - k_1 z) + E_2 \cos(\omega_2 t - k_2 z)$$

Then the second term in equation (3.1) can be written as, (for the case that $z = 0$):

$$\begin{aligned} P^{(2)} &= \epsilon_0 \chi^2 E^2 \\ &= \epsilon_0 \chi^2 (E_1^2 \cos^2 \omega_1 t + E_2^2 \cos^2 \omega_2 t + 2E_1 E_2 \cos \omega_1 t \cdot \cos \omega_2 t) \\ &= \epsilon_0 \chi^2 \left[\frac{1}{2} (E_1^2 + E_2^2) + \frac{1}{2} E_1^2 \cos 2\omega_1 t + \frac{1}{2} E_2^2 \cos 2\omega_2 t + E_1 \cdot E_2 [\cos(\omega_1 + \omega_2)t + \cos(\omega_1 - \omega_2)t] \right] \end{aligned}$$

It is the term $E_1 \cdot E_2 \cos(\omega_1 + \omega_2)t$, which is the relevant one for ($2\omega = \omega + \omega$) and ($3\omega = 2\omega + \omega$) harmonic generation.

3.2.2: Phase matching

The nonlinear polarization acts as a source of new waves at frequencies $\omega = \omega_1 + \omega_2$ that propagate through the crystal with phase velocity $v_{ph} = \frac{\omega}{k} = \frac{c}{n}$. The phase matching

condition that conserves momentum is given by the vector equation

$$k(\omega_1 \pm \omega_2) = k(\omega_1) \pm k(\omega_2) \quad (3.3)$$

Two examples for this are shown in Figure 3.15.

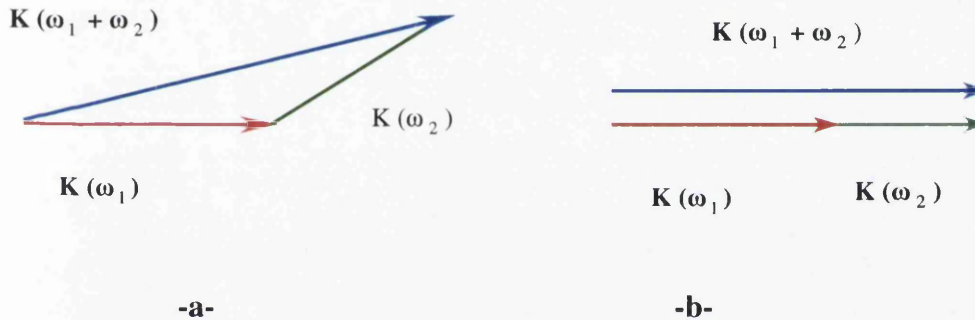


Figure 3.15: Phase matching condition associated with momentum conservation. a) Non-collinear propagation of the three beams. b) Collinear propagation of the three beams (Demtröder, 2003).

The collinear case is achieved for $\theta = 90^\circ$ (for the meaning of θ see Figure 3.16), and both fundamental wave and second harmonic wave travel in collinear direction through the crystal, the non-collinear case is encountered for $\theta \neq 90^\circ$.

Two methods, angle tuning or temperature tuning, can be used to achieve phase matching. In our study, angle tuning is used to optimize the non-linear harmonic generation. Note that if the angles between the three beams are large, the efficiency of the sum or difference frequency will decrease, because the overlap region between the waves

becomes too small. The maximum efficiency is found when the angles between the three waves are nearly zero, as shown in Figure 3.16,b collinear case (see e.g. Demtröder, 2003).

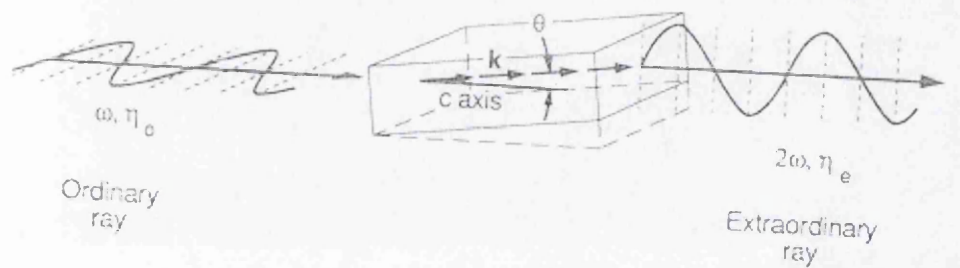


Figure 3.16: Phase matching using angle tuning (see e.g. Silfvast, 2004).

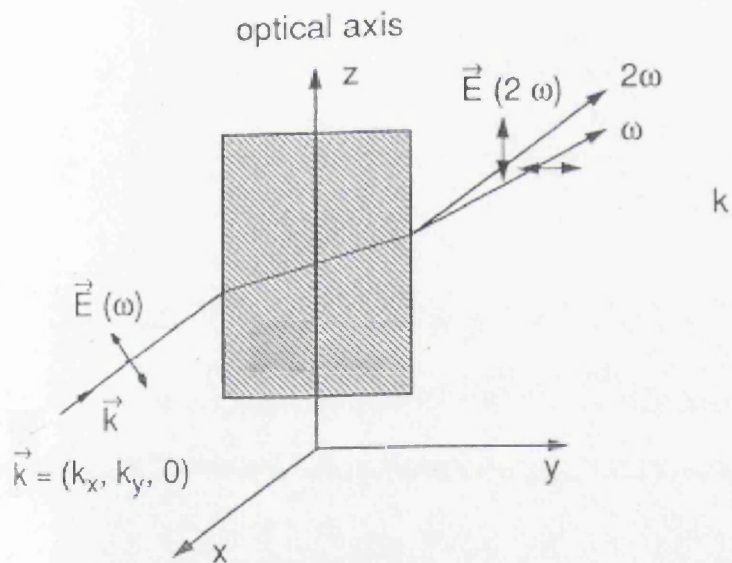


Figure 3.17: Description of nonlinear optics coordinate system in a KDP crystal (see Demetroder, 2003).

The ordinary ray is polarised perpendicular to the plane of the optical axis of the crystal and the propagation vector, while the extraordinary ray is polarised in the plane of the optical axis and propagation vector (see Figure 3.16 and 3.17). One denotes η_o as the refraction index of the ordinary ray, and η_e as the refraction index of the extraordinary ray.

Note that η_e is dependant on the angle between the optical-axis and the propagation vector; the change can be expressed as:

$$\frac{1}{\eta_e^2(\theta)} = \frac{\sin^2 \theta}{\overline{\eta_e^2}} + \frac{\cos^2 \theta}{\eta_o^2} \quad (3-4)$$

Where $\overline{\eta_e}$ is the mean value of the refractive index of the extraordinary ray.

From equation (3-4) one finds that for $\theta = 90^\circ$, $\eta_e(\theta) = \overline{\eta_e}$, and one obtains as well that $\eta_e(\theta) = \eta_o(\theta)$ when $\theta = 0$.

If $\eta_e(\theta) < \eta_o(\theta)$, the fundamental beam is associated with the ordinary ray (horizontal polarisation) and the harmonic wave is associated with the extraordinary ray (vertical polarisation). If the optical-axis and propagation vector (\mathbf{k}) are neither parallel nor perpendicular to each other, the ordinary ray and extraordinary ray tend to diverge from each other. This effect is referred to as "walk-off".

The refractive index of some crystals depends on their temperature. Therefore, by adjusting the temperature of the crystal phase matching at the operating wavelengths can be achieved (see e.g. Silfvast, 2004). It also means, that to maintain optimum conversion efficiency using angle-tuning, the temperature of the crystal needs to be stabilized.

3.2.3: Second harmonic generation

In second harmonic generation the two photons are equal, $\omega_1 = \omega_2 = \omega$. Thus, the phase matching condition for this case is

$$k(2\omega) = 2k(\omega),$$

And the phase velocity of the incident photon and the second harmonic wave must be equal, i.e.

$$v_{ph}(2\omega) = v_{ph}(\omega).$$

This happens when the extraordinary index $\eta_e(2\omega)$ of the second harmonic wave is equal to the ordinary index $\eta_o(\omega)$ of the fundamental wave. If the incident wave propagates through the crystal, the polarization $P(2\omega, r)$ combines in phase and the second harmonic wave at the frequency (2ω) will be developed as an extraordinary wave. According to the arguments used in section 3.2.2, the polarization direction of the second harmonic wave is orthogonal to the polarisation of the fundamental wave.

3.3: The dye laser system

3.3.1: Layout of the dye laser system

The LP3002 dye laser system contains a grating-tuned oscillator and associated preamplifier (in the same dye cell), plus a main amplifier. The pump beams entering the two dye cells are directed as shown schematically in Figure 3.18. The overall system, for oscillator-only operation, is shown in Figure 3.19.

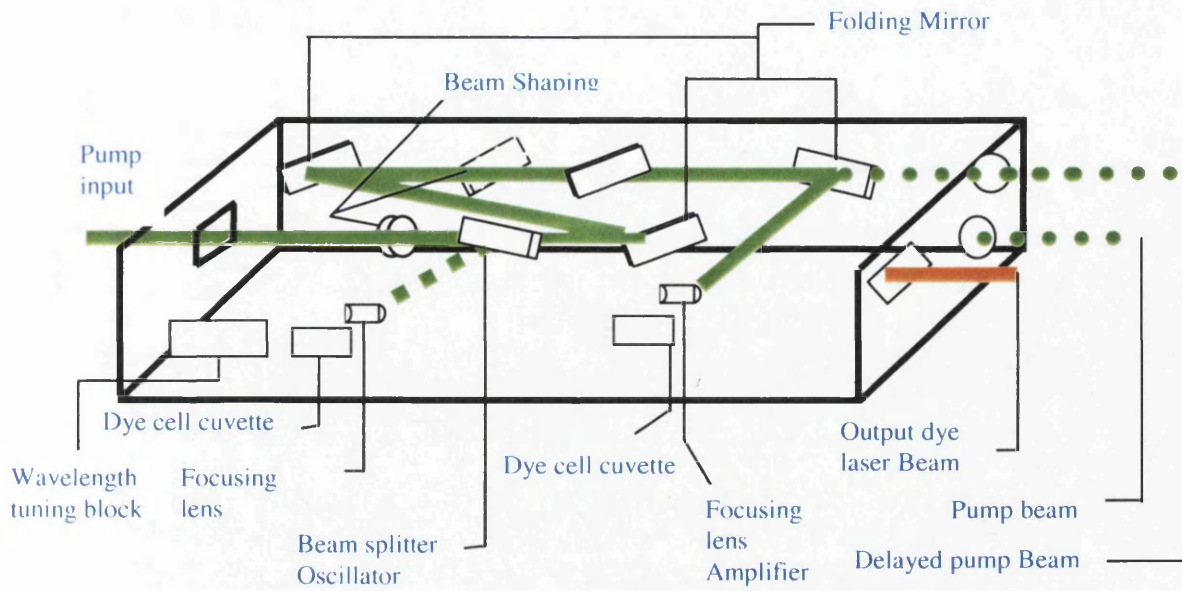


Figure 3.18: Layout of the dye laser (Instruction Manual, Lambda Physik, FL -1b)

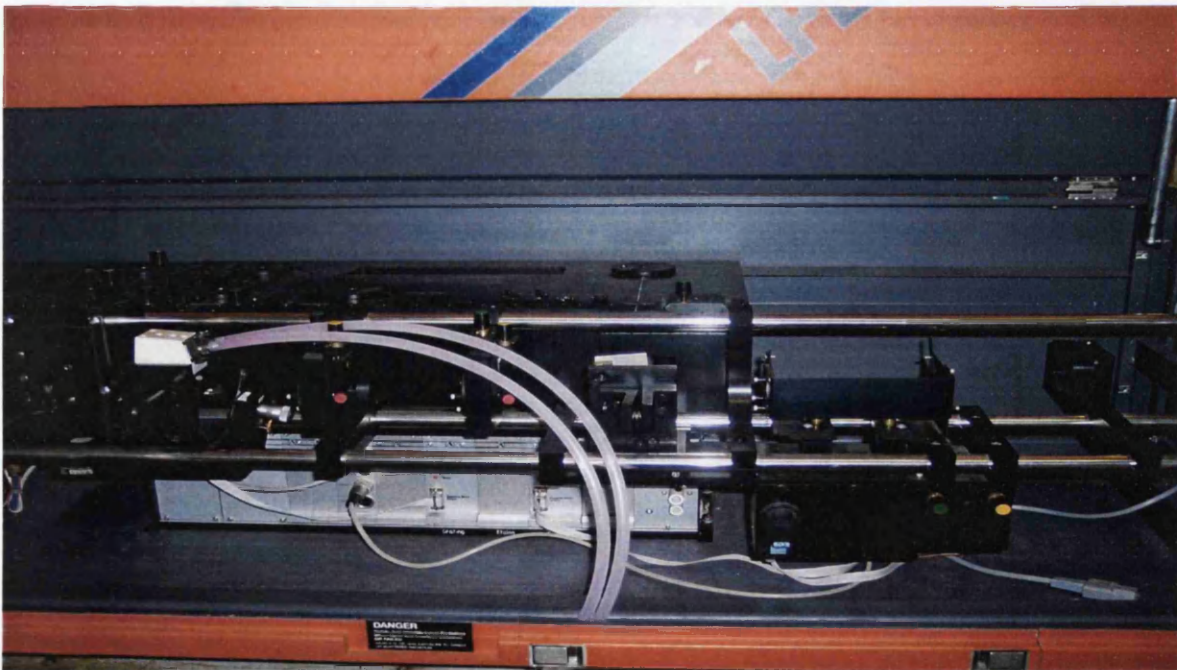


Figure 3.19: FL 3002 dye laser, which is used in the experiment (here only shown with the oscillator / pre-amplifier dye cell installed).

Note that the beam from the Nd:YAG laser needs to be adapted to the cell dimensions. For this a telescope is used in the input beam. The 2nd harmonic at 532nm is expanded for this purpose to 20mm in width, to be suitable for pumping the dye laser. The telescope consists of two cylindrical lenses (see Figure 3.20), one of them is a divergent lens with focal length $f = -30$ and the other is a convergent lens with focal length $f = 100$.

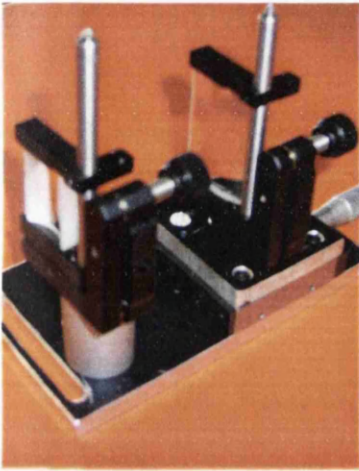


Figure 3.20 a: The telescope, which is used to expand the 532nm pump beam.

3.3.2 Dye laser components

1. Oscillator/ preamplifier

The oscillator determines the wavelength of the radiation, and therefore it is the most significant part of the tuneable dye laser.

The oscillator consists of a grating for wavelength selection, a prism beam expander, a dye flow cell which contains the active medium, and a mirror coated to cover the whole spectral range.

The dye-flow cell is a mounted and adjusted unit. It consists of (i) Head with flow body,(ii) Fused silica cuvette (20mm), and (iii) Frame.

The wavelength tuning block is positioned in the left side of the dye laser (see Figure 3.18 / 3.19). Its grating is used in third to eighth order, to achieve high spectral resolution.

The overall geometry of the dye laser oscillator is shown in Figure 3.21.

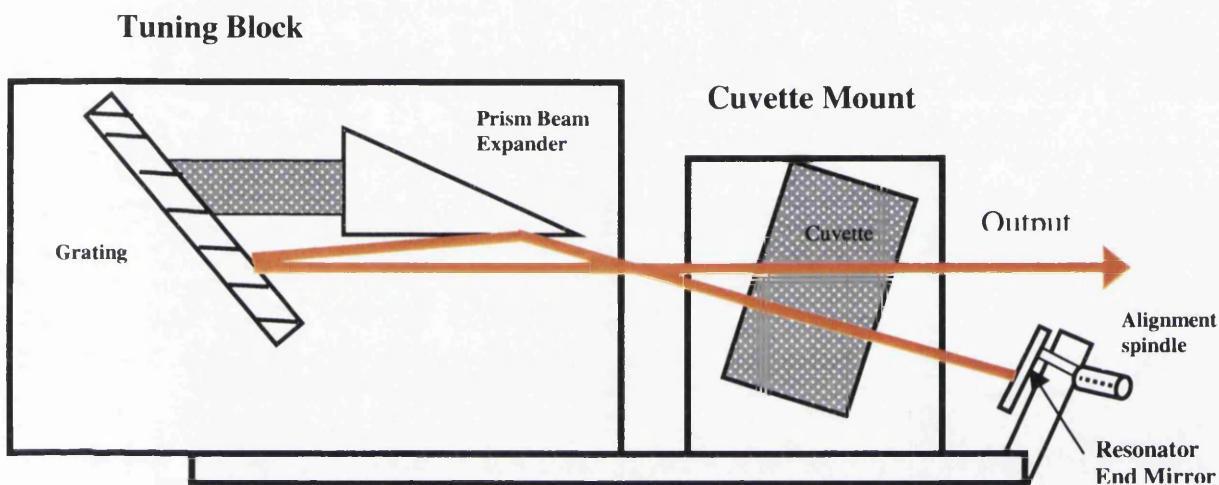


Figure 3.21: Schematic of the FL3002 dye laser oscillator.

2.Main Amplifier. The amplifier includes a flow cuvette with 40mm wide. However, this second amplification stage was not used in this study.

3.Dye selector. The dye selector consists of a reservoir, filter, and cooling water circuit.

The connection to the dye cell is realized by tubes of diameter 10mm. The unit is shown in Figure 3.22.

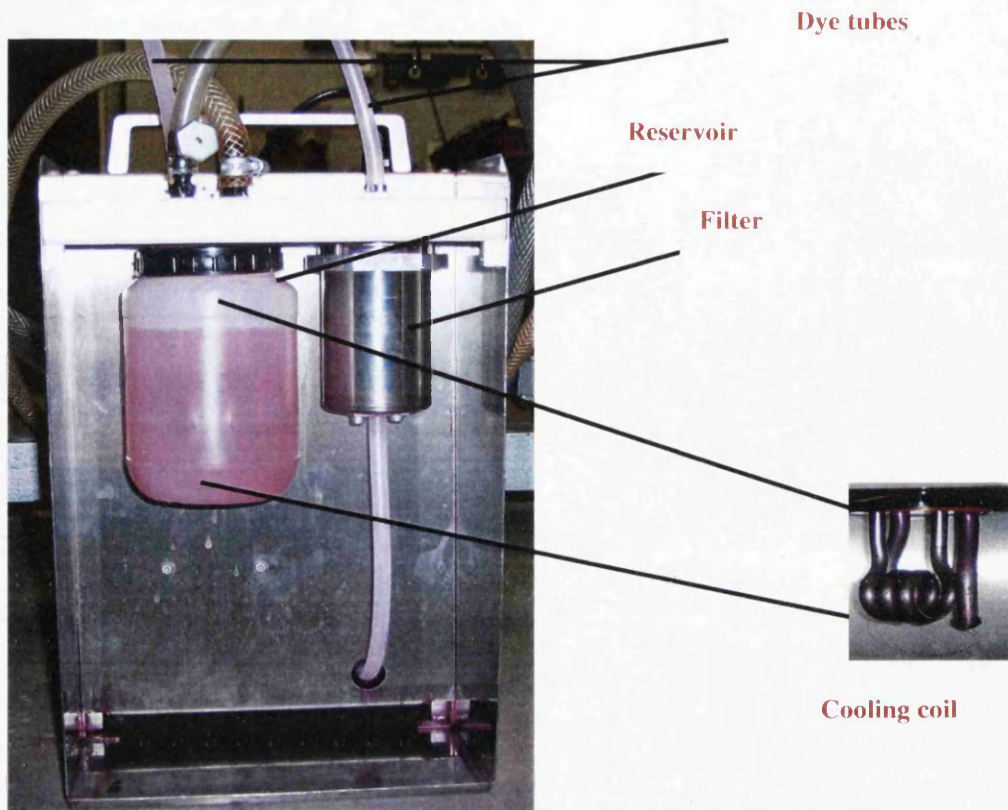


Figure 3.22: Dye selector.

All the dye tubes (material polypropylene), which are connected from the reservoir to the filter, and from the dye selector to the cuvette cells, as well as the cooling tubes, had to be changed because of age. Water is used to cool the dye laser system.

4. **Laser dyes:** Rhodamine B is used in the dye laser as active medium.

Chapter 4: Characterization of the Nd: YAG laser system

4.1: General remarks

The set up for the Nd: YAG laser system in this work is designed to generate pulses of wavelengths at 1064nm, 532nm and 355nm. The operating parameters (pulse energy and pulse width, fluences, and power density for 1064nm, 532nm, and 355nm) are reported in this chapter. Comparisons of the beam profile for the fundamental beam at 1064nm, 2nd harmonic generation at 532nm, and 3rd harmonic generation at 355nm were carried out. Furthermore, a telescope to diverge the beam in one direction (for use with the dye laser) was set up.

4.2: Set up for the Nd: YAG laser

4.2.1: Adjustment of the optical axis

For all units (Quantel Brilliant Nd: YAG laser, Harmonic Generator, and Harmonic Separator) mounts were designed to achieve a common height of the laser beams of 75mm above the breadboard. The beam height of 75mm is chosen because of compatibility reasons: the mounts (KC1/M) exhibit 25mm height from the center; the pillar posts (RS2) are made with 40mm height, as shown in the figure below; 10mm is the height of the base plate (BA1). Thus, the height of laser beam is 75mm from the breadboard, matching the center of all mounted components.

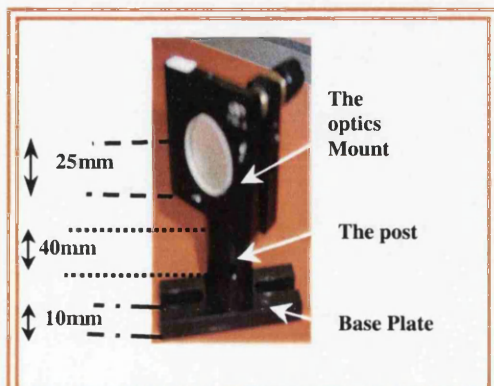


Figure 4-1: Heights of mount, post and base plate.

1. **Quantel Brilliant Nd: YAG laser:** Its base was measured to be 43mm from the center of the aperture. Thus, the laser was raised to an optical axis of 75mm using small pillars and BA1 base plates (see Figure 4.2).

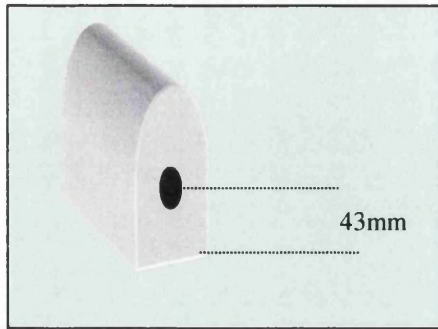


Figure 4-2a

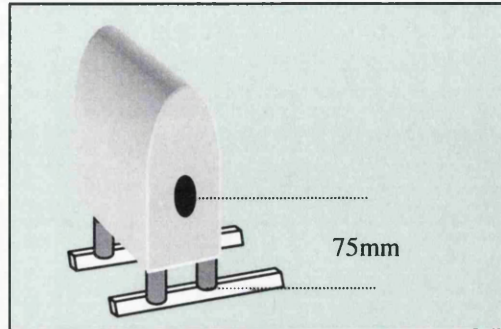


Figure 4-2b

2. **Harmonic Generator:** Its optical axis was measured to be 89mm; therefore, the mount was reduced by 14mm to achieve 75mm.

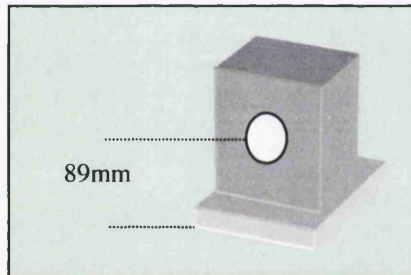


Figure 4-2c

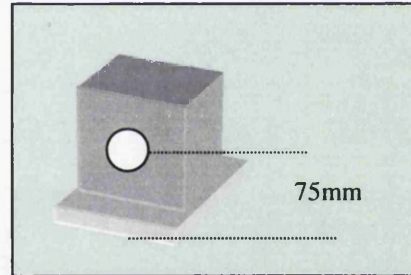


Figure 4-2d

3. **Harmonic Separator:** Its beam axis was measured at 44mm, similar to that of the Nd: YAG laser; the unit was raised 75mm by pillars and BA1 base plates.

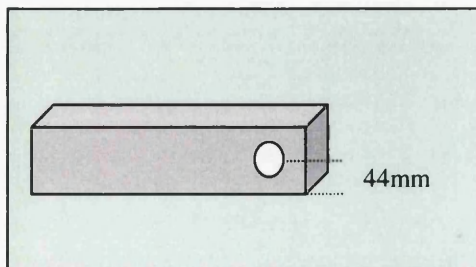


Figure: 4-2e

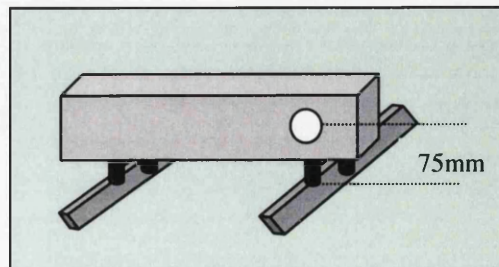


Figure: 4-2f

4.2.2: Adjustment of the laser beam

This section is related to the beam steering after the laser beam has left the source. It has to be reflected into the harmonic generator and adjusted in the right position so as to emerge correctly from the crystals. The harmonic separator needs adjustment of its Pellin-Brocca prism, and its right angle prisms (90° and 180° deflection). The Pellin-Brocca prism is rotated, to the right or the left, up or down to receive and reflect the three wavelengths at the correct angle. A right angle prism (180° deflection) is used to reduce the system dimension, always preserving 75mm beam height. It is moved forward or backward until the laser beams are in the right position. Adjusting a further set of right angle prisms (90° deflection) forward or backward, the beams at 532nm and 355nm are leaving the beam separator at right angle and can be used simultaneously (see Figure 3.8).

Note that during alignment protective eyewear must be used because of the potential exposure to hazardous Class 4 laser radiation.

4.2.3: Optimisation of the 2nd and 3rd harmonic pulse energy

1. Second harmonic generation adjustment

A. The 2nd harmonic crystal is mounted in the optical axis of the fundamental beam (1ω) at 1064nm; for this crystal a translation arm is moved downwards.

B. Rotate the angle tune until the green beam becomes brightest (this means, phase matching is achieved).

C. The pulse energy of the 2ω output beam is measured and the maximum reading (peak energy) is recorded.

2. Third harmonic generation adjustment

Both the crystal translation arms of the 2nd harmonic crystal and the 3rd harmonic crystal are pushed down, so that both crystals are in the optical axis. The tune angle of the 3rd harmonic crystal is adjusted until "blue" fluorescence on a piece of white paper becomes brightest. As in the case of 2nd harmonic generation, the 3rd harmonic pulse energy is measured and the angular position recorded at which the maximum value in pulse energy is achieved.

4.2.4: Time delay between flashlamp and Q-switch operation

Naturally, there is a delay in time between the flashlamp pulse and the Q-switch trigger. With an oscilloscope this time was measured, as shown in Figure 4-3, where channel 1 represents the flashlamp trigger pulse and channel 2 is representing the Q-switch pulse.

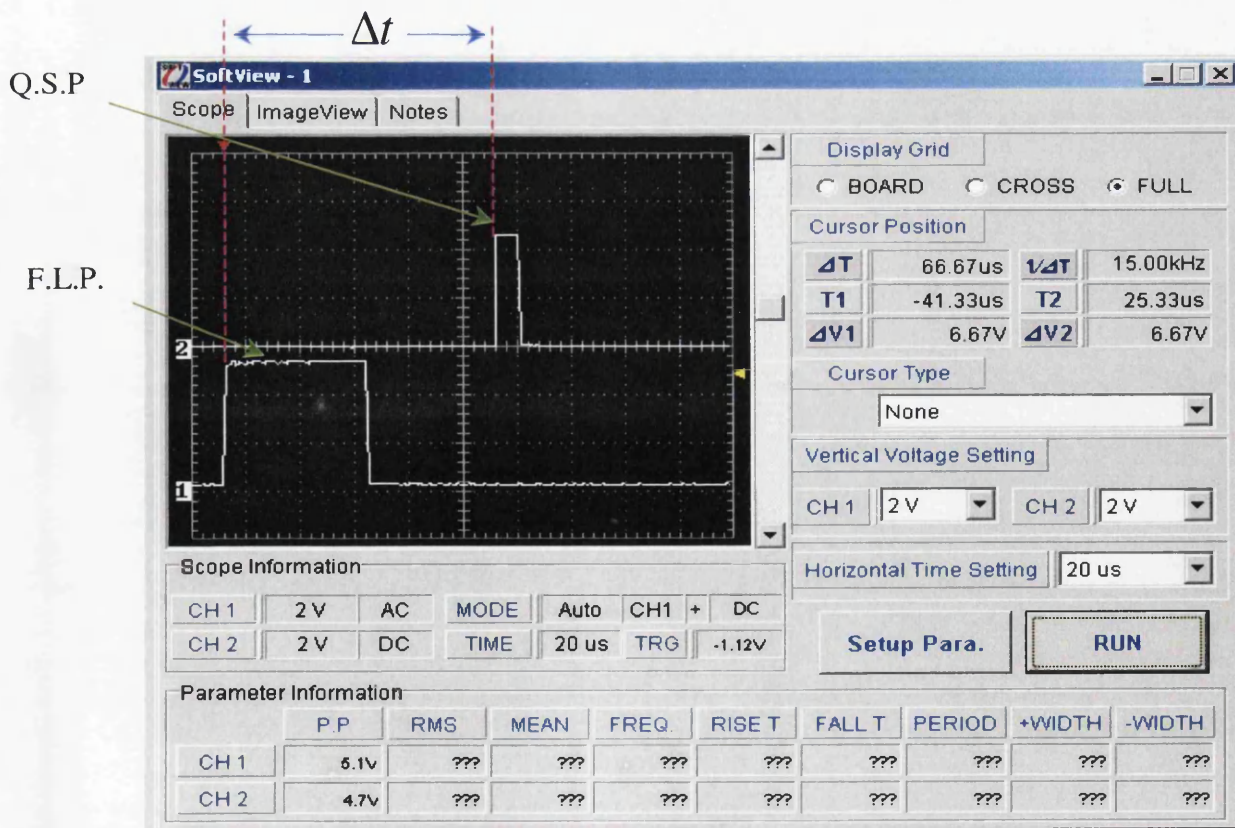


Figure 4-3: Time delay between flashlamp and Q-switch pulses.

The delay interval is measured between the leading edges of the two pulses. At these instances the flashlamp and the Q-switch commence, respectively. Note, that the oscilloscope determines the delay between the centers of the pulses, and the value of $(+24-8) = 16\mu\text{s}$ needs to be added to the readings. There is a proportional relation for the time delay between the flashlamp and the Q-switch pulses, which can be adjusted using a dial. The position of the Q-switch pulse can be changed relative to the position of flashlamp pulse. The delay between flashlamp and Q-switch pulses increases linearly with dial setting (see Figure 4-4).

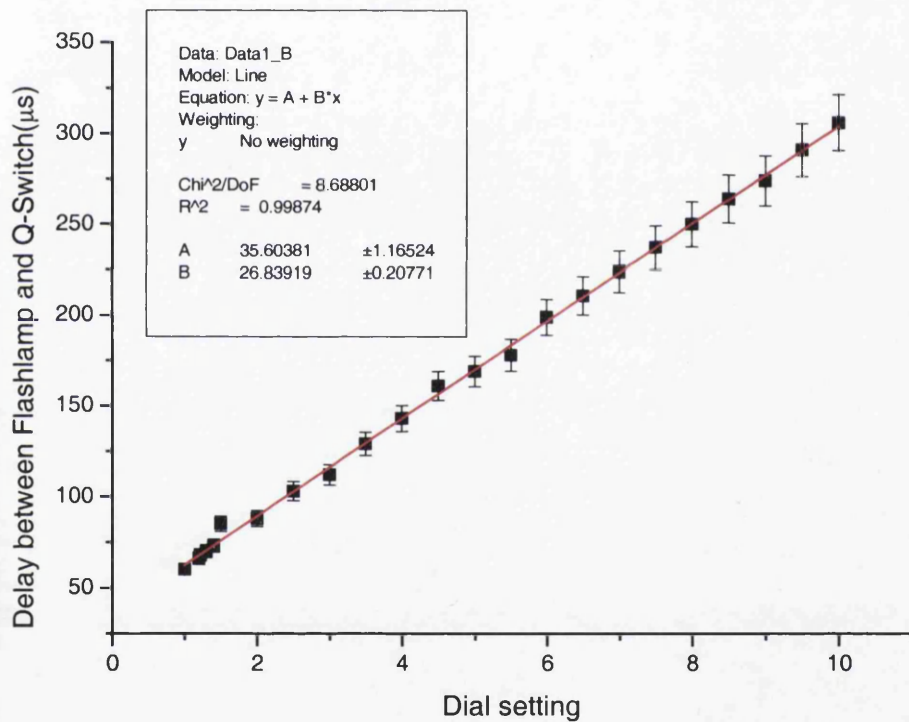


FIGURE 4-4: Delay Time between flashlamp and Q-switch pulse, in μs . A linear fit with equation $y = A + B \cdot x$ is included.

The actual delay with respect to the dial reading is

$$\Delta t = \text{Slope}(B) \times \text{dial setting} [\mu\text{s}] + \text{Offset} (A)$$

The actual values of the parameters are shown in the Figure 4-4.

4.3 Pulse energy measurements

An energy probe is used to measure the pulse energy, E_p ; a divergent lens has to be placed in front of the energy probe to avoid damage to its coating.

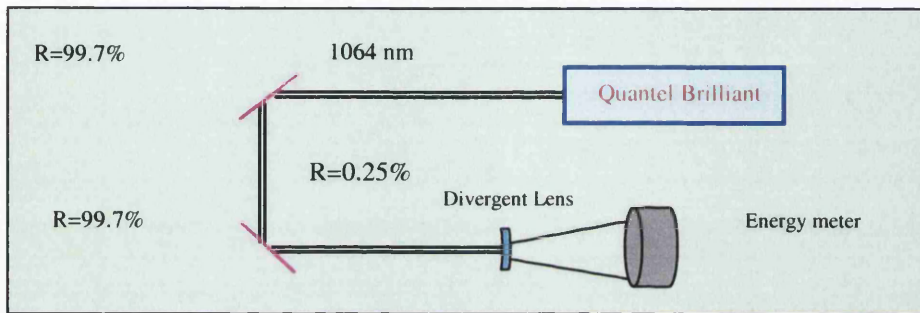


Figure: 4-5: Layout for E_p measurement, exemplified for the fundamental beam at 1064nm.

Increasing the reading of the adjustment (dial)¹ of the power supply, the pulse energy rises to the maximum value in the pulse energy of 102mJ at dial setting 5.5. Note that the same behaviour of the pulse peak energy for the fundamental beam at 1064nm is also found for the peak energies of the 2nd and 3rd harmonic generations at 532nm and 355nm. Some energy is lost because of the mirrors and the lens; these losses can be calculated; as is outlined in Chapter 3.

¹ Dial is the delay position between flashlamp and Q-switched pulses.

4.3.1 Pulse energy of the fundamental beam at 1064nm

There are two beams profiles of Nd: YAG at 1064nm laser shown in Figure 4-6. Either profile was taken when the dial was set to 5. Profile-a- is taken before the laser has thermally stabilised (after only 7 minutes warming up) while profile -b- is taken after the laser has fully thermalised (after ~ 25minutes warming). There is hardly any difference in output energy as function of flashlamp / Q-switch delay, whether the laser has stabilised or not. However, the beam profile, and with it the power density change dramatically, as Figure 4-6 reveals. Profile -b- is more even than that of profile-a-, although the pulse duration for both profiles was ~ 3ns. The diameter of the burn pattern is found to be 6mm in both cases; these burn pattern do not completely reveal the actual Gaussian beam profile, due to the "on/off" behaviour of the paper over wide ranges of power density.

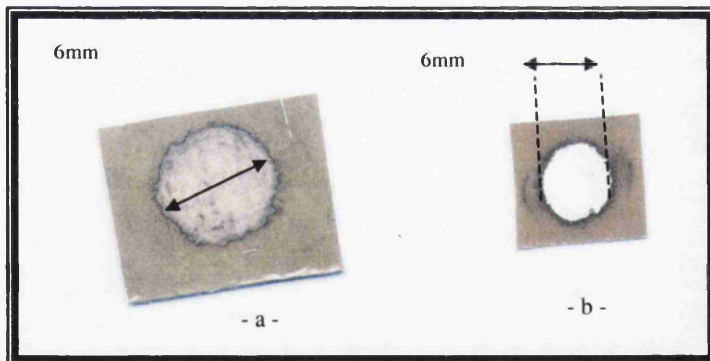


Figure: 4-6: Beam profile of Nd: YAG laser at 1064nm.

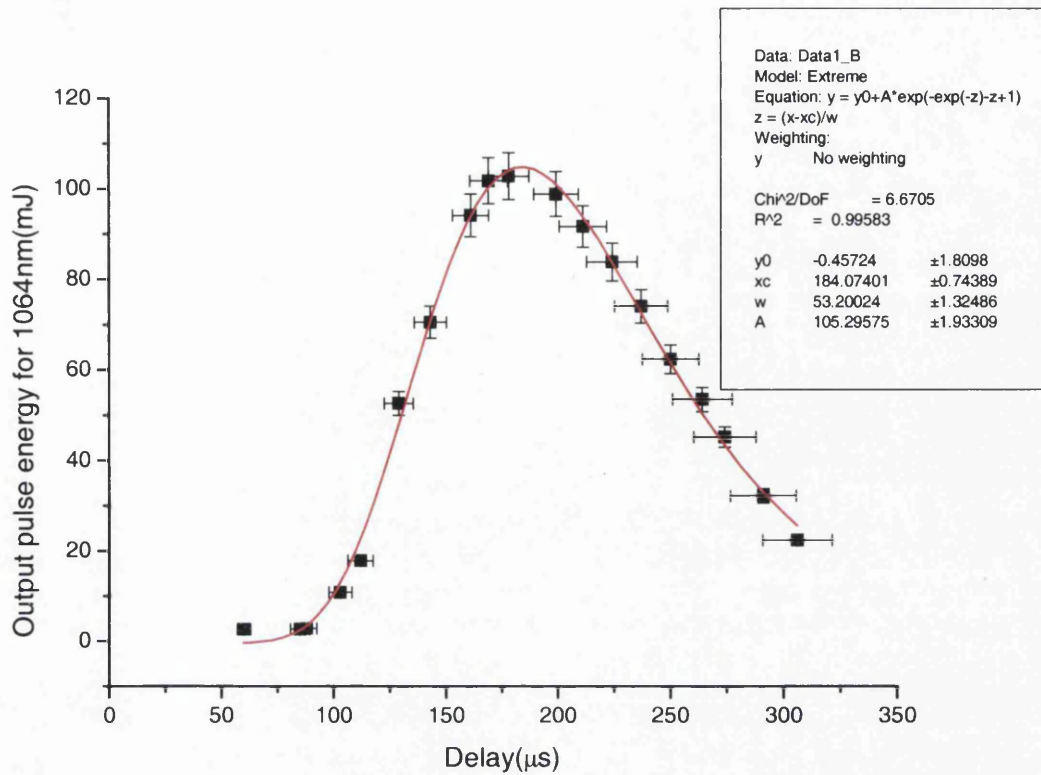


Figure 4-7: Output of the pulse energy for fundamental laser beam at 1064nm, after warm-up.

The total energy of the fundamental at 1064nm is

$$E(1\omega) = E_p + (0.3\% + 0.3\% + 0.25\%) E_p \quad (4-1)$$

Here E_p is the measured pulse energy value and the losses are those of the two mirrors and the AR-coated diverging lens, which need to be factored in to obtain the real $E(1\omega)$.

An Origin program is used to fit the measured curve of the output pulse energy at 1064nm with the equation shown in the insert of Figure 4-7.

While this function has no direct physical meaning, other than reflecting the increase in population inversion with time and its decay after termination of the flashlamp, the fit is useful to determine the maximum pulse energy value and its position.

The curve shown in Figure 4-7 represents the pulse energy versus time delay between the flashlamp (FL) and the Q-switch (Q-S); for the calibration of the dial and time delay see Section 4.2.4.

The pulse energy increases slightly up to the value of about 102 mJ; at this point the laser emits its optimum pulse energy, peak power and the clearest burn pattern on the burn paper is observed. This value of pulse energy occurs when the position between FL and Q-S indicates to number 5.5 on dial; this reading is equivalent to a delay of $\cong 178 \mu\text{s}$ delay in time. The pulse energy declines slowly with increasing change in the delay between FL and Q-S to become 10 on the dial (equivalent to 300 μs), when the pulse energy is recorded to be 22.3 mJ.

4.3.2 Pulse energy of the 2nd harmonic beam at 532nm

The pulse energy of the 2nd harmonic at 532nm is measured and found to peak at $\sim 68 \text{ mJ}$ when the delay dial was set to 5.5, equaling $\cong 178 \mu\text{s}$ time delay.

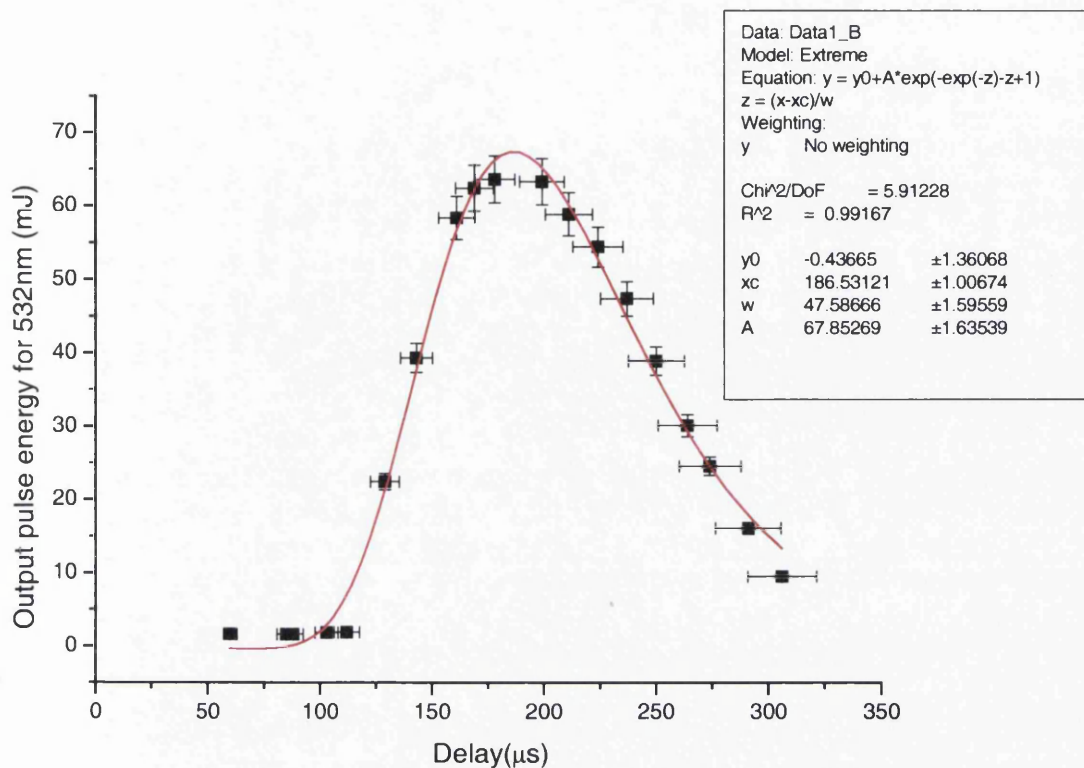


FIGURE: 4-8: Output pulse energy of the 2nd harmonic generator at 532nm.

As for the fundamental wave, the pulse energy curve is fitted to the equation as shown in the insert of Figure 4-8. The peak energy of $\sim 68\text{mJ}$ is found at $\Delta t \cong 187\mu\text{s}$.

The actual total energy of the 2nd harmonic generation is difficult to determine. It would be $E(2\omega) = E_p + (0.3\% + 0.3\% + 0.25\%)E_p$ if the configuration were as in the measurements for the fundamental wave. However, now the harmonics separator (see Figure 4-9) is included, which adds an unknown amount of losses, although one could roughly calculate the values from the different prim surfaces (which are uncoated). The H.S. losses can crudely be estimated to be $\sim 20\%$. A small pulse detector and an

oscilloscope are used to measure the energy of pulses that are less than 4mJ. The oscilloscope reading must be converted to units of energy; according to the relation

$$E_p = E \text{ (V)} / 78.5 \text{ (V/J)} \quad (4-2)$$

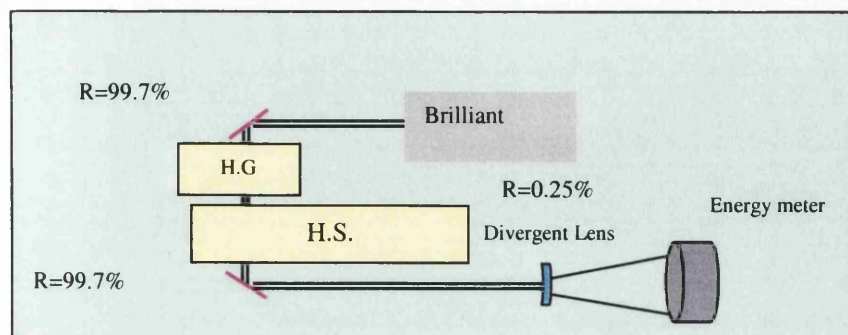


Figure: 4-9: Layout for E_p - measurement of the 2nd harmonic generation at 532nm.

The "Gaussian" intensity profile of the 2nd harmonic generation at 532nm is as shown in Figure 4-10.

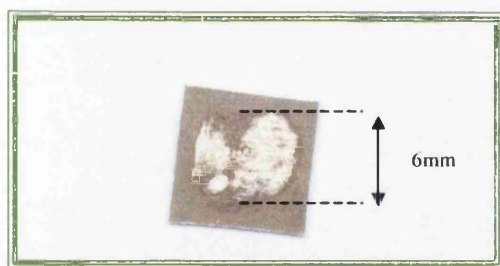


Figure: 4-10: Laser profile of the 2nd harmonic at 532nm.

The diameter of the 2nd harmonic profile at 532nm is found to be ~ 6mm over 30 pulses. Note that the beam profile is not homogeneous but rather patterned. This is most likely do to damage to the crystal surface, which can be seen when looking at the crystals. The hygroscopic crystals most likely have suffered damage over the years, due to absorption of water from the humid air in Swansea.

4.3.3 Pulse energy of the 3rd harmonic beam at 355nm

The pulse energy of the 3rd harmonic output started very low at about 1.2 mJ, at 60 μ s time delay. The pulse energy rises slowly up to 3.2mJ at 112 μ s time delay and then increases sharply as noticed in the curve in Figure 4-11, up to the peak energy of \sim 27mJ at \cong 143 μ s delay, and then decreasing gradually for larger delays.

As for the 532nm wave; the beam separator contributes losses in the measurements, which can be estimated as \cong 20%.

The beam profile of the 3rd harmonic wave at 355nm is displayed in the Figure 4-12, exhibiting an asymmetric pattern of 5mm by 3mm. The pattern is generated by averaging over 30 pulses.

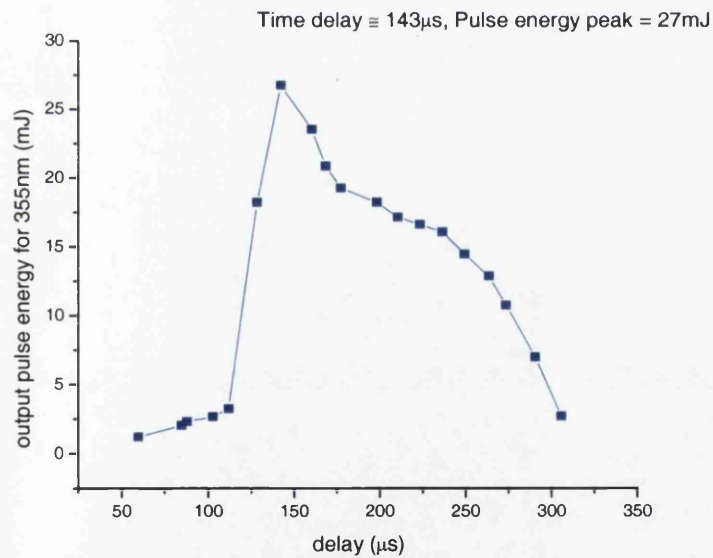


Figure: 4.11: Output pulse energy of the 3rd harmonic generator at 355nm

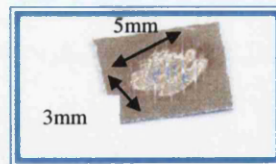


Figure: 4-12: laser profile of the 3rd harmonic output at 355nm

4.3.4 Summary of pulse energy output data

A comparison between the three pulse energy curves is given in Figure 4.13, revealing the conversion efficiency for the two harmonics.

The maximum pulse energy for the fundamental beam at 1064nm is measured as 102mJ, while the maximum energy for 2nd harmonic generation is measured to be 63mJ. The experimental results thus shows that the maximum efficiency of the ω to 2ω conversion is about 60%, while the efficiency of the 3ω generation is found to be $\cong 35\%$ at delay $\sim 140\mu\text{s}$, but less than 20% at the delay of $\sim 100\mu\text{s}$, for which maximum conversion would be expected. As discussed further below thermal effects could be one reason for this. Also, the damage to the crystal surfaces could influence the overall conversion.

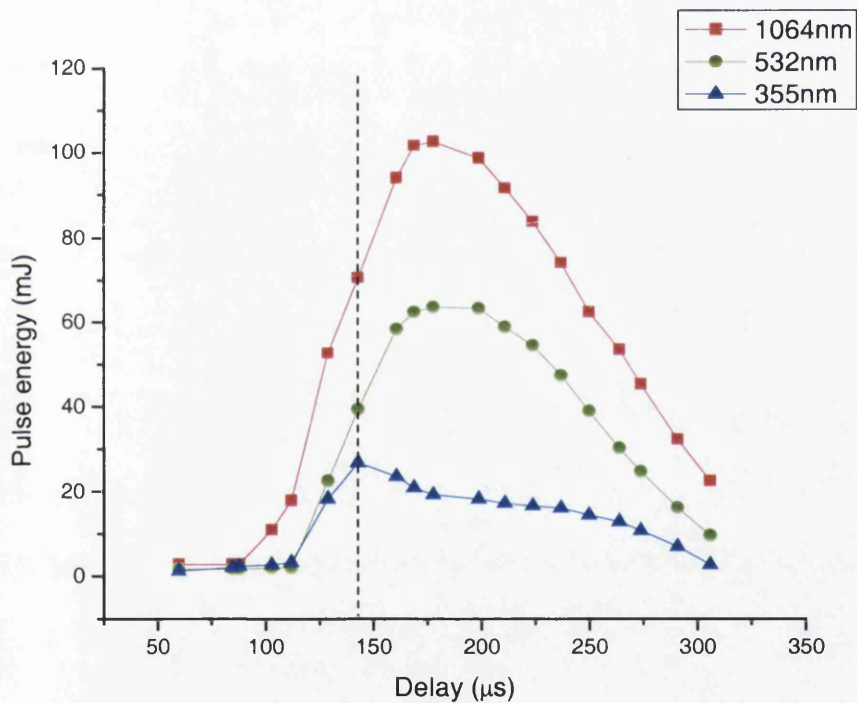


Figure 4-13: Output pulse energies of 1064nm, 532nm, and 355nm versus to the delay.

It is not quite clear, why the pulse energy curve for the 3rd harmonic behaves as shown in Figure 4.11 and 4.13. One would expect that $E(3\omega) \propto E_p(2\omega) \times E_p(\omega)$, where $E_p(\omega)$

would be the non-converted energy left over from the 2nd harmonic generation, i.e. (trace in Figure 4.7) – (trace in Figure 4.8). This is evaluated in Figures 4.13 and 4.14. As seen in the last figure, the "kink" in the output pulse energy curve is not reproduced. A possible explanation may be that the 3rd harmonic crystal undergoes thermal variations when exposed to the varying amount of input energy, which would affect the phase matching conditions. The remainder curve is the subtraction of the intensity of 2nd harmonic from the intensity of the fundamental wave is given in the Figure 4-14.

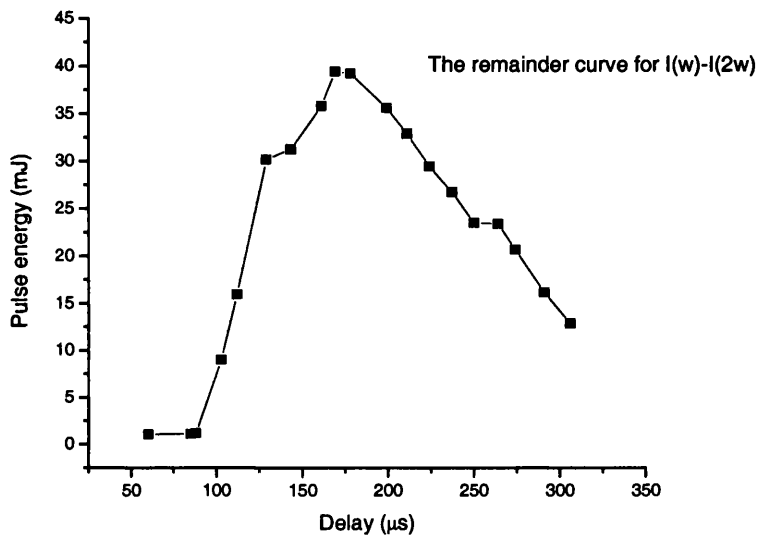


Figure 4-14: The remainder curve of $I(w) - I(2w)$.

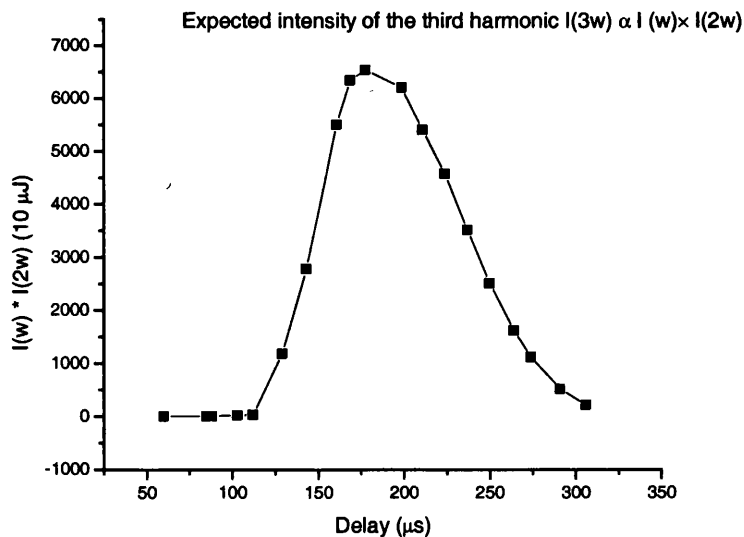


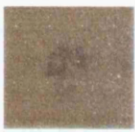
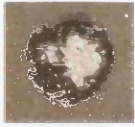
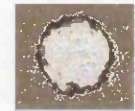
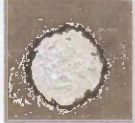

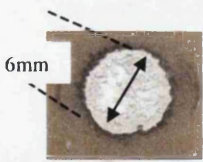

Figure 4-15: The result multiplication curve of $I(w) * I(2w)$.










4.4: Determination of beam profiles by burn patterns

1. The fundamental beam at 1064nm

Different burn patterns are observed for the fundamental beam at 1064nm depending on the position of the dial of laser source, i.e. the delay and associated with it the pulse energy.

Table 4.1: Burn patterns for the fundamental beam at 1064nm.

Picture	Damage threshold	Delay setting / E_p	Remark
A		103 μ s / 10.9mJ	The intensity of the beam is lower than the damage threshold of the burn paper.
B		112 μ s / 17.9mJ	This picture reveals the beginning of the paper damage threshold (for a dial setting of 3).
C		129 μ s / 52.6mJ	Increase in homogeneity of the burn pattern
D		143 μ s / 70.6mJ	Increase in homogeneity of the burn pattern
E		161 μ s / 94.2mJ	Increase in homogeneity of the burn pattern
F		169 μ s / 101.9mJ	(This picture shows homogeneous damage across the profile, it is taken when the dial setting is 5). The radii of the burn paper in picture f and picture g are measured as 6mm; they are the largest value of diameter.
G		178 μ s / 102.9mJ	

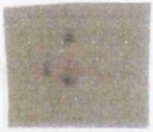



H		199 μ s / 98.9mJ	The homogeneity of the profile decreases with lower pulse energy.
I		211 μ s / 91.8mJ	The homogeneity of the profile decreases with lower pulse energy.
J		224 μ s / 83.9mJ	The homogeneity of the profile decreases with lower pulse energy.
K		237 μ s / 74.1mJ	The homogeneity of the profile decreases with lower pulse energy.
L		250 μ s / 62.4mJ	The homogeneity of the profile decreases with lower pulse energy.
M		264 μ s / 53.6mJ	The homogeneity of the profile decreases with lower pulse energy.
N		274 μ s / 45.3mJ	The homogeneity of the profile decreases with lower pulse energy.
O		291 μ s / 32.3mJ	The homogeneity of the profile decreases with lower pulse energy.
P		306s / 22.4mJ	The homogeneity of the profile decreases with lower pulse energy.





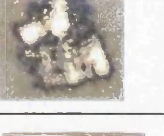

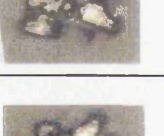
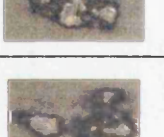

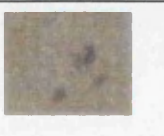

Summary: The burn patterns of the paper increase in homogeneity quickly with increasing delay, i.e. pulse energy; they roughly follow the intensity curve shown in Figure 4-6. It should be noted that the apparent homogenous profile of the burn pattern do not reflect the real laser beam profile. Because of the high energy density the burn threshold switches "on" or "off", rather than following the expected Gaussian beam profile.

2. The 2nd harmonic output beam at 532nm

The burn patterns registered for the second harmonic outputs from the laser system are collected in table 4.2.

Table 4.2: Burn pattern for the 2nd harmonic generation at 532nm.

Picture	Damage threshold	Delay setting / E_p	Remark
A		112 μ s / 3.9mJ	The intensity of the beam is less than the damage threshold of the burn pattern.
B		129 μ s / 22.5mJ	Increase in homogeneity of the burn pattern.
C		143 μ s / 39.3mJ	Increase in homogeneity of the burn pattern.
D		161 μ s / 58.4mJ	Increase in homogeneity of the burn pattern.






E		169 μ s / 62.4mJ	Increase in homogeneity of the burn pattern.
F		178 μ s / 63.6mJ	This picture appears as the clearest and brightest of the burn profiles, the intensity of the beam is the highest.
G		199 μ s / 63.3mJ	The homogeneity of the profile decreases with lower pulse energy.
H		211 μ s / 58.9mJ	The homogeneity of the profile decreases with lower pulse energy.
I		224 μ s / 54.5mJ	The homogeneity of the profile decreases with lower pulse energy.
J		237 μ s / 47.4mJ	The homogeneity of the profile decreases with lower pulse energy.
K		250 μ s / 38.9mJ	The homogeneity of the profile decreases with lower pulse energy.
L		264 μ s / 30.2mJ	The homogeneity of the profile decreases with lower pulse energy.
M		274 μ s / 24.6mJ	The homogeneity of the profile decreases with lower pulse energy.
N		291 μ s / 16.1mJ	The homogeneity of the profile decreases with lower pulse energy.
O		306 μ s / 9.6mJ	The intensity of the beam falls below the damage threshold of the burn paper.










Summary: It clear from the pictures of the burn pattern that there is damage in the harmonic crystal. All of theses pictures are generated by averaging over 10 laser pulses.


3. Third harmonic output beam at 355nm:

The burn patterns registered for the third harmonic output from the laser system are summarised in table 4.3.

Table 4.3: Burn pattern of the 3rd harmonic generation at 355nm.

Picture	Damage threshold	Delay setting / E_p	Illustration
A		112 μ s / 3.2mJ	In this picture the beam intensity is too weak to generate a burn pattern.
B		129 μ s / 18.2mJ	The intensity of the beam is just exceeded the damage threshold of the burn paper.
C		143 μ s / 26.8mJ	The clearest damage threshold is shown in this picture because the intensity is at its maximum.
D		161 μ s / 23.5mJ	The homogeneity of the profile decreases with lower pulse energy.
E		169 μ s / 20.9mJ	The homogeneity of the profile decreases with lower pulse energy.

F		178 μ s / 19.3mJ	The homogeneity of the profile decreases with lower pulse energy.
G		199 μ s / 18.2mJ	The homogeneity of the profile decreases with lower pulse energy.
H		211 μ s / 17.1mJ	The homogeneity of the profile decreases with lower pulse energy.
I		224 μ s / 16.6mJ	The homogeneity of the profile decreases with lower pulse energy.
J		237 μ s / 16.1mJ	The homogeneity of the profile decreases with lower pulse energy.
K		250 μ s / 14.4mJ	The homogeneity of the profile decreases with lower pulse energy.
L		264 μ s / 12.9mJ	The homogeneity of the profile decreases with lower pulse energy.
M		274 μ s / 10.7mJ	The homogeneity of the profile decreases with lower pulse energy.
N		291 μ s / 6.9mJ	The burn pattern disappeared completely because the intensity of the beam is too weak.

O		306 μ s / 2.7mJ	The burn pattern disappeared completely because the intensity of the beam is too weak.
---	---	---------------------	--

Summary: As for the 2nd harmonic, the beam profile for the 3rd harmonic is not homogeneous. Clearly, it is related to the beam profile for the 2nd harmonic beam, i.e. it exhibits so-called "hot-spots". Whether the 3rd harmonic crystal is also damaged is difficult to ascertain from the pictures.

4.5: Gaussian beam propagation

According to the manual of the "Brilliant" laser, its fundamental beam at 1064nm should exhibit Gaussian shape (TEM_{00}), therefore the profile of the output beam should be as shown in Figure 4-16.

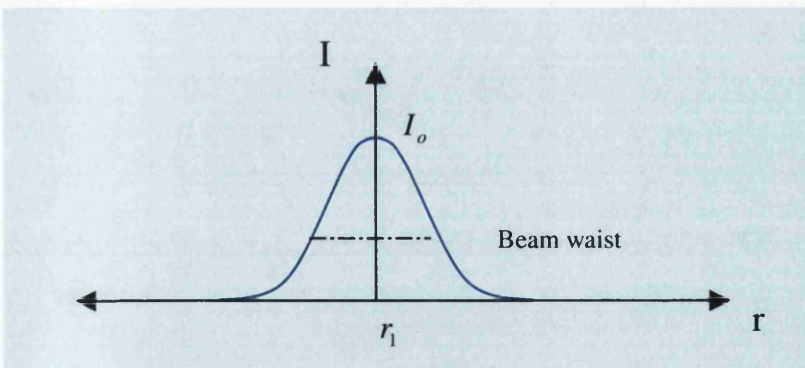


Figure 4-16: Gaussian beam profile.

The overall shape can be described by the formula

$$I(r) = I_0 \exp\left(-r^2/r_1^2\right), \quad (4-4)$$

Where r is the distance from the beam axis, r_1 is the width of the profile function, I is the intensity of the beam, and I_0 intensity of the beam at the center.

The waist of the beam is given by $W_0(z)$ where the beam has the smallest spot size along z -axis for $z=0$ (see Figure 4-17).

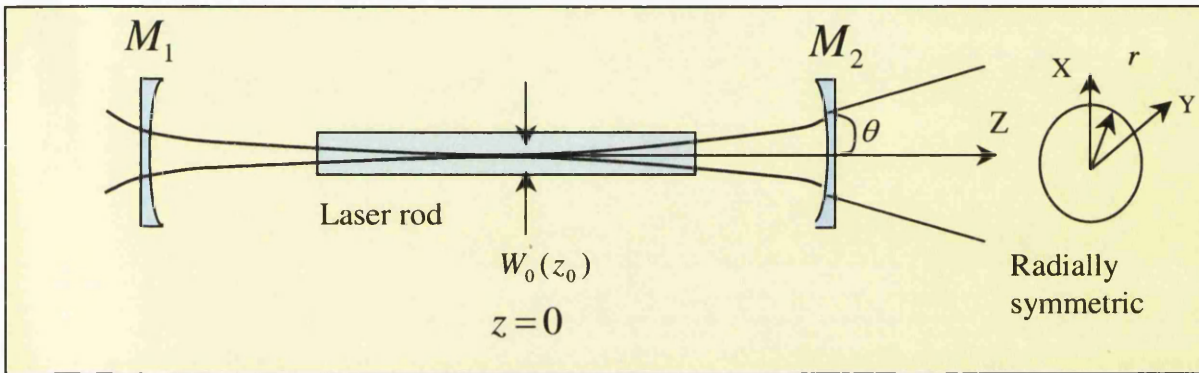


Figure 4-17: Scheme of expanding Gaussian beam.

$$W(z) = W_0 \left[1 + \left(\frac{z}{z_0} \right)^2 \right]^{1/2} \quad (4-5)$$

Where $z_0 = \frac{W_0^2 \pi}{\lambda}$ is defined as the Rayleigh length (range). The beam waist increases away from the source. For $(z \gg z_0)$, the beam waist will then be

$$W(z \gg z_0) = \frac{W_0 z}{z_0} = \frac{z \lambda}{W_0 \pi}$$

The divergence angle of the beam is given by

$$\theta = 2 \times \frac{dw}{dz} = \frac{2\lambda}{W_0 \pi}$$

4.6: Pulse width

The pulse width is determined in this work as the full width at half maximum (FWHM) of the pulses.

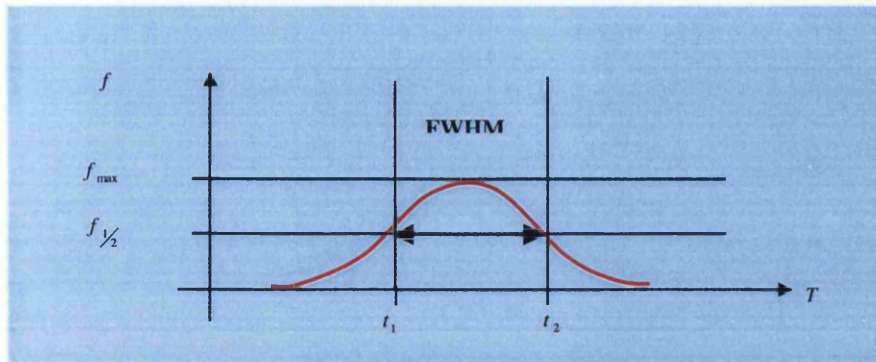


Figure 4-18: Scheme of the pulse width.

The pulse width was measured using a PIN diode, which is connected to an oscilloscope and placed close to the radiation of the laser beam; the oscilloscope gives a trace, from which the (FWHM) is extracted.

The pulse width was measured to be in the range 3ns to 4ns, as shown below in Figure 4-19. By and large the measurement data are limited in resolution by the time response of the oscilloscope used in the measurements. The overall trend in pulse duration is as expected: for short delay between flashlamp and Q-switch the population inversion is not fully developed, and hence the laser operates for only a reduced period of time, until the population inversion is depleted. The measured pulse duration is consistent with the manufacturer's specification of $\tau_p \approx 4ns$. The red lines in the graphs guide the eye.

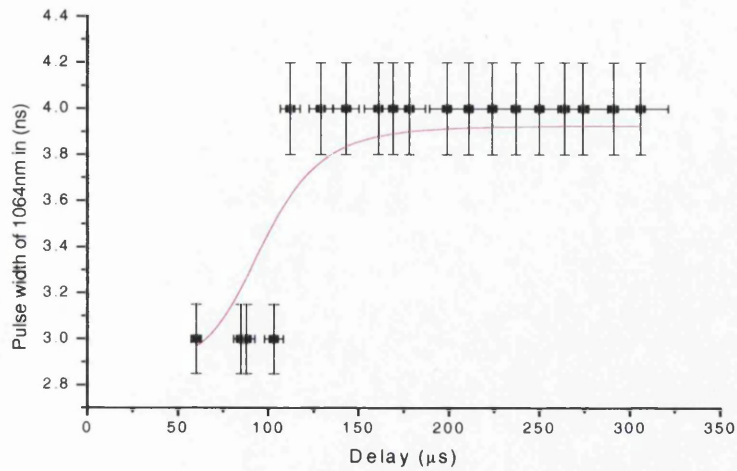


Figure 4-19: Pulse width of the fundamental output at 1064nm.

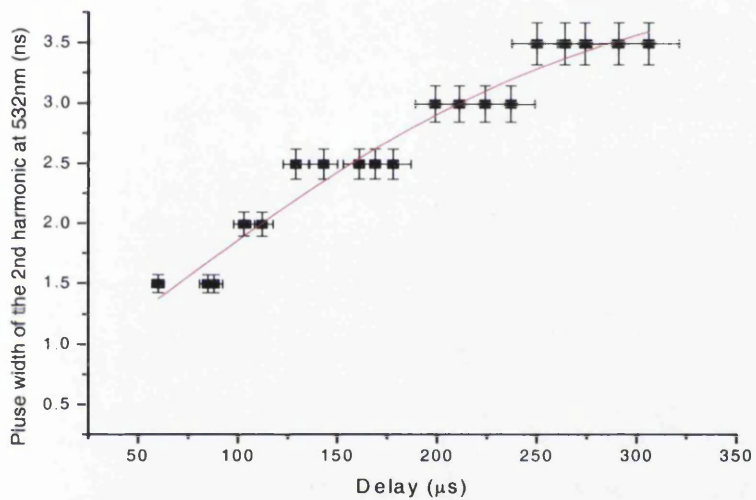


Figure 4-20: Pulse width of the 2nd harmonic output at 532nm

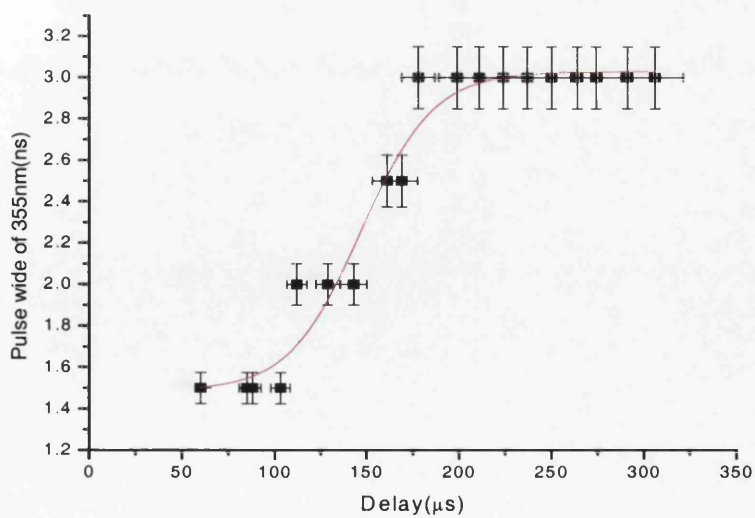


Figure4-21: Pulse width of 3rd harmonic output at 355nm.

As expected, the pulse width of the harmonics is somewhat shorter than the fundamental pulse, due to the I^2 -dependence, which affects the apparent pulse width.

4.7: Fluence of the laser beam and power density

When the pulse energy E_p is divided by the area (A) of the cross section of output beam, this gives the fluence, ϕ , in the beam:

$$\phi = \frac{E_p}{A} . \quad (4-10)$$

The cross section of the fundamental beam at $\lambda=1064\text{nm}$ is of a circular shape, as shown in Figure 4-7. Therefore, the area of the cross section is simply $A= \pi r^2$, where r is the radius of the beam, i.e. $r = \frac{D}{2} = \frac{6}{2} = 3\text{mm}$. Hence,

$$\phi = \frac{0.102\text{J}}{(3.14)(0.3)^2} = 0.36\text{J}/\text{cm}^2 \quad \text{for } 1064\text{nm}$$

$$\phi = \frac{0.064\text{J}}{(3.14)(0.3)^2} = 0.23\text{J}/\text{cm}^2 \quad \text{for } 532\text{nm}$$

$$\phi = \frac{0.027\text{J}}{(3.14)(0.25)(0.15)\text{cm}^2} = 0.23\text{J}/\text{cm}^2 \quad \text{for } 355\text{nm}$$

Note that the profile for the 3rd harmonic is very inhomogeneous, and its area has been approximated by an "ellipse".

The (peak) power density is defined as the pulse energy over time (pulse width), i.e.

$$P = \frac{E_p}{A\tau_p}, \text{ where } \tau_p \text{ is the pulse width. Using the values for the measured maximum}$$

pulse energies and using the pulse duration at the delay corresponding to this maximum, one finds the values tabulated in Table 4-4.

Table 4-4: Peak power density of laser output

Laser beam	E_p (mJ)	τ_p (ns)	$A(\text{cm})^2$	P (MW/cm^2)
ω	102	4	0.29	$\cong 88$
2ω	64	3	0.29	$\cong 74$
3ω	27	3	0.24	$\cong 39$

Finally, two cylindrical lenses with focal length -30 and $+100$ were used to set up a Galilean telescope to increase the beam from 6mm to 20mm . Note that this beam expansion is only in one beam dimension, since the lenses are cylindrical lenses.

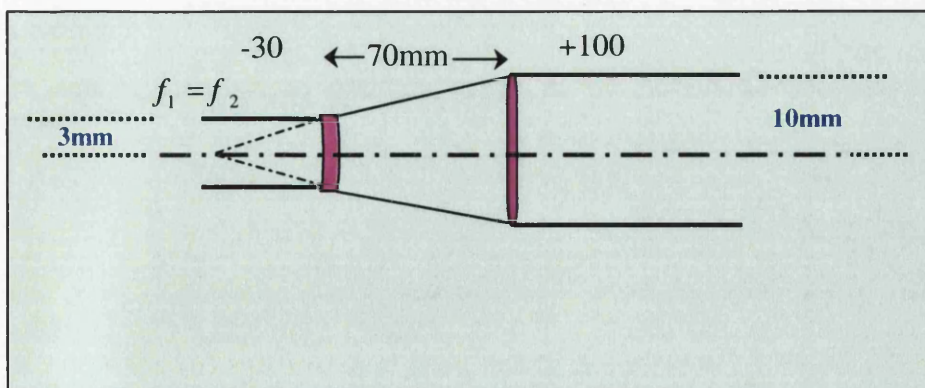


Figure 4-8: Scheme of telescope .

Chapter 5: Characterization of the dye laser system

In this chapter we briefly summarise the set up procedure for the dye laser, the alignment for the pump beam, preparation of the dye solution, and the measurement of the pulse energy from the oscillator/preamplifier of the laser, as a function of wavelength.

5.1: Alignment of the dye laser system

An alignment tool is used to check the correct location and the height of the pump beam. Using the alignment tool, the height of the beam is adjusted by first placing it in the left side of the cabinet. Then the beam is adjusted so that it goes through its centre. For the duration of the alignment the flow cuvettes are removed.

The beam enters through the rectangular input port, then to the centre of the folding mirror 1 through the beam splitter. An alignment template is hung on the dye cell crate to check the correct position of the focussed beam; for this the beam splitter is rotated and, using the v-control, is adjusted until the reflected beam falls onto the lower line of the alignment paper.

Folding mirror 1 reflects the beam to folding mirror 2; its vertical alignment control can be used to adjust the height of the beam. Once more, for this the alignment tool is used and hung on the plate. Finally, the second beam splitter manipulator is used to adjust the pumping of the pre-amplifier path, until the reflected beam falls onto the upper line of the cell alignment paper. The 2nd amplifier stage was not used in this experiment, and hence we do not describe its alignment procedure. For further details on the procedure outlined above, see the instruction manual for the FL3000 dye laser.

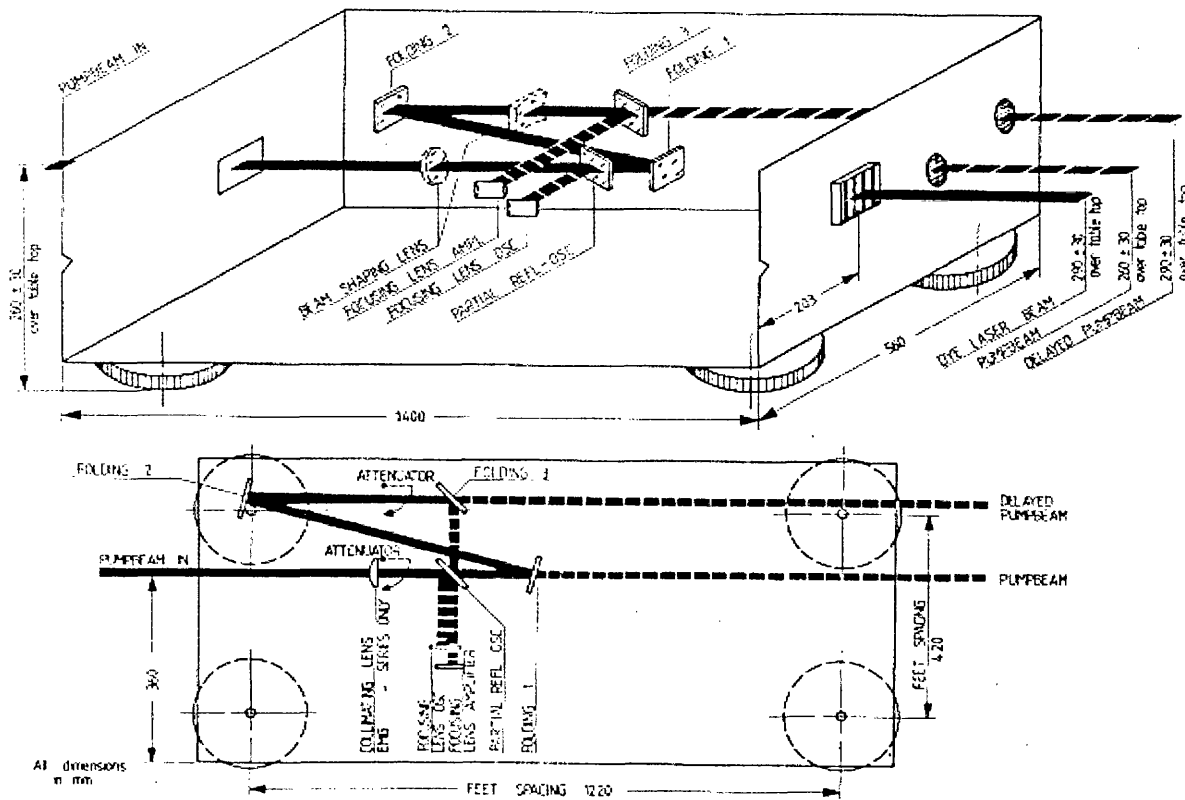


Figure 5.1: Alignment path of the FL 3000 dye laser (see instruction manual of the dye laser FL3000, Figure FL1).

5.2: Cleaning of the dye selector and leak testing

Because the dye laser had not been used for a long time, the dye selectors needed to be cleaned. Initially, the dye selectors were cleaned three times using water; each cycle involving 10 minutes of pump circulation. Methanol is used as a solvent to dissolve the laser dye (Rhodamine B). Thus, methanol is used in the final cleaning cycle, being circulated for about 15 minutes. No leaks appeared from the tubes or from the connection points.

5.3: Preparation of the dye solution

Rhodamine B (Rh B) is the laser dye used as active medium in this experiment. The solution data, such as the quantity of the dye and the type of solvent were taken from the table provided by Lambda Physik for pumping with 532nm (Nd:YAG laser, 2nd harmonic). According to the list 1 litre of the solvent (Methanol) takes 220mg of the dye (Rhodamine B) for the reservoir of the oscillator and preamplifier; this solution is mixed at room temperature. The dye Rh B is listed to have a tuning range of about 584-619nm, with peak emission at 594nm, as mentioned above in Table 2.1. The absorption and emission spectra for Rh B are shown in Figure 5.2.

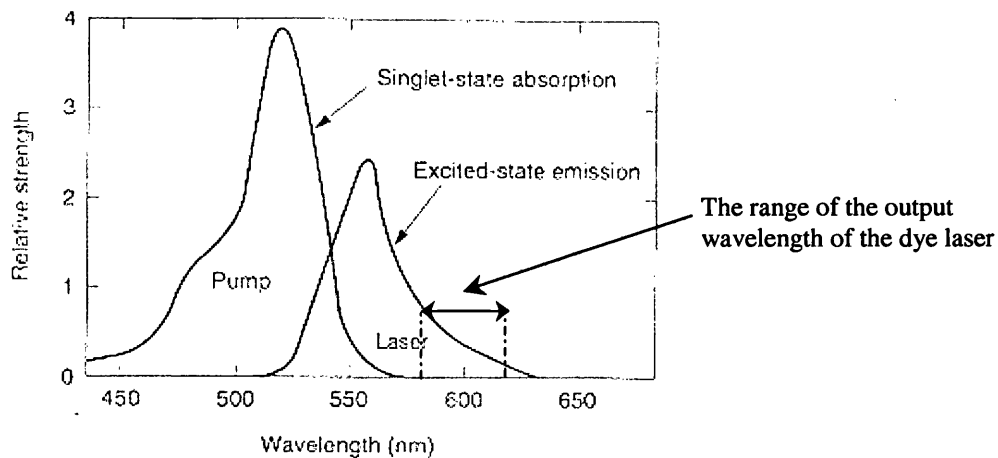


Figure 5.2: Absorption and emission spectra for Rhodamine B (Rh B laser dye), dissolved in Methanol. (Silfvast, 2004).

5.4: Rh B dye laser wavelengths

The wavelength of the dye laser was changed by using its computer-controlled grating selector. The dye laser output wavelengths are graphed by using a spectrometer; all spectra were taken with the 600gr/mm grating of the spectrometer.

The spectra for the individual wavelength setting are superimposed in Figure 5.3. Two things can be observed. First, the envelope of the intensity profile, as a function of the wavelength, does not change much with wavelength. This is due to the fact, that the spectrometer detector saturated (here we only wanted to determine the wavelength and not the pulse amplitude). Second, the tuning range is much narrower than expected, only 588-603nm. This is most likely due to the very low pump pulse energy available during the time of these tests.

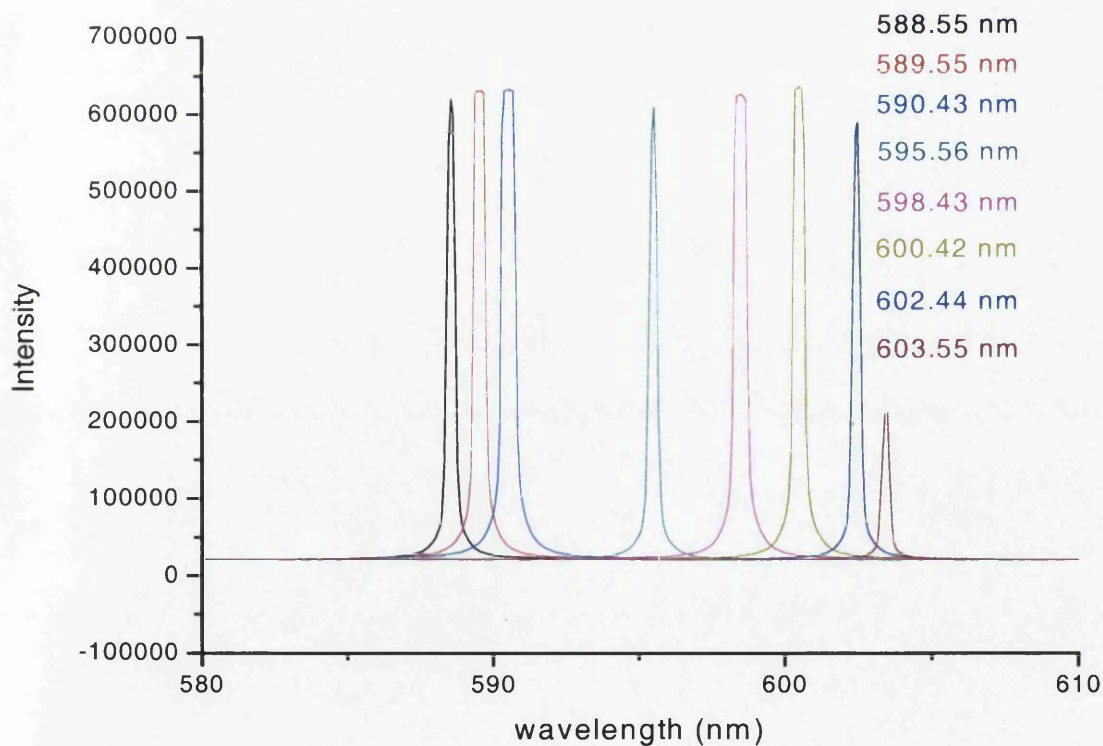


Figure 5.3: Dye laser wavelengths of the FL 3000, for Rh B, pumped by the 532nm green Nd: YAG laser.

5.5: Pulse Energy of the dye laser (E_p)

The pulse energy at the different wavelengths of the dye laser was measured using a joule meter. Some energy is lost in the beam steering prism, about 4.3% at each surface, i.e. a total of $\sim 8.6\%$, for perpendicular beam input, as detailed below.

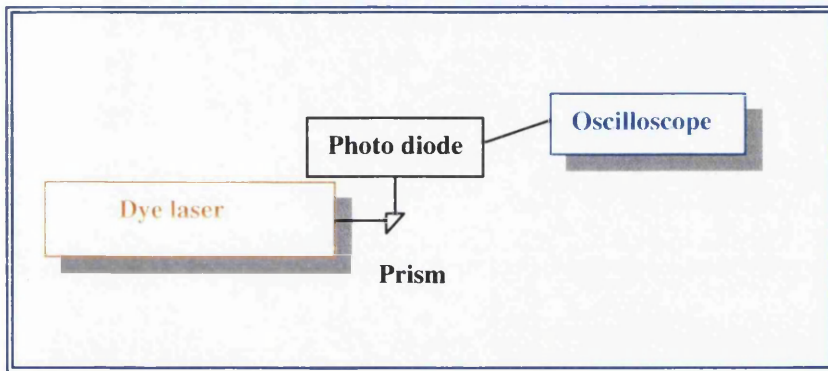


Figure 5.4: Set up of the dye laser pulse energy measurement.

The refraction losses of the a single surface can be calculated from

$$R = \left(\frac{n_2 - n_1}{n_2 + n_1} \right)^2 \quad (5-1)$$

The refractive index of the glass prism depends on wavelength. Using the value of

$n_{600} \cong 1.52$, one obtains:

$$R = \left(\frac{1.52 - 1}{1.52 + 1} \right)^2 = 0.043$$

$$R_{total} = 0.043 \times 2 = 0.086 \cong 8.6\%$$

Hence, the total energy of the dye laser is

$$E_{total} = E + 8.6\% E$$

A photodiode detector is used to measure the pulse energy of the dye laser, which can be calculated from the oscilloscope signal by using the formula (adopted from THORLABS)

$$V_0 = P \times \mathfrak{R}_\lambda \times R_{LOAD} \quad (5-2)$$

In our case, $R_{LOAD} = 50\Omega$; \mathfrak{R}_λ depends on the spectral responsivity curve, here

$\mathfrak{R}_\lambda = 0.34 \text{ A/W}$ @ 595nm, and P is the power density. For the peak power one finds

$$P = \frac{V_0}{\mathfrak{R}_\lambda \times R_{LOAD}}$$

With $P = \frac{E_p}{A \times \tau}$ substituted into equation (5-2) one finds:

$$E_p = \frac{V_0 \times A \times \tau}{50 \times \mathfrak{R}_\lambda}$$

The pulse energies of the dye laser are shown in Figure 5.5, as a function of wavelength.

Note that the pulse width of the dye laser was measured to be of the order $\sim 3\text{-}5\text{ns}$.

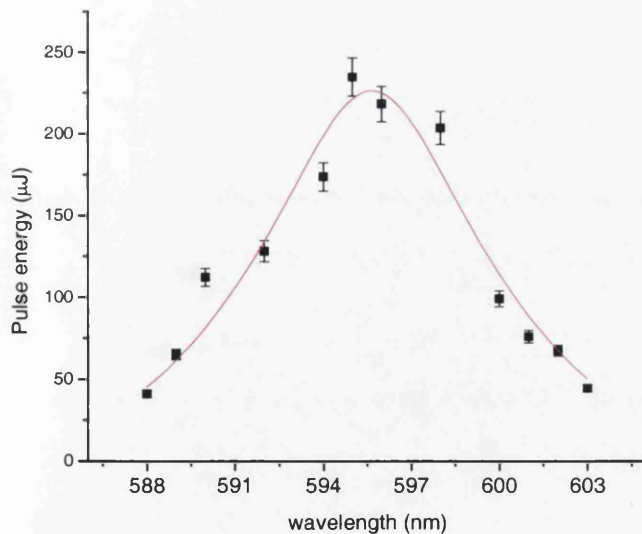


Figure 5.5: Dye laser pulse energy.

From the graph in Figure 5.5 the pulse peak power, at the center of the tuning curve, can be calculated as

$$P = \frac{E_p}{A\tau} = \frac{245 \times 10^{-6}}{(0.05)^2 \pi \times 5 \times 10^{-9}} \cong 6.2 \text{ MW/cm}^2$$

Chapter 6: Spectroscopic applications of the Nd: YAG and the dye lasers

In this chapter a brief description of the principles and theory for laser induced-breakdown spectroscopy (LIBS) is given together with experimental spectra of two samples, recorded for different observation delay and laser pulse energy.

The principles of optogalvanic spectroscopy are described later and some results were recorded using a tuneable dye laser.

Finally, the theory of laser induced fluorescence spectroscopy (LIFS) is summarized and attempts of its implementation are outlined.

6.1: Laser-induced breakdown spectroscopy (LIBS)

6.1.1: Principle and theory

Laser-induced breakdown spectroscopy (LIBS) is also known as laser-induced plasma spectroscopy (LIPS) [see e.g. Rohwetter et al, 2004]. It is an analytical spectroscopic method in which the output of a pulsed laser (for example from a Q-switched Nd: YAG laser) is focused onto the surface of the sample, which causes ablation and ionization of the sample atoms, forming a small plasma above the surface. The plasma light emission is collected and analyzed by the spectra detection system. LIBS was first invented by Brech and Cross in 1962 [see e.g. Adrain et al, 1984].

For a transition between two levels, the signal intensity is given by:

$$I = \frac{hcAn}{4\pi\lambda} \quad (6-1)$$

Where I is the intensity per unit solid angle, h is *Planck's* constant, λ is the wavelength of emission photon, c is the velocity of light, A is the Einstein coefficient for spontaneous emission, and n is the population density.

The population density is related to the total population of the species (N) by the Boltzmann equation when the energy levels concerned are in local thermal equilibrium (LTE):

$$n = N \frac{g}{z} \exp\left(-\frac{W}{kT_e}\right) \quad (6-2)$$

Where g is the statistical weight, W is the energy of the upper level, k is the constant of Boltzmann, and T_e is the electron temperature.

Equation (6-2) is substituted into (6-1) to obtain the intensity of the spectral line,

$$I = \frac{hcgAN}{4\pi\lambda z} \exp\left(-\frac{W}{KT_e}\right) \quad (6-3)$$

If taking natural logarithms for both sides of equation (6-3), one obtains

$$\ln\left(\frac{I\lambda}{gA}\right) = \ln\left(\frac{hcN}{4\pi\lambda}\right) + \left(-\frac{W}{KT_e}\right) \quad (6-4)$$

Note that the term $\left(-\frac{W}{KT_e}\right)$ is constant, therefore when plotting $\ln\left(\frac{I\lambda}{gA}\right)$ against W , a straight line of slope $\frac{-1}{kT_e}$ is the result (known as Boltzmann plot), as shown schematically in Figure 6.1.

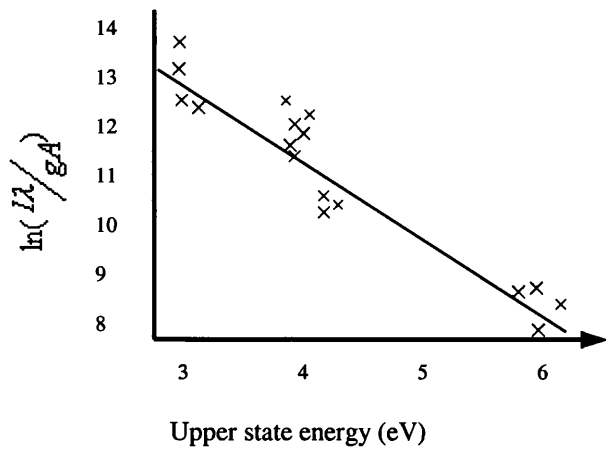


Figure 6.1: Boltzmann plot $\ln\left(\frac{\lambda I}{gA}\right)$ against W for an Fe I spectral line (adopted from Adrain and Waston et al, 1984).

Pulses from a Nd: YAG laser operating at 1064nm ablate a minute amount of mass of the material per one laser pulse. Examples for experiments with pulse width 8ns and pulse energy 13mJ are collected in Table 6.1 (see Uebbing et al, 1991).

Table 6.1: Ablated mass per laser pulse for different sample materials.

Sample	Ablated mass per laser pulse, in μg
Aluminum	0.170
Copper	0.084
Steel	0.030
Borax glass ($\text{Si}_2\text{B}_4\text{O}_7$)	0.003
Ceramics	0.004
Brass (Cu 65.5% / Zn 34.1%)	0.09

LIBS can be used to determine the composition of materials and alloys, and to a limited extent also for molecular analysis (identification), in medical investigations for the analysis of biological and pharmaceutical samples, and in archaeological investigations.

6.1.2: Apparatus for LIBS

The typical apparatus for laser-induced breakdown spectroscopy consists of the laser source, a spectrometer, focusing lens and transmission lens, optical fiber, collection optics, a target (sample) holder, and the samples (see Figure 6.2). Two samples were used in this study, namely aluminum and copper.

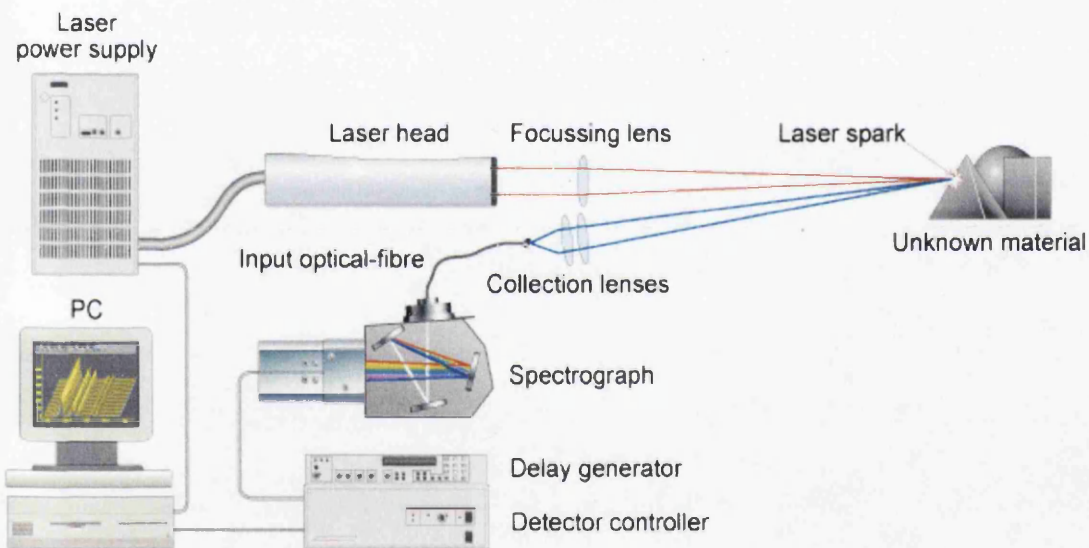


Figure 6.2: Typical LIBS system set up (from Applied Photonics Ltd brochure).

Radiation from our Q-switched Nd: YAG laser operating at 1064nm with repetition 20 Hz, 4ns pulse width and fixed energy (approximately 20mJ) is focused onto the sample

and used to ablate the surface of the sample to generate the plasma (see Figure 6.3a). The analysis system consists of a spectrometer, comprising a spectrograph that includes three gratings (2400, 600 and 150 grooves/mm), an array detector, a delay generator, detection controller and a PC computer controller (see Figure 6.3b).

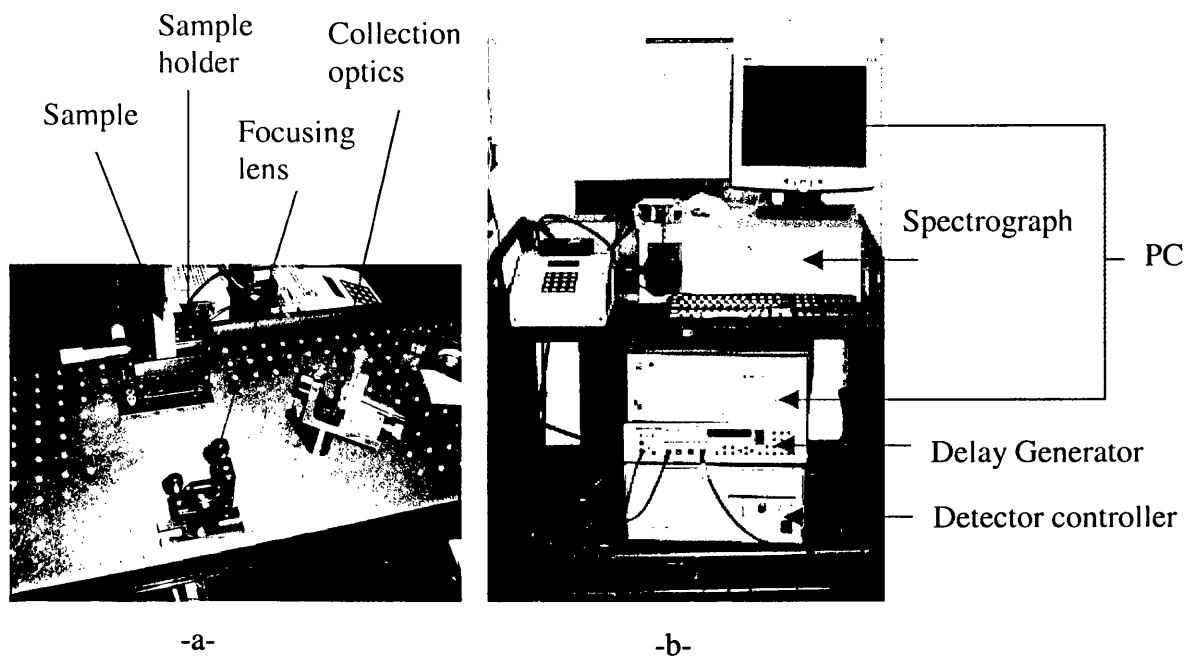


Figure 6-3: External view of (a) the LIBS site and (b) the spectrometer.

6.2: Experimental results

In this study two types of materials were used, namely Al and Cu. Typical spectra were recorded at fixed laser pulse energy of about 20mJ but for different grating resolution, and as a function of delay between excitation and observation, from 1 μ s to 30 μ s.

6.2.1. LIBS spectra of aluminum sample

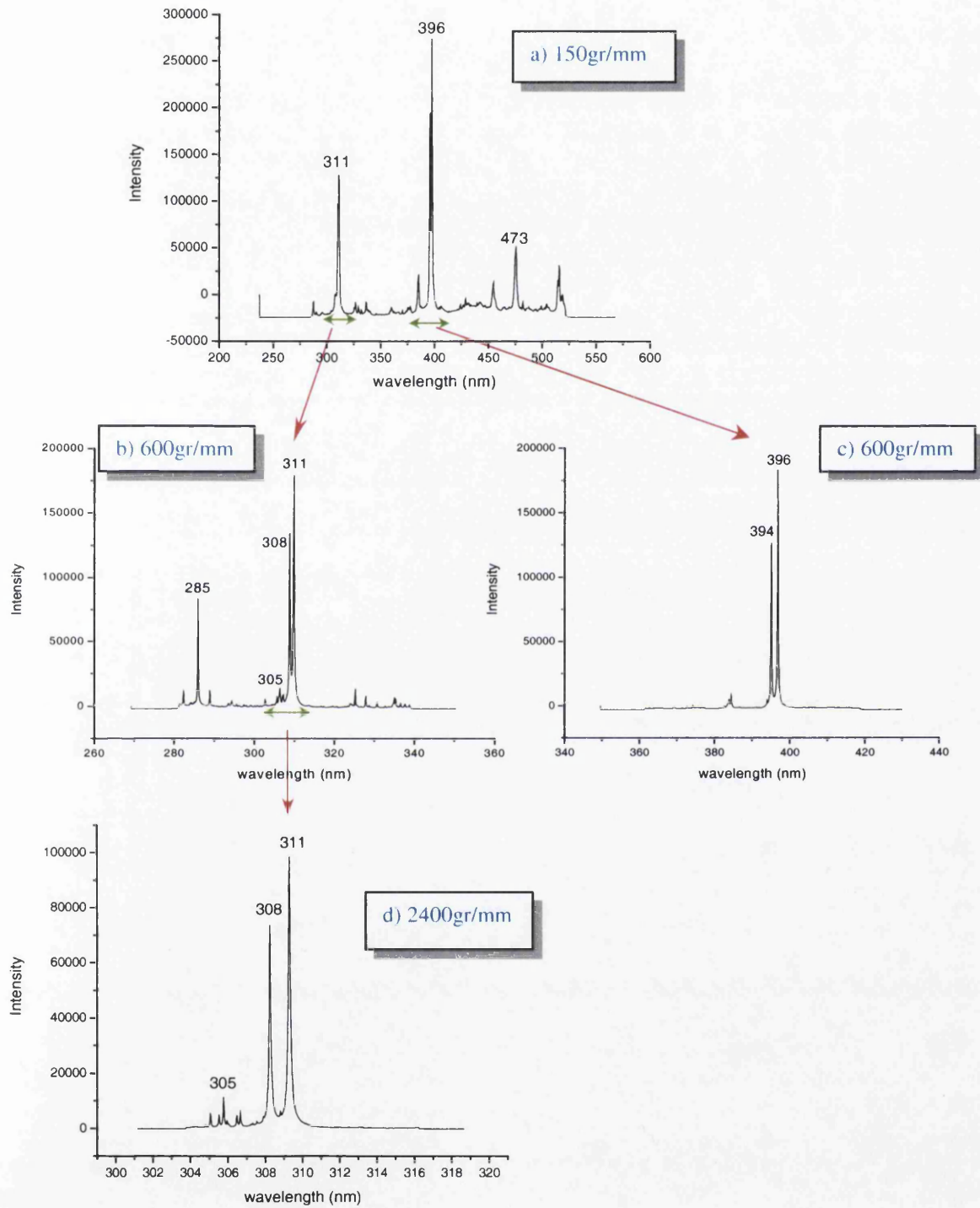


Figure 6.4: LIBS wavelengths are observed with different grating resolution.

The graphs in Figure 6.4 show the dominant Al lines at $\approx 310\text{nm}$ and $\approx 390\text{nm}$. For the grating with 150 groove/mm, the doublets are barely resolved. Graphs b and c were recorded with the grating 600 groove/mm, which provides better resolution, and now the wavelength resolution is sufficient to fully separate the doublets, i.e. into the 308 and 311nm and 394 and 396nm lines. For the 2400groove/mm grating the resolution now allows to observe additional details around the doublets. Note that this sample also exhibits lines at the wavelengths 285nm, 394nm, and 475nm which indicate impurities, most likely from the manufacture of Al from bauxite, and intentionally added trace elements to improve strength. Common impurity metals are Fe, Si, Na, Ca and Ti, as well as intentionally added Mg.

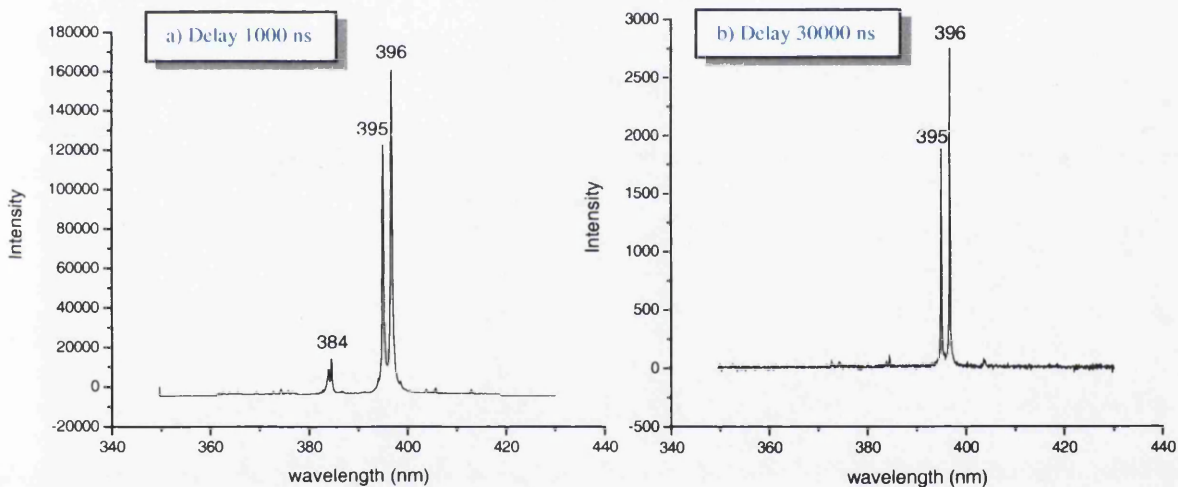


Figure 6.5: Aluminum spectra with different delay at 390nm, using the 600gr/mm grating.

Table 6.2: Wavelength intensity of aluminum regarding to the delay.

Delay (ns)	Intensity of 396.77nm	Intensity of 395.14nm	Intensity of 384.63nm
1000	161668	121588	13418
2000	102903	79442	12388
3000	68079	50828	9526
4000	52580	37278	7822
5000	36336	25996	4440
6000	28773	20793	3437
7000	27511	19536	2690
8000	21101	14698	2165
9000	18392	12922	1707
10000	17601	12029	1401
12000	14847	10251	1053
14000	13359	9057	540
18000	8553	5963	452
30000	2758	1820	84

Table 6.2 shows the intensity at the wavelengths when altering to the delay; clearly, increasing the delay causes a decline of the intensity (see Figure 6.9a). All these data were obtained with the grating 600gr/mm, and are visualised in Figure 6.9 further below.

Aluminum spectra were also recorded using the 600gr/mm grating, with different energy in the range of 20-60mJ (see Figure 6.6); the peak intensities are collected in Table 6.3, and later are visualised in Figure 6.9b.

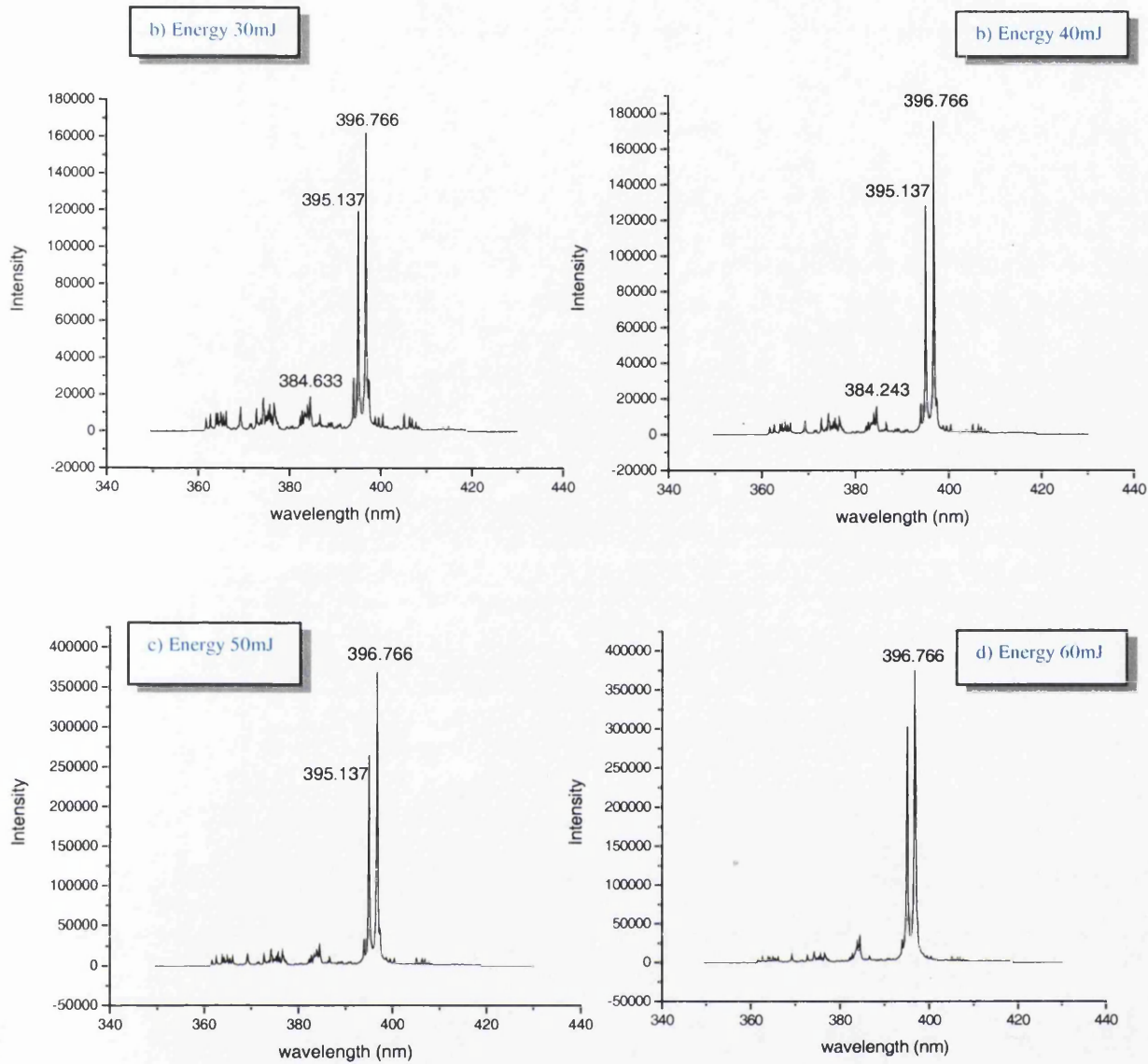


Figure 6.6: Aluminum spectra recorded at different laser ablation energy.

Table 6.3: Intensity of the wavelengths at 396.753nm, 395.113nm, and 384.496nm, respectively, for varying pulses energy.

Pulse energy (mJ)	Intensity of 396.753nm	Intensity of 395.113nm	Intensity of 384.495nm
20	161212	122100	13418
30	172180	119083	17916
40	196075	128266	15737
50	301996	266125	25853
60	354430	303038	32884

6.2.2. LIBS Spectra of Copper Samples

LIBS spectra for Cu were recorded for wavelengths at around 325nm, where the main emission doublet for copper is observed. As before, different delays between excitation and observation were implemented (see Figure 6.7). All measurements were carried out using the 600groove/mm grating.

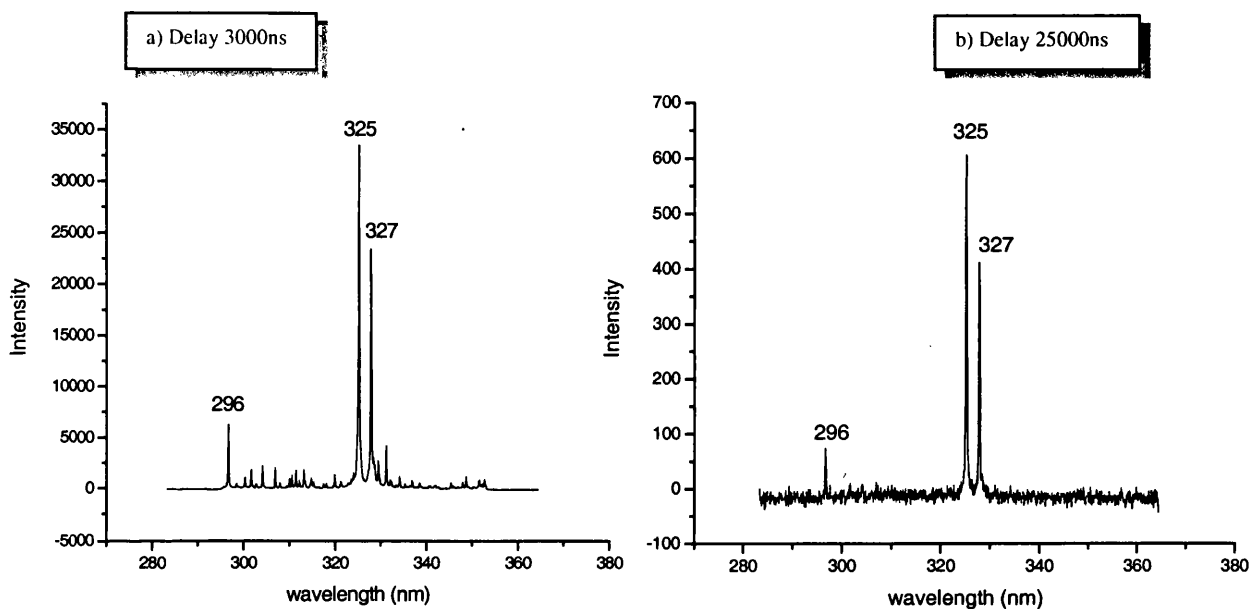


Figure 6.7: Copper spectra with different delay times between ablation and spectroscopic probing.

In Table 6.4 the intensities of the Cu spectral lines are summarised, which decrease with longer delay; as stated above, the spectra were recorded using the grating of 600gr/mm.

Table 6.4: Wavelength intensity of copper with varying delay.

Delay (ns)	Intensity of 325.187nm	Intensity of 327.797nm	Intensity of 296.702nm
1000	107167	76322	12160
3000	33507	23393	6251
4000	20900	13838	2267
5000	17146	11574	2493
6000	12897	8967	2276
7000	11298	8034	2391
8000	10941	7814	2378
9000	9240	6654	1818
10000	8359	5988	1636
12000	6787	4804	951
14000	4004	2903	736
16000	3531	2516	556
18000	2929	2149	536
20000	1554	1097	246
25000	608	412	73

As for Al, spectra for Cu were also recorded for changing of the pulse ablation energy of the fundamental beam at 1064nm from 20mJ up to 60mJ; as expected, the energy causes changes in the intensity of the spectrum (see Figure 6.8 and 6.6).

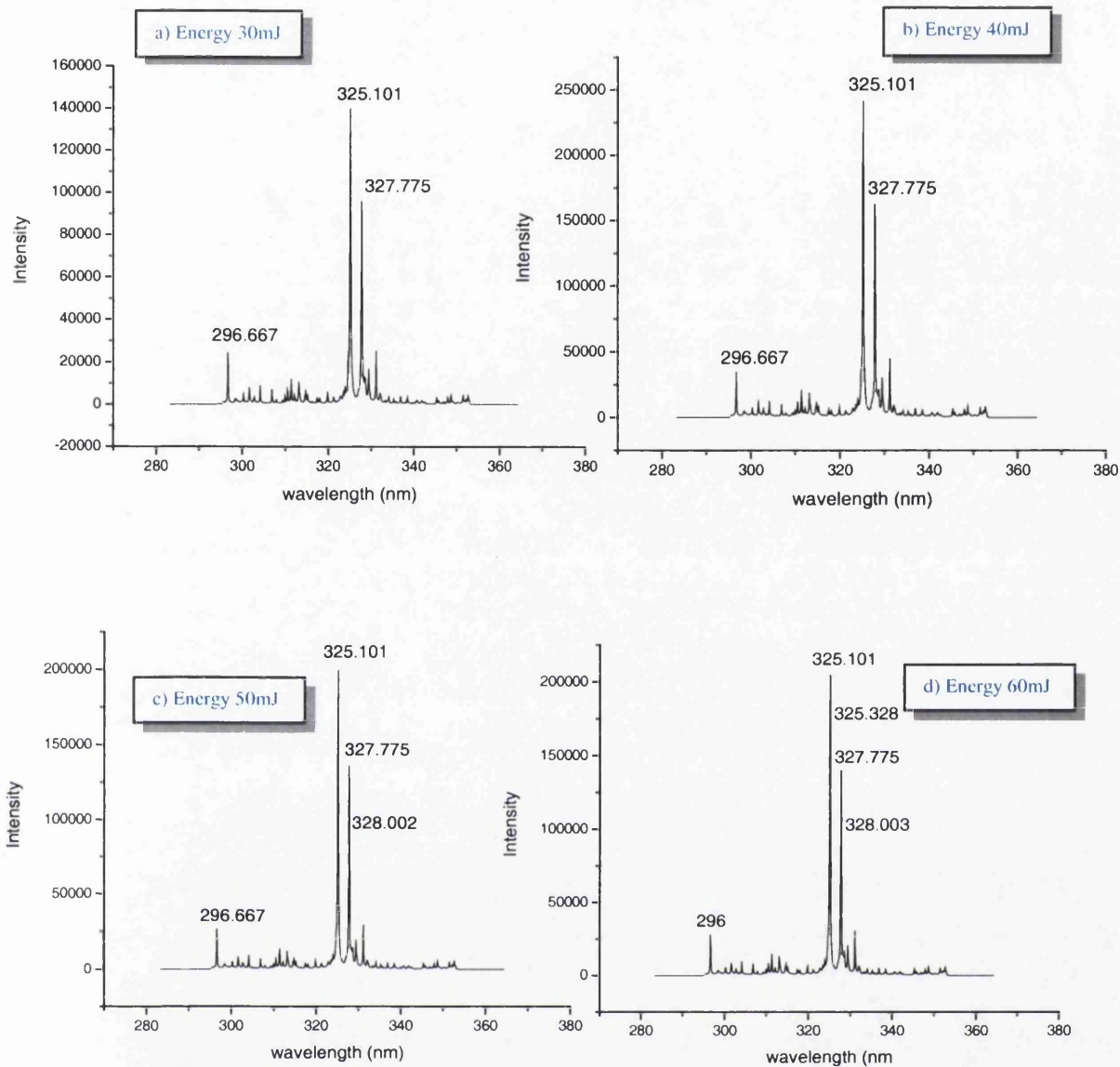


Figure 6.8: LIBS spectra of copper for different ablation energy.

Table 6.5: Intensity at the wavelengths at 325.187nm, 327.797nm, and 296.702nm against the pulse energy. The intensity increases with energy.

Pulse energy (mJ)	Intensity of 325.186nm	Intensity of 327.796nm	Intensity of 296.701nm
20	105772	76322	12519
30	140375	95747	24064
40	162292	162617	34863
50	208953	135119	26167
60	204647	140101	26807

A summary of the time dependence and pulse energy dependence for the emission lines

from Al and Cu is given in Figure 6.9.

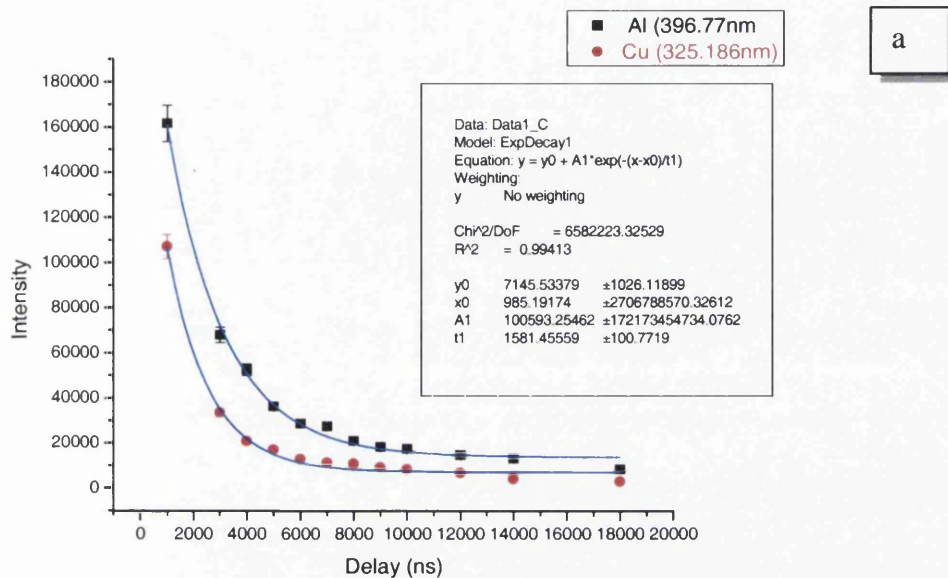


Figure 6.9: a) LIBS intensities of Al and Cu using fundamental beam of Nd: YAG laser at 1064nm versus delay.

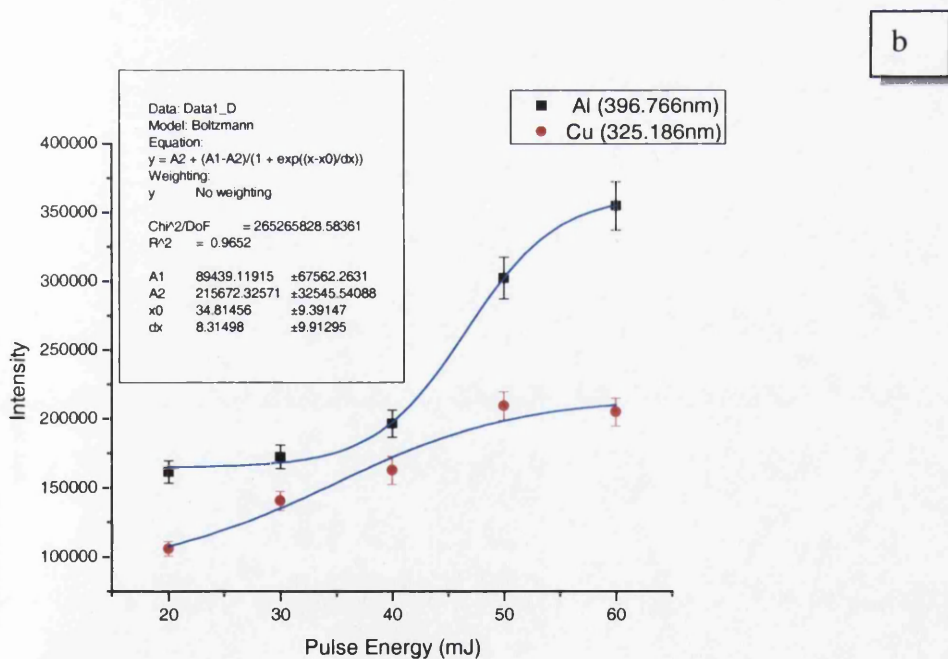


Figure 6.9 : b) LIBS spectral line intensities, as a function of the pulse energy of the Nd: YAG laser at 1064nm.

6.2.3 LIBS experiment using 532nm radiation

For comparison, the second harmonic output from the Nd: YAG laser at 532nm was used in a set of LIBS experiments with delay in the range of $1\mu\text{s}$ - $30\mu\text{s}$, for the same samples of aluminum (Al) and copper (Cu). Example spectra for the two samples, recorded for their most prominent emission lines, are shown in Figure 6.10. Table 6.6 summarizes the change in the intensity of the spectral lines, as a function of the delay.

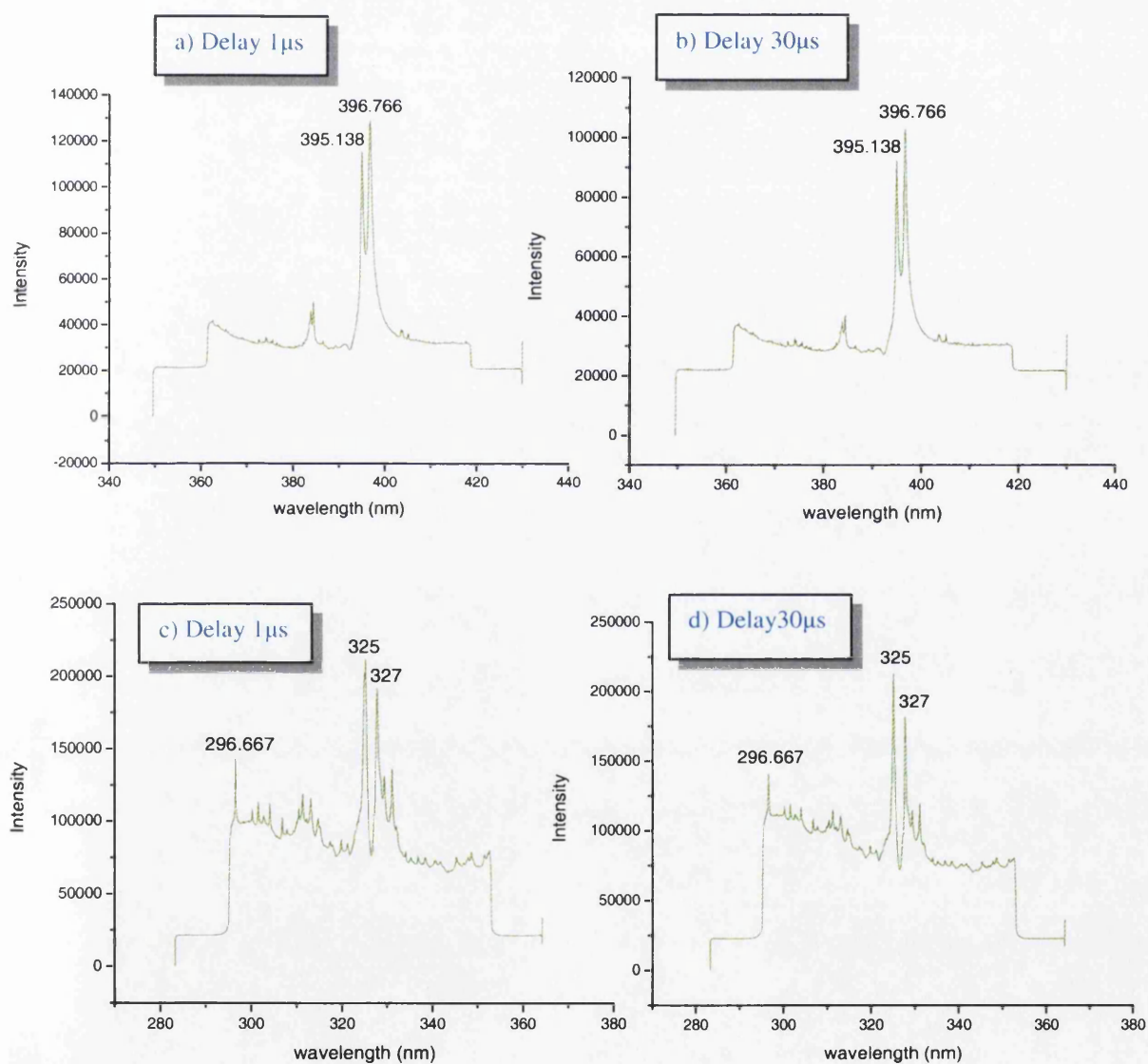


Figure 6.10: LIBS spectra of Aluminum (traces a and b) and Copper (traces c and d) for different delay. All spectra were recorded using the laser at 532nm.

Table 6.6: Intensity of Al and Cu against delay between ablation and observation.

Delay (ns)	Intensity of (Al) $\lambda=390\text{nm}$	Intensity of (Cu) $\lambda=325\text{nm}$
1000	114950	211720
2000	114950	195253
3000	114432	326487
4000	110173	295609
5000	110942	291225
6000	103857	282458
7000	100253	278074
8000	95465	278970
9000	93908	256426
10000	84890	254664
12000	79666	251522
14000	81929	248284
16000	77554	234777
18000	74406	227611
20000	75801	232472
25000	71258	230251
30000	70338	211016

The peak data summarized in the table are plotted in Figure 6.11 for better visualization.

As expected, the peak intensities decrease exponentially, as the plasma cools.

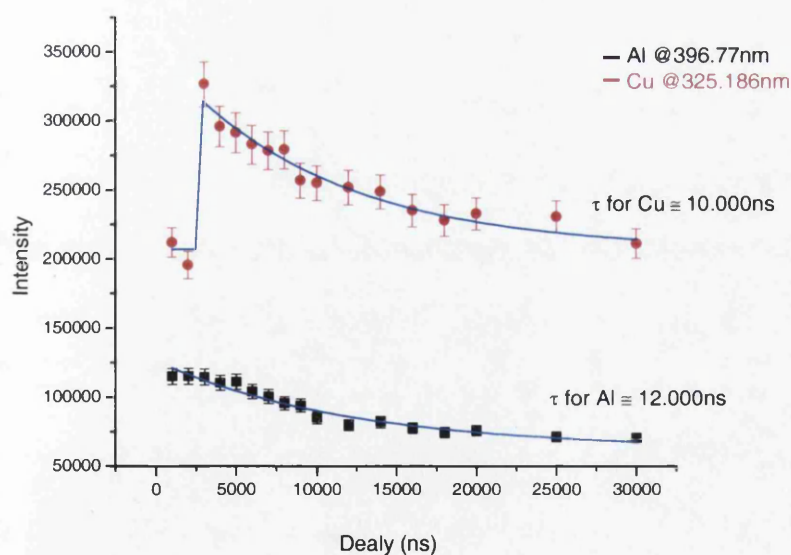


Figure 6.11: LIBS spectral line intensities, as a function of the delay for Al and Cu, using 532nm. Fitting with Exp Decay 1 of equation $y = y_0 + A1 \cdot \exp(-(x-x_0)/t1)$

6.3: Opto-galvanic Spectroscopy

6.3.1: Principles of opto-galvanic spectroscopy

Opto-galvanic spectroscopy is a well-established technique to conduct laser spectroscopy in gas discharges. When the atoms in the discharge tube absorb the energy of a laser photon to undergo the transition from $E_i \rightarrow E_k$, the interaction of radiation with the atoms (or ions) causes a change in the electrical properties of the discharge. This effect is known as the opto-galvanic effect (OGE); OGE was first discovered by Foote and Mohler (1925) and Penning (1928) in discharges at low pressure. Foote and Mohler investigated cesium vapour to detect ion formation, while Penning used two neon discharge tubes. Penning observed an impedance change in a low-pressure neon glow discharge on irradiation by light from the second Ne tube (for further details see e.g. Daran, 1989).

In general, the perturbed level distribution returns to steady state after illumination. A multiplication factor α is defined as "the number of electrons generated at the cathode by avalanche, caused by a single electron emitted from the cathode". In the steady state $\alpha = 1$; if $\alpha > 1$ the current increases. Let us consider an electron, which passes through the illuminated volume and the response is in the "small signal domain", i.e. when the signals are very small. Under these conditions $\alpha \equiv 1$ ($d\alpha = 0$).

$$d\alpha = \left(\frac{\partial \alpha}{\partial V} \right)_{ni} \Delta V + \sum_i \left(\frac{\partial \alpha}{\partial n_i} \right)_{V, n_j, j \neq i} \Delta n_i = 0, \quad (6-5)$$

Where V is the voltage across the tube, ΔV is the small signal voltage (the deviation from the steady state), n_i are the atomic populations, and Δn_i are their steady state deviations one obtains

$$\Delta V = -\beta \sum_i a_i \Delta n_i, \quad (6-6)$$

$$\text{Where } \beta = \left(\frac{\partial \alpha}{\partial V} \right)_{n_i}^{-1} \text{ and } a_i = \left(\frac{\partial \alpha}{\partial V} \right)_{n_i, V}. \quad (6-7)$$

β is always positive since a voltage increase will increase the ionization probability; furthermore, also $a_i > 0$ for all i . In general, a_i increases with energy of the state i .

The dynamic equation for Δn_i is given by

$$\frac{d(\Delta n_i)}{dt} = \sum_j \gamma_{ji} \Delta n_j - \sum_j (n_i - n_j) \sigma_{ij} I_{ij}, \quad (6-8)$$

Where γ_{ij} are the rate coefficients for transition $i \rightarrow j$ (without illumination), σ_{ij} is the optical cross-section for the transitions and I_{ij} is the light intensity. For a monochromatic laser pulse at the resonance frequency of transition $1 \rightarrow 2$, one finds

$$\frac{d(\Delta n_1)}{dt} = \sum_j \gamma_{j1} \Delta n_j - (n_1 - n_2) \sigma_{12} I_{12} \quad (6-9)$$

$$\frac{d(\Delta n_2)}{dt} = \sum_j \gamma_{j2} \Delta n_j - (n_2 - n_1) \sigma_{12} I_{12} \quad (6-10)$$

The sums in the equations (6-9), (6-10) represent the relaxation of Δn_i to steady state without illumination. Since there are many levels they can be treated collectively using a characteristic relaxation time back to steady state after illumination, T_i . Therefore,

$$\frac{d(\Delta n_1)}{dt} = \frac{\Delta n_1}{T_1} - (n_1 - n_2)\sigma_{12}I_{12} \quad (6-11)$$

$$\frac{d(\Delta n_2)}{dt} = \frac{\Delta n_2}{T_2} - (n_2 - n_1)\sigma_{12}I_{12} \quad (6-12)$$

One then can deduct the behaviour of the optogalvanic signal, ΔV , for various modes of illumination. In the case of a cw laser, one may assume the fluctuations have passed so

$d\Delta n/dt = 0$. Therefore, one obtains, for $t \rightarrow \infty$,

$$\Delta n_1 = -(n_1 - n_2)\sigma_{12}I_{12}T_1, \quad (6-13)$$

$$\Delta n_2 = (n_1 - n_2)\sigma_{12}I_{12}T_2, \quad (6-14)$$

The voltage fluctuation, ΔV can be written as

$$\Delta V = -\beta\sigma_{12}I_{12}(a_2T_2 - a_1T_1)(n_1 - n_2). \quad (6-15)$$

If state "1" is the lower energy level, then $a_2 > a_1$ and $n_1 > n_2$, which give the following solutions for ΔV :

1. ΔV is negative if $a_1T_1 > a_2T_2$. Thus, the signal will be negative, except for excitation from metastable levels. A positive signal may change sign with increased current, because enhanced collisions with electrons will reduce T_1 (the gas pressure will also have a similar effect).
2. The time profile of ΔV follows the intensity, I_{12} (for cw radiation the laser has to be chopped to permit fluctuations and therefore detection from a dc discharge).

3. The OG signal (ΔV) is proportional to $(n_1 - n_2)$ and $\sigma_{12}I_{12}$ in the small signal limit.

The treatment for pulsed lasers differs somewhat. If one assumes that the pulses are short compared to any other process, the rate equation becomes;

$$\frac{d(\Delta n_1)}{dt} = (n_1 - n_2)\sigma_{12}I_{12} = -\frac{d(\Delta n_2)}{dt}, \quad (6-16)$$

After the laser pulse ends (at $t = 0$);

$$\frac{d(\Delta n_1)}{dt} = -\frac{\Delta n_1}{T_1}, \quad \frac{d(\Delta n_2)}{dt} = \frac{\Delta n_2}{T_2} \quad (6-17)$$

$$-\Delta n_1(t=0) = \Delta n_2(t=0) = Q(n_1 - n_2), \quad (6-18)$$

Where;

$$Q = \sigma_{12} \int_{\text{pulse}} I_{12}(t) dt,$$

From these one obtains for ΔV ;

$$\Delta V = -\beta Q(n_1 - n_2) \left(a_2 e^{-t/T_2} - a_1 e^{-t/T_1} \right) \quad (6-19)$$

Where $a_2 > a_1$ and $n_1 > n_2$.

The OG signal voltage is always initially negative ($\Delta V(t=0) < 0$), for $T_1 \cong T_2$ the OG signal decays exponentially in a time characteristic of the plasma.

For metastable states ($T_1 \gg T_2$), the signal crosses zero at a time t_0 and decays with time constant t_1 . The maximum signal is given by $t = t_m$, t_0 and t_m are given by the formula;

$$a_2 e^{-t_0/T_2} = a_1 e^{-t_0/T_1} \quad \text{and} \quad \left(\frac{a_2}{T_2}\right) e^{-t_m/T_2} = \left(\frac{a_1}{T_1}\right) e^{-t_m/T_1}. \quad (6-20)$$

In both cases ΔV is directly proportional to $(n_1 - n_2)$ and $\sigma_{ij} \int_{\text{pulse}} I_{ij}(t) dt$ (see e.g.

Griffiths, 2005).

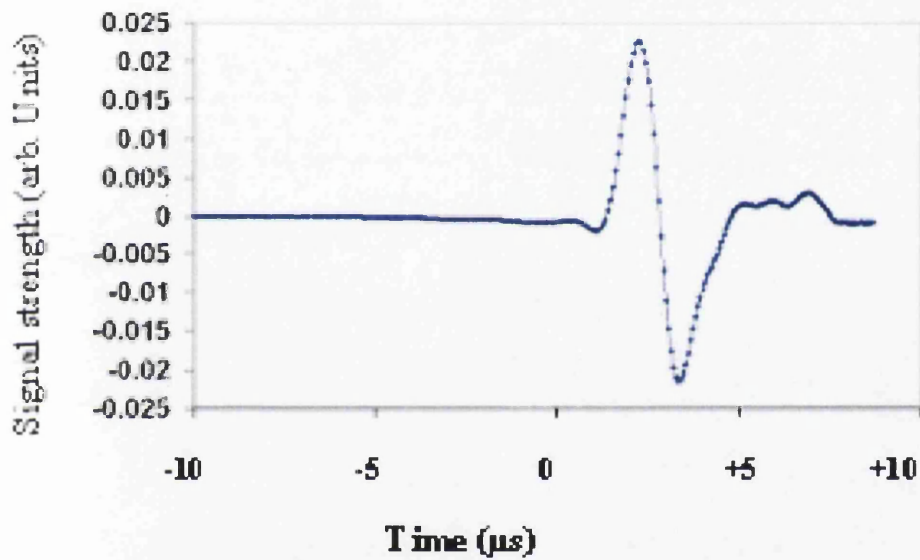


Figure 6.12: Typical OG signal, with the laser tuned to a Ne resonance.

6.3.2: Apparatus for opto-galvanic spectroscopy (OGS)

Principally, an opto-galvanic spectroscopy experiment consists of the laser, a hollow cathode lamp (discharge tube), an opto-galvanic controller, and a boxcar integrator (see Figure 6.13)

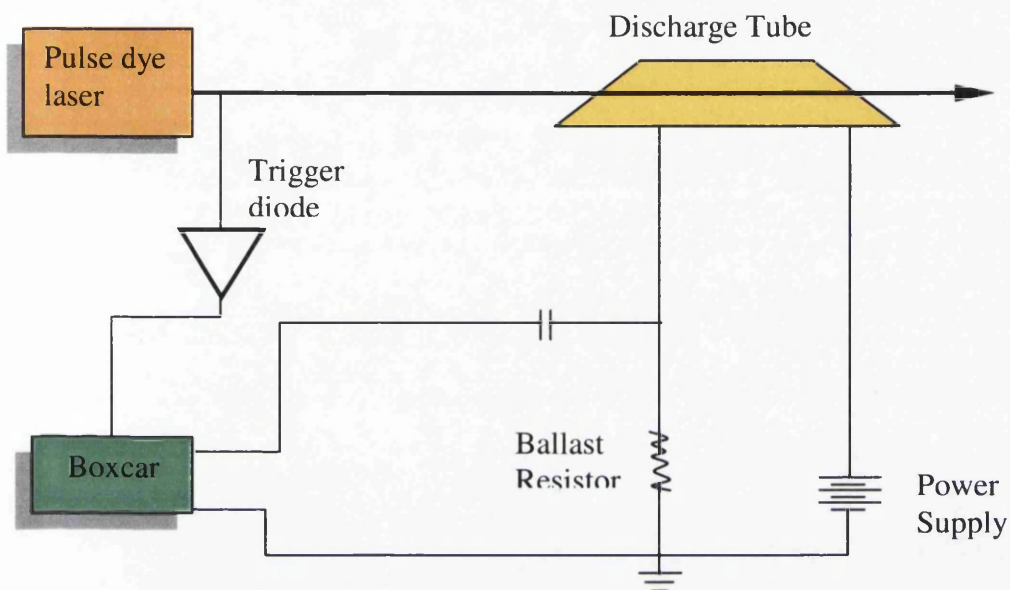


Figure 6.13: Typical experimental apparatus for opto-galvanic spectroscopy. The signal is detected across the ballast resistor while the capacitor permits decoupling of the high-voltage power supply.

In our case, a dye laser was used to irradiate the atoms or ions in the discharge tube, which initiate the change in the electrical properties of the discharge. Our basic set up for OGS is shown in Figure 6.14; the important components which are summarized below:

- (1) Quantel Brilliant (Q-switched) Nd: YAG laser was used to pump dye laser.
- (2) the dye laser (FL3000) was used to irradiate the atoms in the discharge tube.
- (3) collection optics were used to collect part the plasma emission.

- (4) a Spectrometer was used to record the spectral emission lines, including those at 588nm, 594nm, and 597nm.
- (5) an OG controller and a Boxcar integrator were used to analyse the discharge in the hollow cathode lamp and read the signal intensities, respectively.
- (6) a Laptop was used to save the signal pictures.

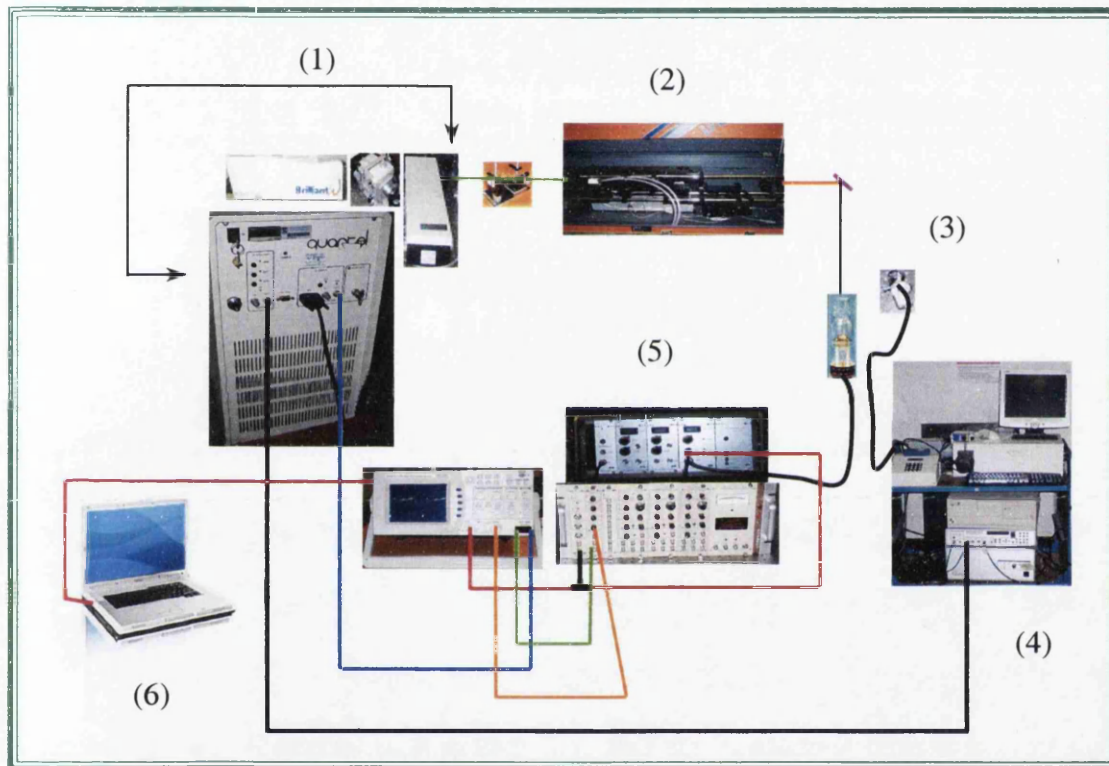


Figure 6.14: Experimental set up for Opt-galvanic system.

The output of the dye laser was focused by using a convex lens to illuminate the center of the hollow cathode lamp, and the OG controller sensed the signal while the dye laser was

scanned through the wavelengths at 588nm, 594nm, and 597nm associated with resonance transition in Ne. The OG signal is visualised using an oscilloscope, and the trace is saved onto a laptop; an example was shown in Figure 6.12 above.

(A). The hollow cathode lamp (HCL)

The hollow cathode lamp consists of a cathode, an anode with spacing of 2-3mm to the cathode, and an inert filler gas, at 10 to 15-mbar pressure (see Figure 6.15). In our study a Na-lamp is used, with maximum current of 15mA. The tube is a standard device manufactured by Cathodeon (Na lamp, with Ne gas filling; tube diameter 37mm).

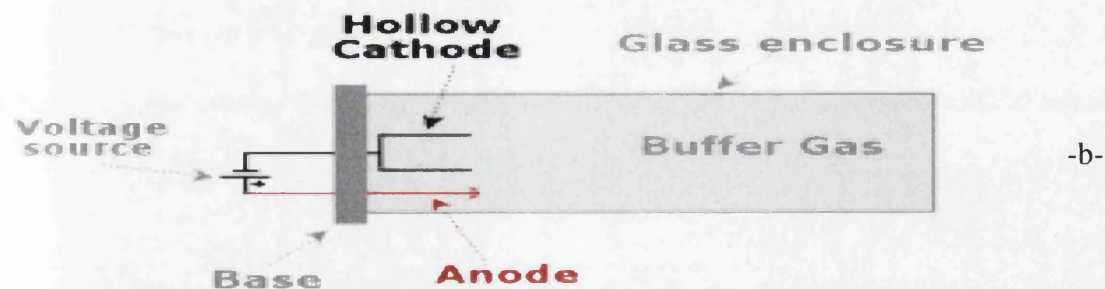


Figure 6.15: Typical Hollow cathode lamp, (a), and its schematic layout, (b).

(B). The boxcar integrator

The opto-galvanic circuitry consists of a trigger- photodiode, the lamp current controller and a signal gated-amplifier (for details see Senturk, 1996, and Griffiths, 2005). Note that the OG internal gated amplifier was not used because of mismatched delay parameters not suitable for our experiments. Instead, an external boxcar integrator (Stanford Research Systems SR250, and SR 275) is used in the experiment, in conjunction with the OG controller. The boxcar integrator is used to increase the signal-to- noise ratio of the signal. Also, because it can read any point of the signal by varying the delay between the start of the trigger pulse to the sampling, the signal shape can be recorded.



-a-



-b-

Figure 6.16: a- Opto-galvanic controller, b- Stanford Research Systems boxcar integrator.

6.3.3: OGS measurements using the LP 3002 dye laser

The dye laser used in our study of OGS could be tuned in the range 588nm-603nm (dye Rh B). During the experiment, the hollow cathode lamp was set to 3mA; an oscilloscope was used to visualise the OG signal. Three strong signals of OG-resonances were found when the wavelength of the dye laser was scanned in the range 588-603nm. As stated above, a Na / Ne hollow cathode lamp was used in this study. The emission spectrum of this lamp is shown in Figure 6.17.

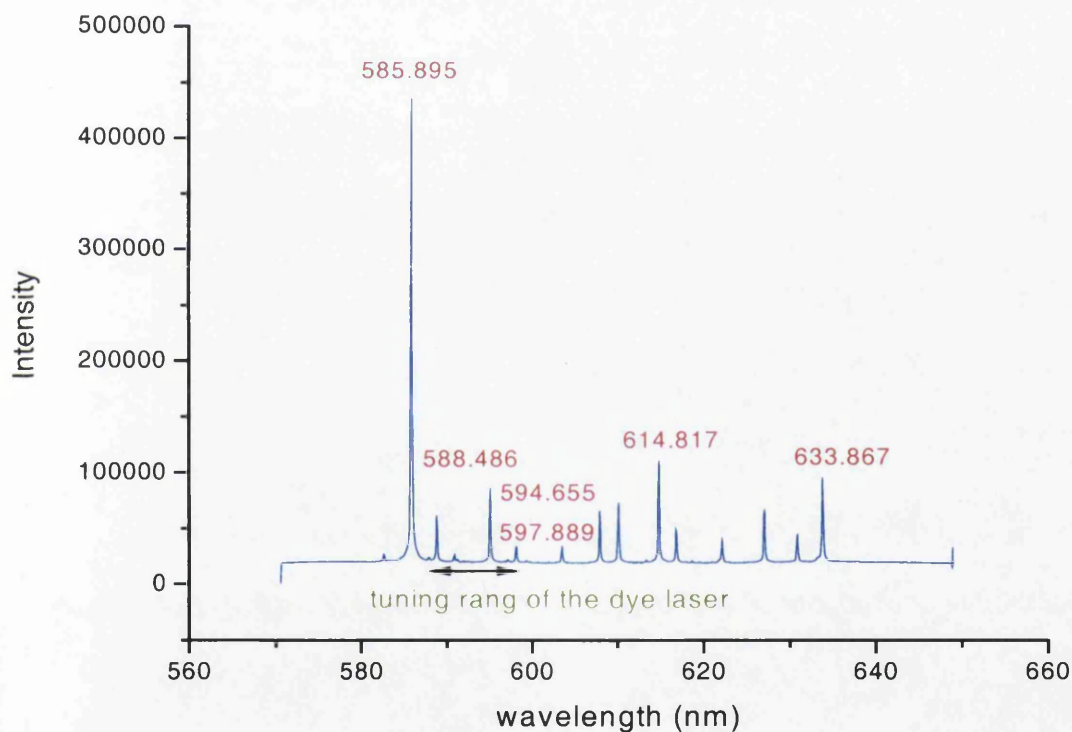
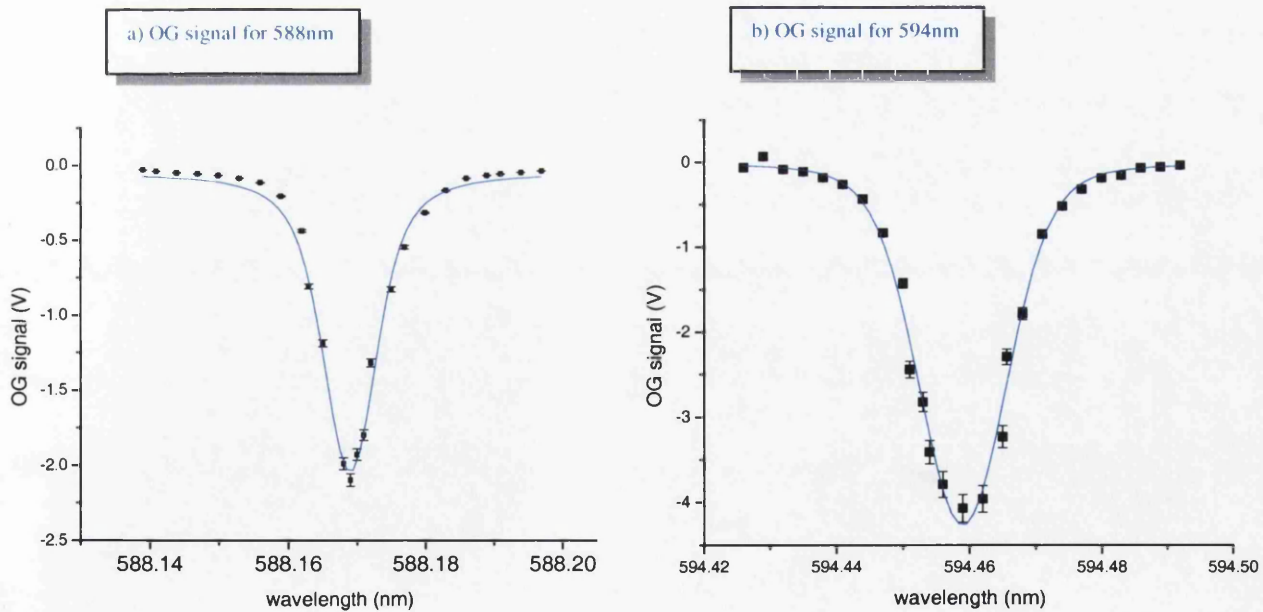


Figure 6.17: Emission spectrum of Na / Ne hollow cathode lamp. Note that the dominant lines are those of Ne, from the transition configuration $2p^5 3s \leftrightarrow 2p^5 3p$. The OG transitions associated with the wavelengths 588nm, 594nm, and 597nm were observed in the tuning of the dye Rh B.

Table 6.7: Comparison for selected wavelengths: $\Delta\lambda = (\lambda_{tab.} - \lambda_{obs.})$, observed wavelength and tabulated wavelength for Ne emission lines.

Tabulated λ (nm)	Observed λ (nm)	$\Delta\lambda = (\lambda_{obs.} - \lambda_{tab.})$ (nm)	OG λ (nm)	$\Delta\lambda = (\lambda_{OG} - \lambda_{tab.})$ (nm)
585.248	585.895	+0.647	-	-
588.189	588.486	+0.297	588.169	-0.020
594.483	594.655	+0.172	594.459	-0.024
597.533	597.889	+0.356	597.53	-0.003
614.305	614.817	+0.512	-	-
633.442	633.867	+0.425	-	-
Average $\Delta\lambda = 0.402$			Average $\Delta\lambda = -0.016$	

While the spectrometer readings were incorrect by ≈ 0.4 nm, the dye laser readings look to be reasonably correct, meaning that its drive mechanism is well calibrated.



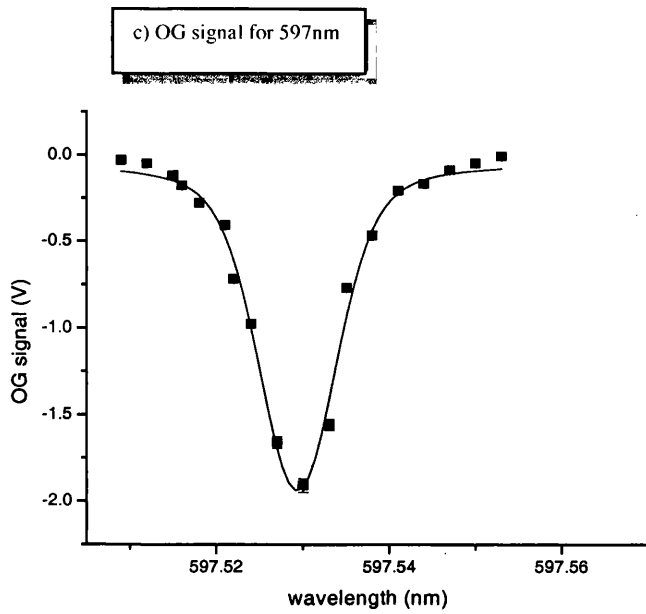


Figure 6.18: OG signals for the wavelengths scanned by the dye laser; (a) to (c) represent the resonant transitions at 588nm, 594nm, and 597nm, which caused change in the electrical prosperities of the discharge lamp.

The measured line profiles for the dye laser OG scans were fitted to a Voigt profile as a compromise (pure Gaussian and Lorentzian shapes were inadequate):

$$y = y_0 + A \cdot \frac{2 \ln 2}{\pi^{3/2}} \frac{w_l}{w_G^2} \cdot \int_{-\infty}^{\infty} \frac{e^{-t^2}}{\left(\sqrt{\ln 2 \frac{w_l}{w_G}} \right)^2 + \left(\sqrt{4 \ln 2 \frac{x - x_c - t}{w_G}} \right)^2} dt .$$

The line positions derived from the fit are included in Table 6.7 above, indicating the quality of the laser OG calibration.

A line extends over a range of frequencies, and the spread is influenced by a number of processes. In addition its center may be shifted from its normal central wavelength by some of the broadening effects. In the OG discharge, the main processes are:

1. **Natural broadening:** the uncertainty principle relates the lifetime of an excited state to the energy width of a level. The broadened line shape is described by a Lorentzian profile.
2. **(Thermal) Doppler broadening:** The atoms in a gas, which are emitting radiation, will have a distribution of velocities; this in turn affects the emission wavelengths. The broadened line shape is described by a Gaussian profile.
3. **Pressure (collisional) broadening:** When an atom with energy levels E_i and E_k approaches to another atom, the energy levels will be shifted because the interaction between the atoms. The shift in the energy depends on the configuration of the electrons of the atoms and the distance between them. The shift in different energy levels may be positive if the interaction between the atoms is repulsive, or negative if the interaction between the atoms is attractive. For more details see e.g. Demtröder, (2003).

From the traces in Figure 6.18 the line widths were derived. Their values are summarised in Table 6.8, and are compared to the laser line width, which should dominate the line width, in principle, because the Doppler width of the transitions is estimated to be

$$\Delta\nu_D = 7.16 \times 10^{-7} \times \nu_0 \sqrt{\frac{T}{M}}$$



$$= 7.16 \times 10^{-7} \times 5.12 \times 10^{14} \sqrt{\frac{1000}{20.179}}$$

$$= 2.6 \times 10^9 \text{ Hz}$$

This value can be converted @600nm to Doppler width in wavelength one finds

$$\Delta\lambda_D = \frac{c}{\nu^2} \Delta\nu_D$$

$$= \frac{3 \times 10^8}{(5.12 \times 10^{14})^2} \times 2.6 \times 10^9$$

$$\Delta\lambda_D = 2.9 \times 10^{-3} \text{ nm}$$

Table 6.8: Comparison between observed and expected line widths.

Line (nm)	FWHM (nm)
Ne transition 588.169	0.010
Ne transition 594.459	0.016
Ne transition 597.53	0.011
Laser line	0.007
Doppler width $\Delta\lambda_D$	2.9×10^{-3} = 0.003

From Table 6.8 one finds: $\Delta\lambda_{laser} > \Delta\lambda_D$, and hence the laser line width should dominate.

6.4: Laser-induced fluorescence spectroscopy (LIFS)

It was intended to use laser-induced fluorescence spectroscopy as a complementary analysis method to LIBS; basically, the plasma was to be produced by ablation using our Q-switched Nd: YAG laser, and subsequently be probed by tuneable laser radiation (from our LP 3000 dye laser). (see Figure 6.19)

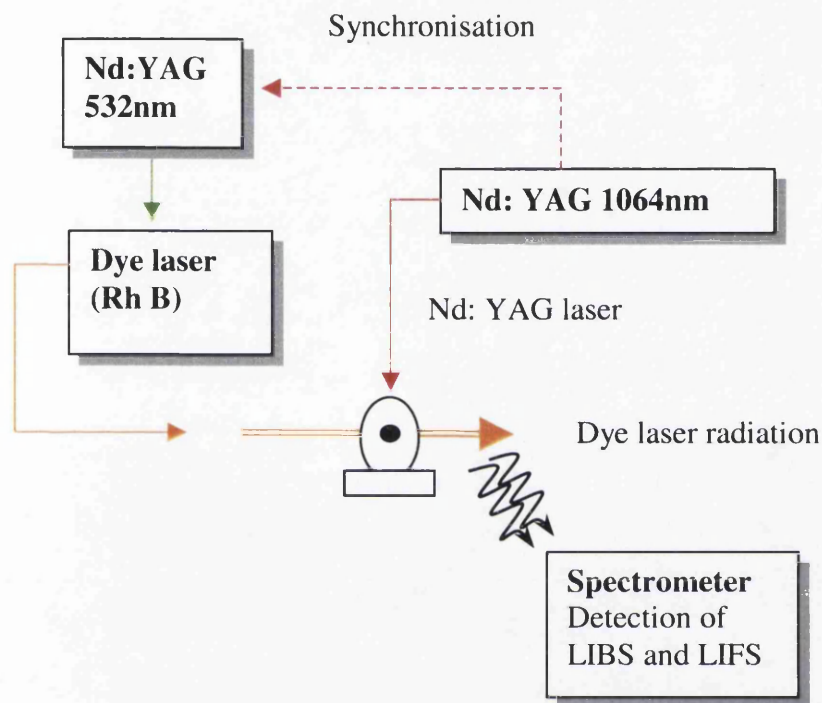


Figure 6.19: Simplified schematic for LIFS experiment.

6.4.1: Principles of laser -induced fluorescence spectroscopy (LIFS)

When an absorption transition occurs between $E_i \rightarrow E_k$, fluorescence photons are emitted in the decay from level E_k , not only back to E_i but also to other levels, E_m . This is exemplified in Figure 6.20.

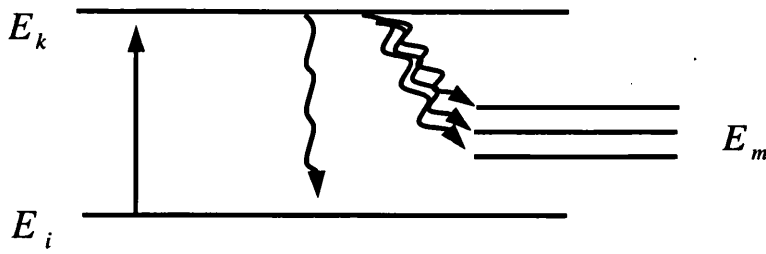


Figure 6.20: Fluorescence principle.

Assume that the number of photons absorbed per second along path length Δx is given by

$$n_a = N_i n_l \sigma_{ik} \Delta x,$$

Where n_l is the number of incident laser photons per second, σ_{ik} is the absorption cross-section per atom/molecule, and N_i is the density of the atom/molecules in the absorbing state (i). The number of fluorescence photons emitted per second from excited state level E_k then is

$$n_{FL} = N_k A_k = n_a \eta_k,$$

Where $A_k = \sum_m A_{km}$ is the probability of the total spontaneous transition to all levels with

$E_m < E_k$, and η_k is the photon quantum efficiency for radiative decay from the excited state which is given by

$$\eta_k = \frac{A_k}{A_k + R_k}.$$

The latter is the ratio of the spontaneous transition rate to the total deactivation rate, with R_k being the radiationless transition rate.

Note, that the number of fluorescence photons emitted per second (n_{FL}) is equal to the number of photons absorbed per second if the quantum efficiency of excited state (η_k) = 1, however this is rarely the case, since radiationless transitions always occur (see e.g. Demtröder, 2003).

6.4.2: Probing the OG plasma by utilising laser-induced fluorescence

Unfortunately, we did not have two independent Nd: YAG lasers available to realise the experiment shown in 6.20. Therefore, we attempted a LIF experiment within the OG discharge environment.

Laser-induced fluorescence spectra should appear in the overview emission spectrum of Figure 6.17 at the wavelengths 602.999nm, 616.359nm, and 659.433nm subsequent to excitation at 588.189, according to the level diagram given in Figure 6.21.

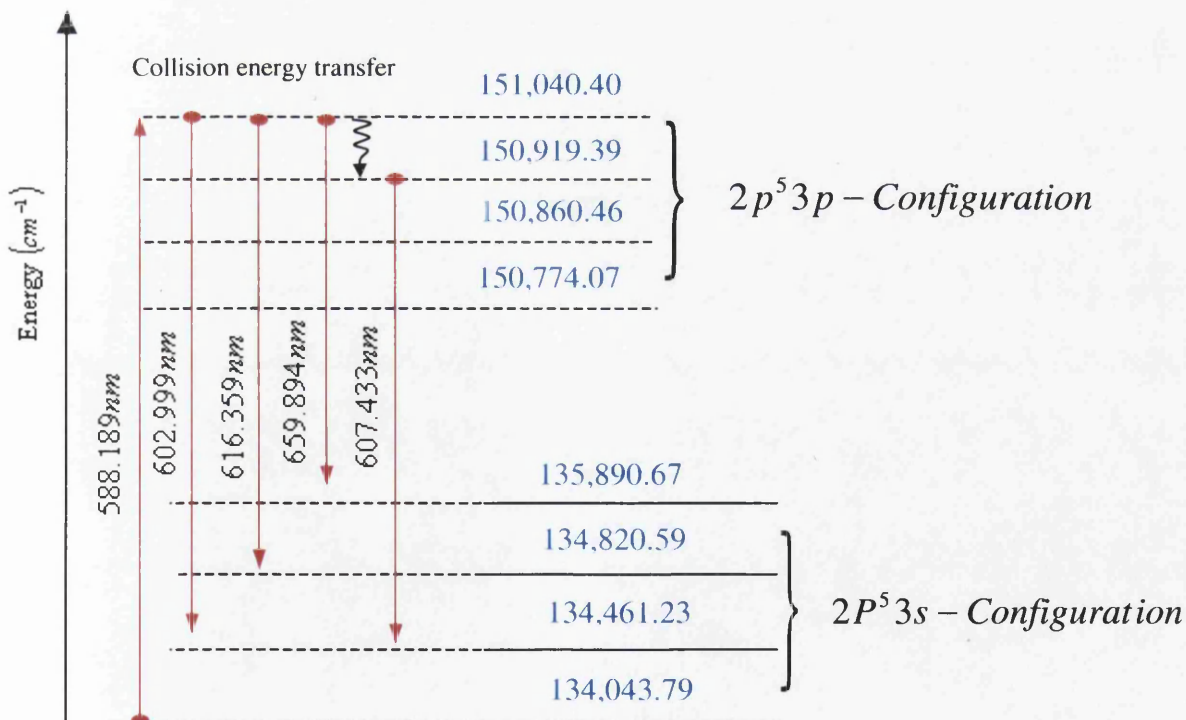


Figure 6.21: Ne energy level term diagram and allowed transitions (The data of this figure were adapted from Larkins, 2001).

During the time scale of these test experiments no LIF signal was observed. The most likely causes for this were that, the overall alignment of the laser, OG-lamp and the observation fibre were not perfect. However, with careful spatial alignment and proper spectrometer timing, LIF should easily be observable (see e.g. Utomo1994). A future task will be to rectify the alignment deficiencies to implement LIF in the OG-discharge.

Chapter 7: Conclusion

7.1: Summary of results

The Quantel Brilliant (Q-switched) Nd:YAG laser generated pulses at 1064 nm and with non-linear conversion techniques produced visible green laser light at 532 nm, and UV laser light at 355 nm, with energies at 102 mJ, 63 mJ and 26 mJ respectively, at 20 Hz repetition rate. The expected output energies at 20 Hz repetition rate were 350mJ at 1064nm, 160 mJ for the 2nd harmonic at 532 nm, and 60 mJ for the 3rd harmonic at 355nm, according to the manual of the laser.

Table 7.1: Comparison of the specified and measured pulse output from the Nd:YAG laser system.

	Specified in the manual (mJ)	Conversion efficiency (%)	Measured value (mJ)	Observed conversion efficiency (%)
Fundamental 1064nm	350		102	
2 nd harmonic 532nm	160	46	63	62
3 rd harmonic 355nm	60	17	26	25

The table reveals, that overall the output pulse energies are way down on specification. Most likely this is due to the fact that (i) the flashlamps of the Nd:YAG laser are old and (ii) its output coupler was not any longer exhibiting the full Gaussian reflectivity distribution. However, the conversion efficiencies into the harmonics from the fundamental wave are better with our set-up than for the Quantel add-on units which provide the 2nd / 3rd harmonic values listed in the manual. This is most likely due to the

fact that more efficient conversion crystals and beam separation optics were used in our arrangement built from Quanta Ray components.

The beam diameter and intensity profiles were determined using burn paper. The results show that, as expected, the beam diameter is $\cong 6\text{mm}$. They also reveal from the inhomogeneous profiles of the harmonic waves that the conversion crystals exhibit some damage.

The output pulse energy of the dye laser was measured as $\sim 250\mu\text{J}$ with a tuning range of 588-603nm; Rhodamine B was used as laser dye solution. The expected output pulse energy of the dye laser with using Rhodamine B was $\sim 20\text{mJ}$ with tuning range of 584-619nm, as described in the Lambda Physik brochure. The reasons for this are (i) the very low pulse energy which could be directed into the dye laser (our beam steering mirrors are far from ideal), and (ii) we only used the oscillator/pre-amplifier part of the laser (the amplifier cell was not used because this cuvette was damaged during the replacement of the dye laser tubing).

LIBS spectral lines of two samples were recorded, using the fundamental beam output from the Nd:YAG laser at 1064nm for ablation, with $\sim 20\text{mJ}$ pulse energy. Aluminum and copper were used as samples in our studies; the LIBS spectra were recorded, as a function of the observation delay in the range $1\mu\text{s} - 30\mu\text{s}$, and as a function of the pulse energy in the range 20 mJ to 60mJ. LIBS experiments were also implemented using 532nm radiation, for the same samples (Al and Cu) and for the same observation delay in the range $1\mu\text{s} - 30\mu\text{s}$.

Both sets of data reveal the expected exponential reduction in line intensity with increasing observation delay. Specifically, the high-resolution spectra reveal emission

lines from trace elements in the Al- and Cu- samples, demonstrating the potential capabilities of the LIBS technique for compositional analysis.

Opto-galvanic spectroscopy was implemented in a Na / Ne hollow cathode lamp. In our experiments the lamp was operated at 3mA, and OG signals were found at the wavelengths 588.169nm, 594.459nm, and 597.53nm. These data were used to compare the calibration of our spectrometer and the dye laser. While the laser was well calibrated, the spectrometer readings were off by $\cong 0.4\text{nm}$.

7.2: Future work

In order to complete the set up of a useful Nd:YAG plus dye laser system from old parts, a few tasks remain which were beyond the time scale of this project. While costs for replacement or refurbishment of component were an important and sometimes prohibitive factor, the lengthy return times from the manufacturer were more of a problem. Overall, the remaining tasks are as follows.

For the laser systems:

1. Replace the flashlamp and the output mirror of the Nd:YAG to improve the energy quality of its output at 1064nm. Also, check or change the ionized water, which is used to cool the laser head.
2. Take off the crystals of the harmonic generator to clean and re-polish them, or replace them by new ones to achieve improved conversion and better beam quality of the 2nd harmonic wave at 532nm and 3rd harmonic wave at 355nm.

3. The beam steering optics should be checked and optimized for the appropriate wavelengths and deflection angle.
4. Repair the amplifier cuvette of the dye laser by changing its cover block, or sending it to the company for repair, to achieve full power output.

For the spectroscopy experiments:

5. Properly set-up the OG-lamp excitation/observation for the implementation of LIFS.
6. Use second Nd: YAG laser to implement full LIBS + LIFS experiment of an ablation plasma.

References

Adrain, R.S. and Watson, J., (1984). *Laser Microspectral Analysis: a Review of Principles and Applications*, Journal of Physics D: Applied Physics Vol. 17, No. (10): 1915-1940

Bachor, Hans-A., (1998) *A Guide to Experiments in Quantum Optics*, Wiley-VCH

Barbieri, B. and Beverini, N., (1990) *Optogalvanic Spectroscopy*, Rev. Mod. Phys., Vol. 62, No. 3, 603-644

Ben-Amir, A., Erez, G. and Shuker, R., (July 1983) *Pulsed Resonant Optogalvanic Effect in Neon Discharge*, Journal of Applied Physics, Vol. 54, No. 7, 3688-3698

Daily, J. W., (March 1977) *Saturation effects in laser induced fluorescence spectroscopy*, Applied Physics. Vol 16, No. (3), :568-571

Daran, A. B. M. (1989) *Laser Spectroscopy of Molecules in Discharges*, PhD. Thesis. University of Wales Swansea

Demtröder, W., (2003) *Laser Spectroscopy: Basic Concepts and Instrumentation*, 3rd ed. Berlin: Springer-Verlag

Gallbacs, G., Budavari, V., Geretovszky, Z., (2005) *Multi-Pulse Laser-induced Plasma Spectroscopy using a single Laser Source and a Compact Spectrometer*, Journal Analytical Atomic Spectrometry, Vol. 20, 974-980

Griffiths, B., (2005) *Development of a high-Powered Tunable Laser System for Spectroscopic Studies of Trace Element and Positronium*, PhD Thesis, University of Wales Swansea

Guenther, R., (1990) *Modern Optics*, John Wiley & Sons, Inc.

Harper, P. G. and Wherrett, B.S., (1977) *Non-linear Optics*, Academic Press, New York

Hussein, H., (2004) *Frequency Selection and Stabilization of Semiconductor Laser Diode Systems*, PhD Thesis, University of Wales Swansea

Kucukkara, I., (1997) *Analytical Laser Spectroscopy using the Method of Laser Induced Breakdown Spectroscopy*, MPhil Thesis, University of Wales Swansea

Levesque, S., Babin, F., and Gagne, J., M., (April 1993) *Calibration of Pulsed Laser Wavelength by Optogalvanic Spectroscopy in Hollow Cathode Discharges*, IEEE Transactions on Instrumentation and Measurement, Vol. 42, No. 2, 251-254

Muraoka, K. and Maeda, M., (1993) *Application of Laser-induced Fluorescence to High-temperature Plasmas*, Plasma Physics and Controlled Fusion, Vol. 35, 633-656

Rohwetter, Ph., Yu, J., Mejean, G., Stelmaszczyk, K., Salmon, E., and Kasparian, J., (2004) *Remote LIBS with Ultrashort Pulses: Characteristics in Picosecond and Femtosecond Regimes*, Journal Analytical Atomic Spectrometry, Vol. 19, 437-444

Rosen, A., and Zutavern, F., (1993) *High-Power Optically Activated Solid State Switches*, Artech House Inc.

Senturk, S., (1996) *Universal Detection System for Opt-galvanic Signals Generated by CW and Pulsed Laser*, MPhil Thesis, University of Wales Swansea

Silfvast, W. T., (2003) *Laser Fundamentals*, 2nd ed. Cambridge University Press

Telle, H. H., Beddows, D. C. S., Morris, G. W., and Samek, O., (2001) *Sensitive and Selective Spectrochemical Analysis of Metallic Samples: The Combination of Laser-induced Breakdown Spectroscopy and Laser-induced Fluorescence Spectroscopy*, Spectrochimica Acta Part B: Atomic Spectroscopy, Vol. 56, 947-960

Thorlabs Catalogue, (2006) *Tools of the Trade*, Volume 18

Utomo, A. (1994) "High resolution spectroscopy using tuneable diode lasers", PhD Thesis, University of Wales Swansea

Verdeyen, J. T., (1989) *Laser Electronics*, 2nd Ed., Prentice-Hall

Whitehouse, A. I., (2006) *Laser-induced Breakdown Spectroscopy and its Application to the Remote Characterization of Hazardous Materials*, Applied Photonics, Vol. 18, No. 2

Wilson, J. and Hawkes, J. F. B., (1987) *Lasers Principles and Applications*, Prentice-Hall International (UK) Ltd.

Yueh, Y. F., Jagdish, P. S., and Hansheng, Z., (2000) *Laser-induced Breakdown Spectroscopy, Elemental Analysis*: in Encyclopaedia of Analytical Chemistry: R. A. Meyers (Ed.), 2066-2087

Web pages

www.cvilaser.com/Common/PDFs/Harmonic_Separators_Discussion.pdf

www.en.wikipedia.org/wiki/Pellin-Broca_prism

www.its.blrdoc.gov/projects/devglossary/_pulse_duration

www.lasalle.edu/academ/chem/laser_web/ndyag_laser.html

www.ledmuseum.candlepower.us/yelldpss.htm

www.redoptronics.com/fused-silica-optical-material.html

www.repairfaq.ece.drexel.edu/sam/CORD/leot/course03_mod03/mod03-03.html

www.sp3plus.co.uk/optics/right-angle-prisms.htm